The University of Birmingham

Microstructural Analysis of Aluminium Alloy 2096 as a Function of Heat Treatment

By

Andrew Williams

A thesis submitted to
The University of Birmingham
for the degree of

Master of Research

School of Metallurgy and Materials
The University of Birmingham
August 2010

Preface

This thesis describes project work carried out within the School of Metallurgy and Materials Engineering at the University of Birmingham from May 2007 to November 2008.

The submission of this thesis is in accordance with the requirements of the award of 'Master of Research in the Science and Engineering of Materials' under the auspices of the University.

Acknowledgements

Firstly, it is only right that I acknowledge the support of my two supervisors, Prof. I.P. Jones and Dr. B.J. Connolly from the School of Metallurgy and Materials at the University of Birmingham. Quite simply this work would not have been completed without their constant advice, direction, and most importantly, patience. They have guided me throughout this project and given me a kick when motivation was required. For what they have done for me, I will always be grateful.

I have received invaluable support from a number of academic and technical staff at the University. For this, I would like to show my gratitude to the following people for providing me with the theoretical and practical knowledge required to carry out my work: Dr. R. Ding, Dr, Y. Tse, Mr. P. Stanley, and Ms. M.Q. Chu.

Finally, I will never be able to convey, in words, the gratitude that I have for my family. Their patience and understanding is endless. I hope that my achievements go some way to thank them for a lifetime of support.

Abstract

A detailed microstructural investigation into possible metallurgical culprits of stress corrosion cracking (SCC) of Al-Li-Cu alloy AA2096 was carried out as a function of isothermal aging time at 160°C. Two tempers were analysed for this study: under-aged at 4 hours (UA4) and under-aged at 12 hours (UA12).

Transmission electron microscopy (TEM) was used to document T_1 (Al_2CuLi) precipitation near to and on low and high angle misorientation grain boundaries. The low-angle grain boundaries of the UA4 temper exhibited a fine, near continuous decoration of T_1 precipitates and a narrow, but distinct T_1 precipitate free zone (PFZ) adjacent to the boundary. The high angle boundaries of the UA4 temper either showed no grain boundary T_1 precipitation, or contained a single, large T_1 precipitate that grew along the boundary causing it to pucker. The low-angle boundaries of the UA12 temper exhibited no such PFZ, with no greater T_1 precipitation than observed in the grain matrix.

An energy dispersive X-ray (EDX) study was conducted to investigate the possible occurrence of copper solute depletion across grain boundaries. In the UA4 temper, the low-angle grain boundaries exhibited a distinct copped depleted zone that corresponded with the PFZ observed.

Contents **Page**

List of Figures

Section 1.

Section 2.

Section 4.

List of Tables

Section 1.

Section 2.

List of Definitions

BCC	Body Centre Cubic
CBED	Convergent Beam Electron Diffraction
CPH	Close Packed Hexagonal
EDX	Energy Dispersive X-ray Spectroscopy
FCC	Face Centre Cubic
FWTM	Full Width Ten Percent Maximun
GP Zone	Guinier-Preston Zone
ICG	Intergranular Corrosion
PFZ	Precipitate Free Zone
SAD	Selected Area Diffraction
SCC	Stress Corrosion Cracking
STEM	Scanning Transmission Electron Microscope/Microscopy
TEM	Transmission Electron Microscope/Microscopy
UA4	Under-aged (Four Hours)
UA12	Under-aged (Twelve Hours)

1. INTRODUCTION

1.1. Background

Over several decades rising fuels costs have driven the aerospace industry to constantly re-evaluate the materials used in modern air frames. In light of recent environmental concerns with CO_2 emissions, reducing the weight of air frames in the interest of fuel efficiency is of primary concern. While some manufacturers have increased interest in carbon fibre composite designs, there is still a great deal of work being carried out to improve current super-alloys by increasing strength and toughness while reducing overall density/weight.

It is widely accepted that the addition of lithium to modern Al-Cu alloys gives rise to a 3% decrease in density, while increasing the Young's modulus by up to 6% (for lithium additions up to 4%) [2, 3]. This factor, coupled with the high strength and toughness of Al-Cu alloys, makes the system commercially attractive. However, a significant concern has been raised in the form of intergranular stress corrosion cracking (IGSCC). SCC can lead to catastrophic and sudden failure of engineering components. Microscopic cracks develop under certain conditions, leaving otherwise ductile metals very brittle. Cracks initiate and propagate at very slow rates, typically of the order of 10^{-9} to 10^{-6} $m.s^{-1}$. These cracks continue to grow until the fracture strength of the metal is exceeded. For SCC to occur three criteria must be met: a susceptible microstructure, a tensile stress, applied or residual and a corrosive environment.

1.2. Literature Review

1.2.1. History

Aluminium alloys with additions of lithium have been in development since the early 1920's. Scleron, a Al-Zn-Cu-Li alloy, was developed in Germany in 1924 [6] and more notably, Alloy 2020, an Al-Cu-Li alloy that was first developed in the United States in the 1950's by Alcoa [6, 7]. For both alloys the considerable reduction in density achieved with additions of lithium was the primary driving force for development. It was later realised that lithium also offered a significant increase in the Young's modulus of the alloy system. Sankaran and Grant [8] went on to conclude that with each weight percent addition of lithium to the Al-Cu alloys (2XXX series) a corresponding decrease in density of 3% and an increase in modulus of 6% were observed for lithium additions of up to 4%.

Although the potential of the Al-Cu-Li-X system was recognised in the early 1940's by LeBaron [9], working for Alcoa, it was quickly overshadowed by the introduction of an Al-Zn-Mg-Cu alloy system (7075). It wasn't until the mid 1950's that Hardy and Silcock [10, 11] picked up interest in the Al-Cu-Li system with their investigations into phase equilibria and tensile properties. By 1957 Alcoa had released their Al-Cu-Li-Mn-Cd alloy, X-2020 [7]. Not only did the high tensile properties of X-2020 stand out, but it also offered good resistance to stress corrosion cracking. The alloy was used for the wing skins of the US Navy's supersonic 'Vigilante' fighter – bomber (RA-5C) and marked the first commercial application of an Al-Cu-Li-X alloy. However, alloy X-2020 was plagued with poor fracture behaviour issues and occurrences of stress corrosion cracking which sparked further

research to understand the microstructure and precipitation reactions within Al-Cu-Li-X systems as well as their response to cold work and aging treatments [12].

1.2.2. Microstructure

The physical metallurgy of Al-Li-Cu alloys is very complex with many forms and chemistries of precipitating particles. Figure 1.1. shows the phase diagrams for the binary Al-Cu and the ternary Al-Cu-Li alloys [1]. Figure 1.2. shows the possible composition relationships for Al-Li-X alloys[4]. Huang and Ardell [13] showed that Al-Li-Cu-X alloys were strengthened primarily by incoherent T_1 (Al_2CuLi) precipitation. T_1 is known to precipitate heterogeneously at dislocations and grain boundaries in 2090 type alloys and to lie on a {111}a habit plane [14]. Lithium provides precipitation strengthening to aluminium alloys by a homogenous distribution of coherent, spherical δ' (Al_3Li). Equilibrium phase δ (AlLi) forms mainly at grain boundaries [7] and can lead to void nucleation and intergranular fracture [15]. With small additions of zirconium, precipitation of β' is possible. β' is a spherical, coherent $L1_2$ structure like δ'. The fine β' particles act to pin grain boundary movement, thereby resisting grain growth [16]. β' particles also act as preferential nucleation sites for δ'. The S phase, lying on a {210} habit plane, is considered to be semi-coherent and lath-shaped. The S' phase is nearly identical in structure, but with marginally different lattice parameters *(14)*. This has led many authors to make no distinction between the two phases. S'(S) phases can form by heterogeneous nucleation from vacancy loops, by heterogeneous nucleation on dislocations, and by transformation of, or nucleation on, the intermediate precipitate S" [17]. The binary θ' (Al_2Cu) phase has a {100} habit plane and can also form preferentially on β' dispersoids throughout the matrix. θ'

formation is affected by the Li:Cu ratio. Preferential formation of T_1, T_2 (Al_6CuLi_3) and T_B ($Al_{7.5}Cu_4Li$) is at the expense of θ' [18]. Silcock suggested that Li could be incorporated into θ' at longer aging times, leading to T_B precipitates forming along grain boundaries [5]. With over-aging, the T_2 phase starts to nucleate at grain boundaries.

In terms of localised corrosion the primary precipitates of interest are the T family and S phase. These precipitates have been shown to be electrochemically active compared to an Al-Cu matrix. The extent of activity and the extent and form of precipitation (e.g., continuous decoration along a grain boundary) may dictate the susceptibility of the alloy to preferential grain boundary dissolution. It should be noted that there may be differences in electrochemical activity within the T family. Due to the increased lithium content, the T_2 particle has a high electrochemical activity, leading to a higher dissolution rate than T_1 and T_B [19, 20]. The various possible phases are discussed in further detail in the following sections.

Precipitate	Structure	Form	Habit Plane	References
δ' (Al_3Li)	FCC	Sphere	N/A	[2, 21]
θ' (Al_2Cu)	Tetragonal	Disc	{100}	[22]
T_1 (Al_2CuLi)	Hexagonal	Plate	{111}	[10]
S' (Al_2CuMg)	Orthorhombic	Lath	{210}	[23]
Ω (Al_2Cu)	Orthorhombic	Plate	{111}	[22]
β' (Al_3Zr)	FCC	Sphere	N/A	[14]

Table 1.1. Description of major precipitate phases in Al-Li-Cu-X alloys

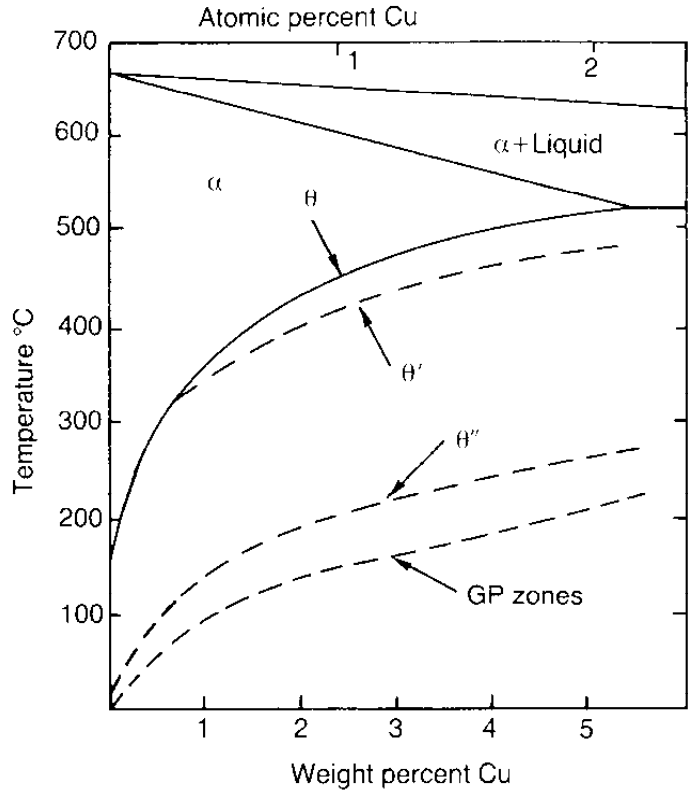

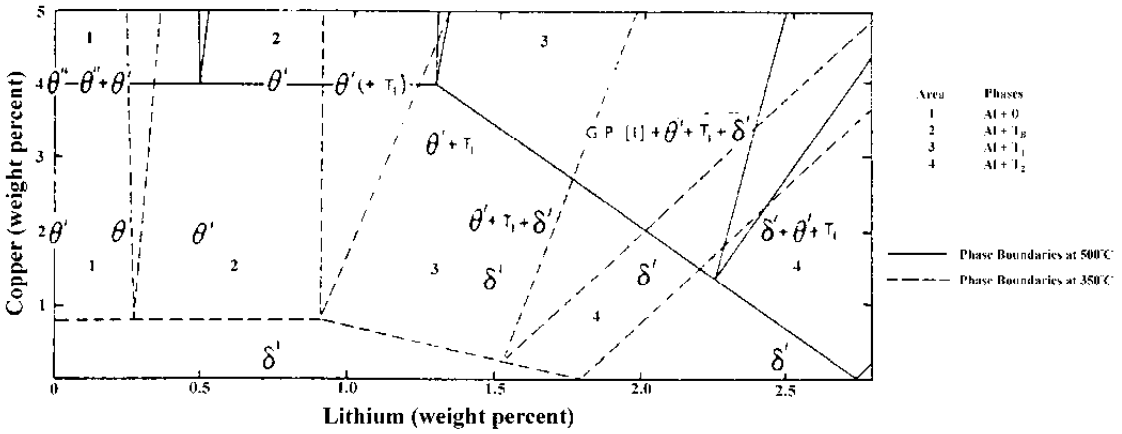

Figure 1.1. a) Aluminium corner of the Al-Cu binary phase diagram [1]. b) Aluminium corner of the Al-Cu-Li phase diagram [5]

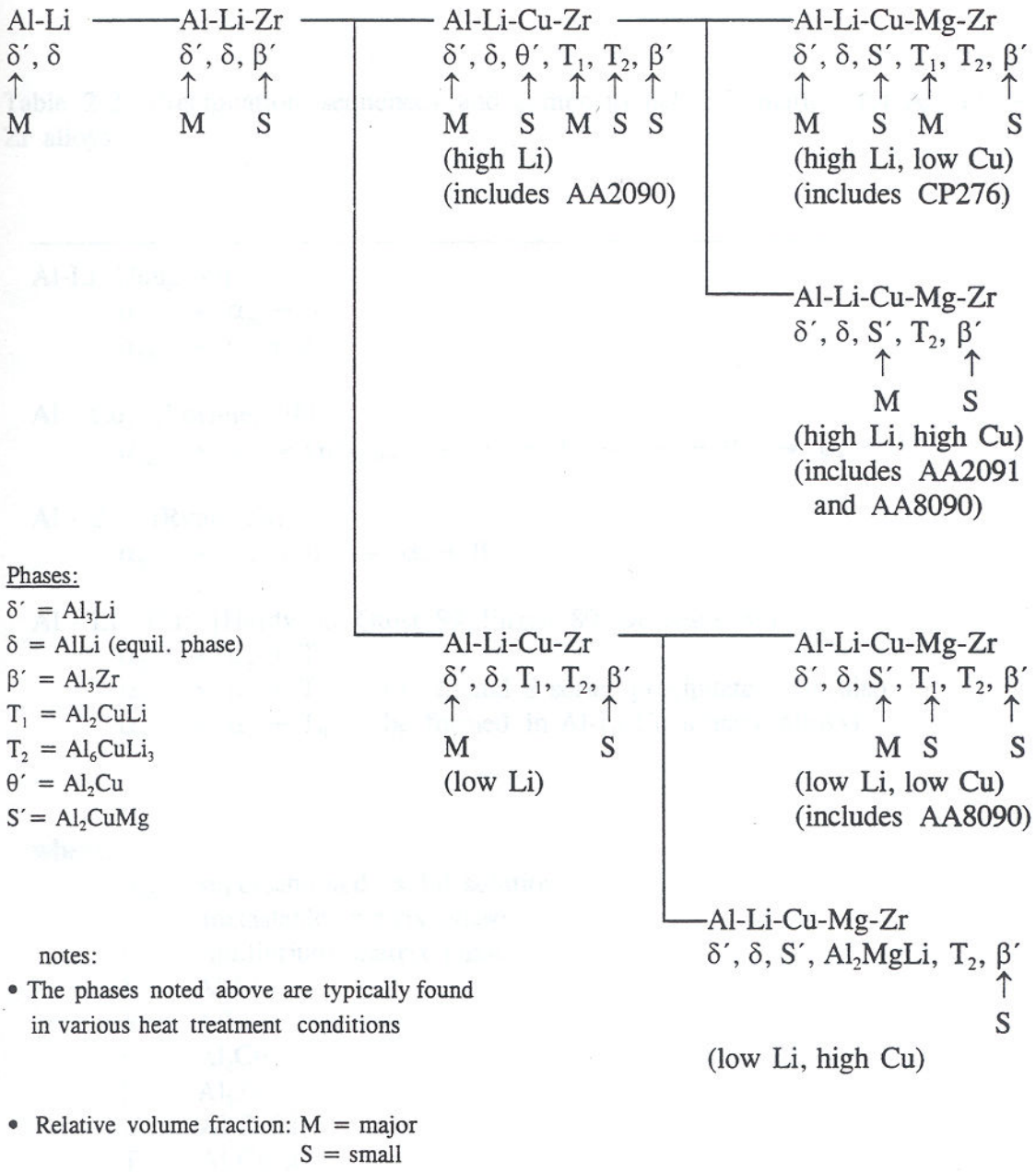

Figure 1.2. A compilation of possible composition/phase relationships in Al-Li based alloys [4].

1.2.2.1. δ/δ’

The pioneering X-ray studies of Silcock [5] showed the precipitation sequence of the binary Al-Li system to be:

α (supersaturated) → δ’ (Al_3Li) → δ (AlLi)

The metastable δ’ phase has a $L1_2$ structure and forms homogenously throughout the matrix as spheres, possessing a cube-cube orientation with the matrix and a small misfit strain [5, 24, 25]. δ’ occurs when Al-Li alloys containing more than 1% lithium are quenched from solution heat treatment at a temperature above the δ solvus and artificially aged at a temperature below the δ’ solvus [26]. It is generally accepted that the mechanism of formation is by spinodal composition [27, 28], although Williams et al. disagree, speculating the mechanism to be homogenous nucleation [25]. The δ’ precipitate has been shown to coarsen in line with Lifshitz-Wagner kinetics with the average radius increasing approximately $t^{1/3}$ [25, 29-32]. As well as this coarsening, δ’ has also been observed to coarsen at defects such as dislocations (9) and grain boundaries [21].

δ’ plays a role in the strengthening of Al-Li-X alloy systems. A study by Noble et al. [33] summarised the four possible models for the strengthening of Al-Li alloy systems by δ’:

- Strengthening by dislocation pairs forming an anti-phase boundary.
- Strengthening due to the difference in shear modulus between the matrix and precipitate.
- Strengthening due to the misfit strain between precipitate and matrix
- Strengthening due to shearing of the precipitate by moving dislocations.

The study calculated that strengthening due to the formation of an anti-phase boundary by dislocation pairs, was the dominant mechanism. However, in systems with lower lithium content, such as 2xxx type alloys, the volume fraction of δ' will be much lower than in higher lithium content alloys. The strengthening contribution from δ' in that case will be much less than other precipitates [16]. Although δ' formation plays a role in strengthening of Al-Li-X alloys, precipitation close to grain boundaries can have a negative effect on the ductility and toughness of the material. Due to the highly shearable nature of δ' particles leading to increased planar slip, their formation can cause high stresses at grain boundaries through dislocation pile up reducing the overall fracture resistance [33, 34].

Generally, at longer aging times, formation of the stable, equilibrium δ precipitate is possible. The δ precipitate has a BCC structure and is semi-coherent with the matrix. The δ phase has been observed to predominately precipitate heterogeneously at high-angle grain boundaries (>9º) [34, 35]. However, Tosten et al. [36] also observed some δ precipitation at high angle boundaries in an Al-Li-Cu alloy in the underage condition as well as at low angle boundaries and within the matrix in the overage condition. The formation of the δ phase can lead to δ' precipitate free zones (PFZs) [37], having a deleterious effect of on the fracture resistance of Al-Li and Al-Li-X alloys [38]. δ' PFZs have been shown to be areas of increased plasticity compared to the matrix, leading to void nucleation and intergranular fracture [15].

1.2.2.2. θ’

The Al-Li system becomes more complex with the addition of copper. The precipitation sequence has been summarised below [4, 5, 10]:

$$
\begin{array}{lll}
 & \rightarrow & T_1\ (Al_2CuLi) \\
 & \rightarrow & T_2\ (Al_6CuLi_3) \\
\alpha\ (\text{supersaturated}) & \rightarrow & T_B\ (Al_{7.5}Cu_4Li) \\
 & \rightarrow & \delta'\ (Al_3Li) \rightarrow \delta\ (AlLi) \\
 & \rightarrow & \text{GP zones} \rightarrow \theta'' \rightarrow \theta' \rightarrow \theta\ (Al_2Cu)
\end{array}
$$

The tetragonal θ’ has a disc morphology, with a {100} habit plane and nucleates heterogeneously at dislocations [39, 40]. Silcock showed that cold work and small additions of cadmium (0.1%) produce a finer dispersion of small θ’ platelets in an Al-Li-Cu alloy [5, 41]. However, Starke and Lin warned that cadmium could segregate to grain boundaries, enhancing crack propagation by lowering the surface energy [42]. Studies have found that θ’ aids in the strengthening of aluminium alloy 2020 (Al-Cu-Li-Cd) [41, 43].

1.2.2.3. T_1

The ternary T_1 phase (Al_2CuLi) posses a hexagonal structure and forms as thin plates with a {111} habit plane [10]. The precipitate primarily nucleates heterogeneously at G.P. zones, dislocations by a stacking fault mechanism and at sub-grain boundaries [44]. With higher densities of T_1, the formation of θ’ is inhibited by competition for available copper [45]. With over-aging, T_1 becomes the dominant precipitate in Al-Li-Cu-X alloys at the expense of θ’ and to some extent δ’ [18, 36].

There is some disagreement as to the strengthening contribution of the T_1 precipitate. Gregson and Flower believed that T_1 was ineffective at breaking up strain localisation in Al-Li-Cu-X systems, therefore having little effect on strength [46]. However, other authors [47, 48] state that the unshearable nature of T_1 governs the yield strength in these alloys. To further complicate matters, Howe et al. observed T_1 plates being sheared by moving dislocations using high resolution transmission electron microscopy (HRTEM) [49]. In this case, the strengthening mechanisms involved are believed to be chemical strengthening and Orowan strengthening [50].

In Al-Li-Cu alloys, T_1 is the dominant precipitate at low-angle boundaries in the underage tempers [35]. In aluminium alloy 2096, Connolly observed heavy, nearly continuous T_1 precipitation in the under-aged temper at low angle grain boundaries (5 – 13º) [20]. A corresponding δ' PFZ of approximately 25nm was observed at such boundaries. Higher angle boundaries (≥13º) were found to contain one or two very large T_1 precipitates that puckered the grain boundary. No associated grain δ' PFZs were observed in the vicinity of this type of grain boundary. With very low angle grain boundaries (≤3º) no greater precipitate density than the matrix and no associated δ' PFZ was observed. These observations are in line with previous studies into the role of grain boundary precipitation of T_1 [35].

1.2.2.4. T_2/T_B

The icosahedral T_2 phase (Al_6CuLi_3) forms as long rods of lengths in the region of 0.2 – 1μm [51, 52]. The precipitate forms throughout the matrix , but more notably at grain boundaries [51], following a {100} habit plane [53]. The formation of

T_2 is the subject of some disagreement. White et al. found T_2 to form during quenching from solution heat treatment [54], while Cassada et al. found the phase to precipitate during isothermal aging above 150ºC.

In terms of localised corrosion the T_2 is of particular interest. The extent and form of precipitation (e.g. continuous decoration along a grain boundary) may dictate the susceptibility of the alloy to preferential grain boundary dissolution. Due to the high lithium content, the T_2 particle has a higher electrochemical activity, leading to a higher dissolution rate than either T_1 or T_B [19, 55]. Rioja et al. [53] found that an applied deformation, prior to aging, refined the microstructure of Al-Li-Cu alloys. The study demonstrated that as the amount of deformation increased the volume fraction of T_2 within the matrix also increased reducing the amount of T_2 at the grain boundary. With the reduction of the highly reactive T_2 precipitate in the vicinity of grain boundarie, overall fracture toughness is improved. Crooks and Starke [56] suggested that a reduction in the aging time of Al-Li-Cu alloys would reduce the T_2 precipitate size thereby increasing the overall strength.

The cubic (FCC) T_B phase (Al_7Cu_4Li) forms in rod-like shapes lying on a {311} habit plane [57]. Silcock suggested longer aging times in Al-Li-Cu alloys promoted the formation of T_B precipitates along grain boundaries [5]. The formation of T_B is at the expense of θ' due to competition for available lithium. A study of aluminium alloy X2020 by Kang and Grant [43] found agreement with the observation that the formation of T_B is due to the transformation of θ' in the presence of lithium.

The study also concluded that the presence of T_B aids in the strengthening of Al-Li-Cu alloys.

1.2.2.5. β'

The coherent β' dispersoid (Al_3Zr) forms as small additions of zirconium are introduced to the system. The particle has a spherical morphology, a L12 structure and forms throughout the matrix [16]. Several studies have shown that β' acts as a preferential nucleation site for δ' [35, 58-60]. With the β' particle acting as a central core, the δ' completely 'wets' the β' dispersoid. A study by Galbraith et al. [60] showed that the β' particle can also act as a nucleation site for the θ' and, to a lesser extent, the T_1 precipitates.

As the degree of recrystallisation and grain morphology can have a detrimental effect on the corrosion behaviour of Al-Li alloys [61], it is desirable to keep such recrystallisation under control. Several authors have reported that β' acts to pin grain boundaries thereby retarding recrystallisation [2, 16, 45]. In particular the study conducted by Starke and Sanders [2] showed that the microstructure of an Al-Li-Cu-Zr alloy, containing β' particles, was completely un-recrystallised after processing. Rystad and Ryum [62] speculated that as the recrystallisation front passes the β' particle the matrix-precipitate interface changes to a semi-coherent form, imparting a high drag force and inhibiting the movement. Alternatively, Sanders and Starke have suggested that for the subgrain boundary to move, the β' particle must completely dissolve and re-precipitate after the advancement of the front. The

suggestion is in agreement with experimental observations that require a very high recrystallisation temperature for zirconium-containing aluminium alloys [30].

1.2.2.6. S/S'/S''

As magnesium is added to Al-Li-Cu-X alloys precipitation of the S/S'/S'' phase occurs. The lath-shaped, semi-coherent S phase (Al_2CuMg) lies on a {210} habit plane with a face centred orthorhombic structure [63]. The S' phase is nearly identical in structure but with marginally different lattice parameters. This has led many authors to make no distinction between the two phases. Indeed Reich et al. [64] ruled out S' as a distinct phase concluding that it was a continuous precursor to S phase formation. Additionally, Wang and Starink [65] proposed an additional FCC, coherent, aluminium-rich structure that forms early in the aging process known as S'' ($Al_{10}Cu_3Mg_3$). With this considered the proposed precipitation process for Al-Cu-Mg alloys is as follows:

$$\alpha \text{ (supersaturated)} \rightarrow GPB_{zone} \rightarrow S'' \rightarrow S' \rightarrow S\ (Al_2CuMg)$$

The S phase has been observed to nucleate heterogeneously at vacancy loops, dislocations and low angle grain boundaries or by transformation of the intermediate S'' precipitate [17, 23, 66, 67]. A slight stretch, prior to solution heat treatment, will introduce further dislocations aiding with the nucleation of heterogeneous S precipitates [23, 68]. S'/S plays an important role in the strengthening of Al-Li-Cu-X alloys. Gregson et al. [67] found that the presence of S precipitates in an Al-Li-Cu-Zn-Mg alloy promoted cross slip within the system which helped in the homogenising of

deformation behaviour and improved overall ductility. In a study by Starink et al. [68] two types of S phase strengthening were discussed. In the earlier stages of aging, dispersion strengthening is provided by heterogeneously nucleated, non-shearable S phase precipitates. Upon further aging this process is impeded due to competition for the available copper and magnesium by homogeneously nucleated S phase precipitates. These shearable, homogeneously nucleated precipitates provide order strengthening and will become the dominant factor in the later stages of aging.

1.2.2.7. Ω

The Ω phase precipitate forms in thin plates on a {111} habit plane [22, 69, 70]. Some controversy exists regarding the structure of the Ω precipitate. Proposed structures have included monoclinic [71], hexagonal [69], tetragonal [72, 73] and orthorhombic [22, 70]. Later review work carried out by Wang and Starink [74] concluded that the precipitate was probably orthorhombic. It is widely reported that small additions of silver to the Al-Li-Cu-X system promote nucleation of the Ω precipitate [69, 74, 75]. It is believed that a change in the vacancy-solute interactions as well as a change in the stacking fault energy is responsible.

1.2.3. Intergranular Stress Corrosion Cracking of Al-Li-Cu-X Alloys

Despite the seemingly attractive properties of the Al-Li-Cu-X system, these alloys have historically been plagued with issues of intergranular corrosion (IGC) and stress corrosion cracking (SCC). Although much previous work has been carried out to investigate the susceptibility of these alloys to SCC [3, 76-78] overall agreement on the mechanism of SCC is yet to be reached.

Four possible mechanisms for SCC failure of Al-Li and Al-Li-Cu alloys have been proposed: 1) Anodic dissolution at copper-depleted zones along high-angle and low-angle grain boundaries [79, 80]. 2) Dissolution of anodic precipitates such as T_1, T_2, T_B and δ at high-angle and low-angle grain boundaries [10, 41]. 3) Dissolution or hydriding promoted by lithium or trace impurity segregation at grain boundaries [81, 82]. 4) Hydrogen embrittlement by decohesion of weakened interfaces or by hydrogen precipitate phases such as δ [83, 84]. There is general agreement that localised corrosion sites serve as initiation points for SCC [85, 86].

Galvele and DeMicheli's work [87] concluded that intergranular corrosion of Al-Cu alloys would only occur if the following conditions were satisfied: The alloy must have a solute depleted zone along the grain boundaries; the corrosive environment must contain anions that are capable of breaking down the passivity of the alloy; the breakdown potential of the solute depleted zone must be a more negative electrochemical potential that that of the grain matrix and the corrosion potential of the alloy must be a less negative electrochemical potential to the breakdown potential of the metallurgical feature at the grain boundary and must have a more negative electrochemical potential to the breakdown potential of the grain matrix. With these conditions satisfied, it was believed that an overlapping string of micro-pits could form along the copper-depleted zone adjacent to the grain boundary.

Sugimoto et al [88] investigated the role of aging time of the SCC susceptibility and pitting potential in a NaCl environment. Their work showed that the difference in the pitting potential of the grain boundary feature and the grain matrix was most

significant in the under-aged tempers whereas little difference was found between the pitting potential of the grain boundary feature and grain matrix in the over-aged tempers. Therefore SCC susceptibility is not observed of the over-aged alloy. Much agreement was found in further studies of various Al-Cu alloys [89-91], corroborating the findings of Sugimoto et al.

There has been much disagreement over the controlling grain boundary feature for intergranular corrosion and SCC in Al-Li-Cu alloys with three possible mechanisms for the preferential anodic dissolution of grain boundary features proposed. Copper depletion adjacent to the grain boundary is accepted by several authors as the controlling feature of the electrochemical framework required for intergranular corrosion and SCC to occur in Al-Li-Cu alloys [79, 80].

Although the mechanisms of intergranular corrosion and SCC of Al-Li-Cu alloys has been investigated in great detail reconciliation of SCC as a function of isothermal aging time is yet to be achieved. Much disagreement exists as to the most susceptible temper (i.e. under-aged, peak-aged or over-aged) to SCC. Several studies have concluded that the under-aged tempers are more susceptible [41, 92, 93] while others have reported the peak-aged tempers to be more susceptible [37, 93-95] others report that the over-aged tempers to be more susceptible [96] and yet other investigations suggest that all tempers are equally susceptible [3, 97]. It must be considered that the variation in the alloy composition, dislocation density, re-crystallised grain structure and processing techniques of these different studies will have affected the overall outcome, thereby confounding the use of aging treatment as

an indicator of SCC susceptibility. Conventional metallurgical thinking alone would suggest that more than one factor must be responsible for the different windows of SCC susceptibility observed in Al-Li-Cu alloys.

Connolly and Scully [19, 20, 55] investigated the SCC susceptibility of AA2096 as a function of isothermal aging time. The work concluded that two distinct windows existed for SCC susceptibility: the severely under-aged (4-8 hours) and the over-aged (70-120 hours) tempers (see Figure 1.3).

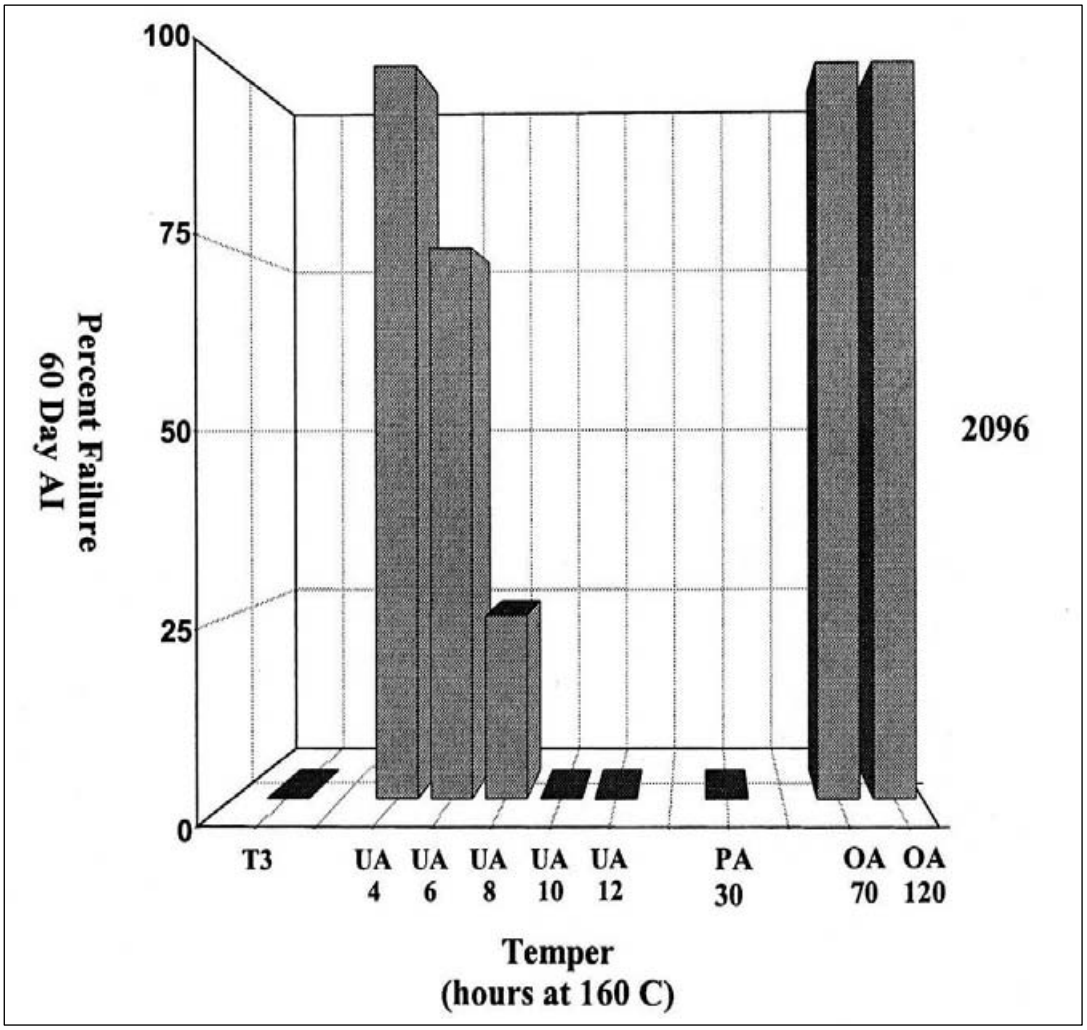

Figure 1.3. SCC susceptibility for AA2096 as a function of isothermal aging time at 160ºC [19, 20, 55].

1.3. Project Aims and Objectives

Two possible metallurgical mechanisms that are viable to explain the SCC susceptibility of AA2096 will be investigated in this study. Firstly, a preferential path for grain boundary dissolution can be caused by the precipitation of actively corroding particles at grain boundaries. Secondly, the formation of copper-rich precipitates close to a grain boundary can lead to copper depletion from the solid solution neighbouring the boundary, leaving the depleted zone that has a higher electrochemical activity than the matrix. Due to the difference in electrochemical potential between the matrix and grain boundary the depleted zone is highly susceptible to preferential dissolution or pitting. Connolly's work [19, 20, 55] indicated that grain misorientation plays a major role in the precipitation of T_1 (Al_2CuLi) particles at grain boundaries. Specifically, at low angle boundaries (5-13°) a greater density of T_1 precipitates were observed along the boundary forming a near continuous coverage.

The primary aim of this project is to carry out a detailed transmission electron microscope (TEM) investigation into the microstructural evolution of AA2096 as a function of isothermal aging time. Electron diffraction is to be used to identify different precipitates, particularly near to and on grain boundaries, as a function of aging time and grain misorientation. The development of active precipitates (i.e., T_1) as a function of aging time and grain misorientation will be documented. In addition, EDX line scans will be performed to measure Cu depletion as a function of aging time and grain misorientation.

2. RELEVANT ELECTRON MICROSCOPY THEORY AND ANALYSIS TECHNIQUES [98-100]

2.1 Transmission Electron Microscopy

A Philips Tecnai F20 field emission gun transmission electron microscope (TEM) incorporating an Oxford Instruments Isis 300 energy dispersive X-ray (EDX) analysis system was used for imaging, microstructural characterisation, phase identification, precipitate density analysis, and X-ray line scans across grain boundaries.

2.1.1. Electron Diffraction

Electron diffraction is a collective scattering phenomenon occurring as the incoming electrons within the electron beam are scattered by the atoms of the crystal lattice within the specimen being examined. The incoming plane electron wave interacts with the atoms and secondary waves occur which interfere with each other. The interference occurs either constructively, reinforcing the electron wave at certain scattered angles generating diffracted beams, or destructively by cancelling out the wave. The process is analogous to the diffraction of light through a diffraction grating with the atomic planes acting as the grating slits.

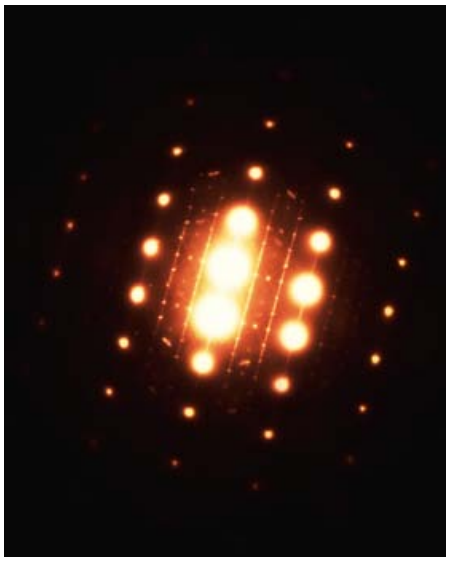

Figure2.1. Electron diffraction pattern illustrating various spots and streaks associated with different precipitate phases being present.

As with X-ray diffraction (XRD) the scattering can be described as a reflection of the beams at planes of atoms (lattice planes). As the wavelength of the electrons, λ, and the diffraction angle, θ, are known, Bragg's Law can be used to calculate the interplanar distances, d, of the lattice. Furthermore the technique can be used to identify different phases within a bulk sample. With knowledge of the crystal structure of possible precipitates, the diffraction pattern can be used to confirm the presence of such precipitates within the sample area being examined (see Figure 2.1).

To analyse a small area of the diffraction pattern the selected area aperture can be used. By introducing the aperture to the beam at the back focal plane only electrons scattered from a particular area of the sample will pass through to the display screen. This technique is known as selected area diffraction (SAD). The technique can be particularly useful when qualitatively assessing distribution of precipitates within the area being examined.

2.1.2.1. Kikuchi Diffraction

In addition to diffraction spots thicker areas of the specimen also contain complex patterns of pairs of dark and bright lines which contrast against the diffuse background scattering. These lines are known as Kikuchi lines. Kikuchi lines occur due to the Bragg diffraction of electrons that were initially inelastically scattered on entering the top surface of the specimen. In addition to electrons that pass straight through the specimen, and those that are elastically diffracted (without loss of energy) a proportion of the electrons are inelastically scattered through a wide range of angles, losing energy in the process. Some of these electrons will be scattered at such

an angle that they are subsequently elastically scattered by lattice planes lying at a Bragg angle, θ_B. In three dimensions the electrons re-diffracted in this manner form two cones, known as Kossel cones (see Figure 2.2). After the Bragg diffraction there is a net loss of electrons in the lines closest to the incident beam direction and a net

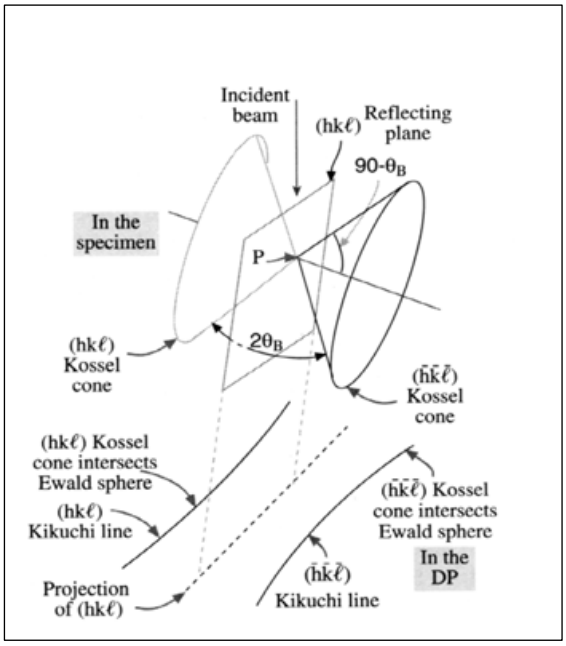

Figure 2.2. Diagram illustrating Kossel cones originating at P on the diffracting plane. As the cones intercept the Ewald sphere, parabolas are formed, approximating to straight Kikuchi lines in the diffraction pattern.

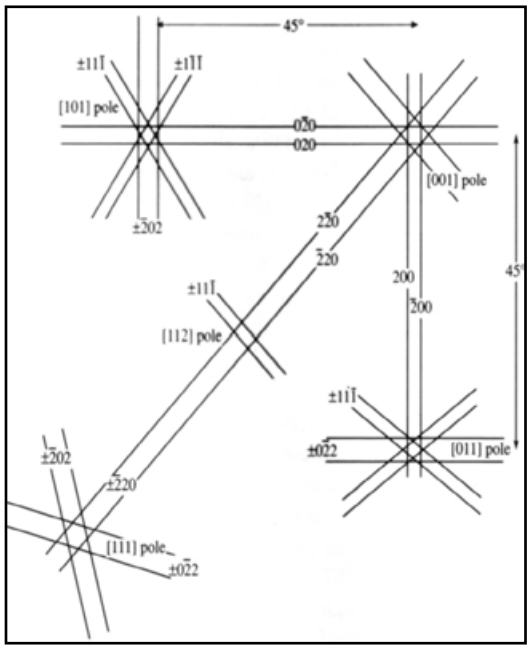

Figure 2.3. Example of a Kikuchi Map

gain in electrons in the line furthest from the incident beam direction. The result being that the lines of net loss appear dark in the image and the lines of net gain appear bright. Thus, Kikuchi lines always appear as a pair of bright and dark lines. Further lines will appear in the diffraction pattern for all other possible reflecting planes in the crystal resulting in a complex array of Kikuchi line pairs. This array of lines forms the basis of the 'Kikuchi Map' (see Figure 2.3). As the Kikuchi lines are fixed to the crystal structure, they will move as the specimen is tilted. To this effect

the lines can be used as a 'roadmap' assisting the operator in tilting between zone axes.

2.1.2. Measurement of Grain Misorientation

Several metallurgical factors control the chemistry in the vicinity of grain boundaries. The misorientation of one grain relative to an adjacent grain is one such factor having a distinct effect on the precipitation around the grain boundary area. Several techniques exist to reliably measure the misorientation between grains. For this project Kikuchi lines were used to measure misorientation, with an acceptable margin for error. Initially the primary grain is centred about a zone axis. The sample is then shifted, without tilting, to an adjacent grain. The Kikuchi map around the next grain is then imaged. By measuring the shift of the pole from the zone axis it is possible to calculate the angle of misorientation from the primary grain, to within ~1º of accuracy; regarded as a reasonable degree of error. For further information regarding the calculation of grain misorientation refer to section 3.2.1.

2.1.3. Bright Field and Dark Field Imaging

To reduce the scattering of electrons that would otherwise reduce the contrast of an image the objective aperture is introduced to the back focal plane. The aperture is then adjusted to allow only electrons from the direct beam through. The resultant image occurs due to a weakening of the direct beam by the sample. In this case mass-thickness and diffraction contrast only contribute to the image formation. With this image formation thick areas and areas of increased crystalline density will scatter

more electrons than lower-mass areas and will therefore appear with darker contrast at the image plane.

Dark field images are formed by adjusting the objective aperture to block the direct beam. The aperture can be shifted to only allow electrons from a specific area within the diffraction pattern to pass. As the diffracted beam has interacted strongly with the specimen the dark field image contains useful information about planar defects, stacking faults and particle size. It is also possible to use dark field imaging to qualitatively assess the distribution of precipitates within a sample area. Precipitate phases will cause reflections of the diffracted beam that appear as spots or streaks within the diffraction pattern. The objective aperture is shifted to only allow electrons from such a feature through. The contrast of the selected precipitate phase will be largely increased within the resultant dark field image assisting in the identification and assessment of the desired phase.

3. EXPERIMENTAL PROCEDURE

3.1 Material

The aluminium alloy 2096 used in this study was fabricated by Reynolds Metals. After casting the alloy was homogenised and extruded into 5mm thick panels. The panels were solution heat treated at 530ºC for 1.5 hours, stretched by 3% and isothermally aged by a single step method at 160ºC for various times covering the range from severely under-aged (2 hours) to over-aged (70 hours). The composition of AA2096 was analysed for a previous study [20] (see Table 4.1).

3.2 Microstructural Characterisation

For microstructural evaluation via TEM the specimen pieces were sectioned from the rolling direction/normal direction (RD/ND) plane of untested (i.e., not exposed to corrosive environments) extrusions using a Si-C wafering blade into slices approximately 0.5 – 1 mm thick. The slices were then mechanically ground to approximately 200 μm and punched into 3 mm discs. To create electron transparent foils the discs were polished using a Struers Tenupol-3 electro-polisher with a 2% Nital solution cooled to -30ºC. Specimen foils of the following tempers were made for analysis: UA4 (aged for 4 hours at 160ºC), UA12 (aged for 12 hours at 160ºC) and PA-T8 (Aged for 30 hours at 160ºC).

A Philips Tecnai F20 200 KeV STEM was used for microstructural characterisation of each temper. The TEM was operated at 200 kV with an extraction

voltage of 4500 V. When carrying out imaging and diffraction the microscope was operated in microprobe mode with spot size 3 and a C2 aperture of 3 giving an approximate probe size ~10 nm full width at ten percent maximum (FWTM). When carrying out analytical (EDX) techniques the microscope was operated in scanning TEM (STEM) nanoprobe mode with spot size 6 and a C2 aperture of 2 giving a probe size of ~1-2 nm (FWTM). The operating pressure of the microscope was $<10^{-5}$ Pa.

The most potent strengtheners of AA2096 have been identified as δ' and T_1. Emphasis was placed on identifying these precipitates and distribution as a function of grain misorientation and temper. In particular T_1 precipitation near to and along grain boundaries was documented as a function of grain misorientation and temper.

3.2.1. Calculation of Grain Misorientation

To calculate the misorientation between the grains of interest convergent beam electron diffraction (CBED) was used. Starting with the first grain the sample was tilted to a zone axis (the intersection of several planes). The sample was then shifted, without tilting, to an adjacent grain. The CBED pattern for the adjacent grain was used to measure the distance *(D)* from the zone axis and direct beam. The angle between the zone axis and direct beam *(τ)* was calculated using the relationship:

$$\tan \tau = \frac{D}{L}$$

Where *L* represents the distance from the specimen to the screen (the camera length).

Throughout this study the grain boundaries of interest are relatively low-angle grain boundaries (see Figure 4.2). Anything over 9° is considered to be a high-angle grain boundary (Type I). For this reason when measuring the grain misorientation with CBED any grain that lies on a different zone axis to the reference grain can be considered high-angle and therefore a Type I grain boundary.

3.2.2. T_1 Precipitation Analysis as a Function of Grain Misorientation

To analyse the distribution of different precipitates selected area diffraction (SAD) was used. SAD patterns were taken from the [112] zone axis within the matrix. Super lattice reflections within the SAD pattern cause characteristic spots and streaks, indicating the presence of particular precipitate phases. By using a small objective aperture to highlight a particular feature a corresponding dark field image can be produced illuminating the relevant precipitate within the material. For example a streak within the SAD pattern, characteristic of T_1, can be highlighted. The corresponding dark field image of the material will illuminate T_1 precipitates within the matrix. This technique offers a qualitative assessment of the presence of precipitate phases and the distribution relative to the grain boundary and matrix. This is of particular use when looking for solute-depleted zones. SAD patterns and dark field images were taken of both the UA4 and UA12 tempers to observe evolution of T_1 as a function of aging time.

3.3 EDX Analysis of Copper Depletion Across Grain Boundaries.

An Oxford ISIS energy dispersive x-ray (EDX) spectrometer was used to assess copper depletion near to grain boundaries. Low and high angle grain boundaries in the UA4 temper were analysed and compared to similar misorientation grain boundaries in the UA12 temper. A nano-probe was used to take line scans across the grain boundary. A line of approximately 130 nm was used to characterise the chemical composition ratio of Al:Cu as a function of distance from the grain boundary. For a high count rate the most efficient angle to tilt a specimen relative to the detector is 18º. Therefore line scan experiments were conducted within the range of 15 – 25º to give a high count rate and reliable data. Furthermore for quality line scans, the boundary being analysed had to be edge-on to the detector. For this reason it was necessary to locate grain boundaries that were edge on to the detector at approximately 18º tilt. It was found that a collection live-time of 7 seconds per point offered reliable quantitative data with minimum beam drift. The areas under the primary $Al_{K\alpha}$ and $Cu_{K\alpha}$ peaks were used to semi-quantitatively measure the ratio of the two elements across the grain boundaries of interest.

4. RESULTS

4.1. Material

4.1.1. Alloy Composition

Table 1 shows the composition of AA2096 measured by IC plasma mass spectrometry and DC plasma emission spectrometry, taken from a previous study [20]. The measured results are tabulated along with the registered composition limits.

	Cu	Li	Mg	Zr	Zn	Ag	Fe	Si	Mn	Ti
Registered composition limits	2.3 - 3.0	1.3 – 1.9	0.25 – 0.8	0.04 – 0.18	0.25 Max	0.25 – 0.6	0.15 max	0.12 max	0.25 max	0.10 max
NASA-Langley Research Centre [1]	2.56 – 2.92	1.36 – 1.41	0.47 – 0.53	0.13 – 0.17	< 0.02	0.29 – 0.35	---	---	---	---
Burgess Laboratories [2]	2.84	1.72	0.48	0.52	0.012	0.36	0.051	0.034	0.001	0.05
Wah Chang Laboratories [2]	2.7	0.837	0.601	0.104	0.019	0.282	0.06	0.0395	< 0.005	0.041

Table 4.1. Alloy Composition (wt %) for AA2096

4.1.2. Grain Size and Morphology

Metallographic etching of AA2096 was carried out during a previous study [20]. The grains were un-recrystallised and the grain microstructure had been elongated by the extrusion process. The elongated grains were of the order of 100 to 150 μm by 10 to 30 μm (long transverse direction) produced in the extrusion/rolling direction. Low-angle sub-grains of the order of 10 μm by 10 μm were also present after all aging heat treatments.

[1] Measured via IC plasma mass spectrometry.
[2] Measured via DC plasma emission spectrometry.

4.2 Microstructural Characterisation

An examination of the microstructure for each temper was carried out using TEM and STEM. A qualitative study of T_1 precipitate density throughout grain matrices and along grain boundaries of various misorientations has been made using dark field TEM imaging for the UA4 and UA12 tempers. Selected area diffraction patterns (SAD) were taken for the UA4 and UA12 tempers to identify all precipitate phases present within the alloy as a function of aging time. The convergent beam electron diffraction (CBED) technique was used to calculate grain misorientation from the reference grain for the UA4 temper (Figures 4.3, 4.4, 4.10 and 4.26) and UA12 temper (Figures 4.37 and 4.38). An EDX study was carried out to qualitatively profile solute depletion across low, mid and high-angle grain boundaries of the UA4 temper (Figures 4.16 – 4.23 and 4.29 – 4.34) and a low-angle grain boundary of the UA12 temper (Figures 4.44 and 4.45).

4.2.1. TEM and EDX Study

4.2.1.1. AA2096 UA4 Temper. Area 1.

For the UA4 temper, three representative areas of interest are presented (note: numerous areas on several foils were studied). Figure 4.1 shows a bright field image of the first area of interest. With grain 1 as the reference grain, the sample was tilted to a [112] zone axis. A SAD pattern (Figure 4.2) from the reference grain was used to identify precipitate phases present in this temper condition. By comparison to SAD patterns from a previous study [20] on Al-Li-Cu-X (see appendix A.1), it was possible to identify bright, characteristic spots and streaks associated with superlattice reflections of the β', δ', and T_1 phases. Faint streaks associated with the S' phase can

also be seen. The faint streaks associated with S' indicate a low volume fraction of precipitates.

Convergent beam electron diffraction (CBED) was used to calculate the degree of misorientation between the reference grain (grain 1) and each neighbouring grain of interest. Grain 1 was tilted to a [112] zone axis. The sample was then shifted without tilt to each neighbouring grain. A CBED pattern was taken for each grain and the degree of misorientation was calculated by measuring the distance from the [112] zone axis. Figures 4.3a, 4.3b, 4.4a and 4.4b show (CBED) patterns taken from grains 2, 3, 4 and 5, respectively. The grain boundaries between the reference grain and grains 2, 3 and 4 were identified as low-angle boundaries (3 – 4.1º). Lying on a different zone axis [110] the grain boundary between the reference grain and grain 5 was identified as a high-angle boundary (Type I).

TEM dark field images were acquired for each grain boundary of interest. When viewing the SAD pattern, a small objective aperture was introduced to the back focal plane. The aperture was then shifted to allow electrons associated only with plate variants of the T_1 phase through. This procedure increases the contrast of T_1 precipitates within the resultant dark field image, assisting in their identification. In a previous study [20], the distribution of T_1 precipitates and grain misorientation were used to identify three types of grain boundary in the UA4 temper (see Table 4.2). Type I grain boundaries were associated with high-angle misorientations ($\geq$ 9º). Large, isolated T_1 precipitates were identified, growing along the grain boundary and quite often causing the boundary to pucker. Type II grain boundaries were associated

with relatively low-angle misorientations (≈3 – 9º). A single plate variant of T_1 with a small inter-particle spacing densely decorated the grain boundary. Unlike Type I grain boundaries the T_1 plates usually grow into the matrix (depending on the orientation of the plate) instead of along the boundary indicating a completely different growth mechanism. Type III grain boundaries were associated with very low-angle misorientations (≤ 3º). This type of boundary consisted of the same density of T_1 as that observed within the matrix.

Grain Boundary Type	Angle of Misorientation	T_1 precipitation on/near to grain boundary
Type I	≥ 9º	No continuous decoration of T_1 particles on the boundary One or two large T_1 precipitates growing along grain boundary causing puckering
Type II	3 – 9º	Near continuous decoration of fine T_1 precipitates growing into the matrix from grain boundary.
Type III	≤ 3º	No preferential precipitation on grain boundary. Same density of T_1 precipitates as that observed within the grain matrix.

Table 4.2. Grain boundary type comparing angle of misorientation with T_1 precipitate density.

Figure 4.5 shows a bright field grain map including the angles of misorientation for each grain of interest. Figure 4.6a shows the grain boundary between grains 1 and 2. The degree of misorientation at this boundary was calculated

to be 4.1º. Referring to the grain boundary types described above, this boundary would be a Type II boundary (it should be noted that the plate variant lying along the boundary is not in an optimal imaging condition but does appear to decorate the boundary).

Figure 4.6b depicts the grain boundary between grains 1 and 3. The degree of misorientation for this boundary was calculated to be 3º. This grain boundary is a Type II boundary in both angle of misorientation and the density of T_1 precipitates. A high density of fine T_1 precipitates can be observed, growing into the matrix, along the full length of the boundary.

Figure 4.7a shows the grain boundary between grains 1 and 5. The degree of misorientation for this boundary was calculated to be 64.02º. This boundary is consistent with a Type I boundary due to the high-angle of misorientation, but no grain boundary T_1 precipitation was observed anywhere along the full length of this boundary.

Figure 4.7b shows a lower magnification image of the triple point between grains 1, 2 and 3. Both boundaries appear to be decorated with T_1 particles. While the boundary between grains 1 and 3 shows the highest density of T_1 precipitates; this may be due to the plate variant of T_1 selected to image from the SAD pattern.

4.2.1.2. AA2096 UA4 Temper. Area 2.

Two grain boundaries, adjacent to the reference grain, were chosen to study (see Figure 4.8). The grain boundary between grains 1 and 6 was identified as a high-angle boundary. The grain boundary between grains 1 and 8 was identified as a low-angle boundary (3.8º). Figure 4.11 depicts the bright field grain map with the angles of misorientation for these grains. Figure 4.12 shows a dark field image highlighting T_1 precipitates throughout the reference grain and along the neighbouring grain boundaries (grains 6 and 8).

Figure 4.13a depicts a bright field image of the grain boundary between grains 1 and 6, with the corresponding dark field image, highlighting T_1, shown in Figure 4.13b. Large T_1 particles can be observed at the centre of the image following the grain boundary. In line with a Type I grain boundary as described above one large particle appears to cause a distinct puckering of the boundary. It follows that this boundary is consistent with a Type I grain boundary in both its high-angle of misorientation and T_1 precipitation density.

Figure 4.14 shows a typical EDX spectrum obtained in the vicinity of a grain boundary. With the characteristic Al and Cu Kα peaks identified, peak integration was used to semi-quantitatively calculate the Al:Cu ratio. This technique was used to examine a series of points on a line perpendicularly bisecting each grain boundary. These line scans aided in profiling the possible occurrence of solute depletion across grain boundaries as a function of grain misorientation and temper.

Figure 4.15 shows the approximate position, length and direction of each line scan taken across the grain 1 – grain 6 boundary. Figures 4.16a – 4.18b show the results with the grain boundary peak approximately at the centre of the scan and the reference grain (grain 1) to the left of this peak. Figures 4.16a and 4.16b show two line scans taken at a considerable distance from the large particle where little, if any, T_1 was present at the boundary. There is no evidence of Cu depletion approaching the boundary for either line scan. Figures 4.17a and 4.17b show two line scans taken directly across the large particle. There is some evidence of Cu depletion apparent in both of these line scans. Although only slight, there is a reduction in the Cu, approaching the grain boundary, more notably in Figure 4.17a. Figures 4.18a and 4.18b show two line scans taken in the vicinity of the large particle (within 10nm). The second line scan shows some evidence of Cu depletion. A Cu depleted zone of approximately 19nm width exists within grain 6.

Figure 4.19a shows a bright field image of the grain boundary between grains 1 and 8 with the corresponding dark field image, highlighting T_1 in Figure 4.19b. A near continuous distribution of fine T_1 precipitates can be observed along the full length of the boundary. A precipitate free zone may well be present, but if so, it is only slight. Although not completely denuded of T_1 precipitates a reduced density of the particles can clearly be observed approaching the grain boundary within grain 1. Twenty measurements were made along the grain boundary of the PFZ and the average width was calculated to be 26.4nm. The boundary is a Type II grain boundary in both angle of misorientation (3.8º) and T_1 precipitation density.

Figure 4.20 depicts the approximate position, direction and length of each line scan taken across the low-angle boundary (3.8º) between grains 1 and 8. Figures 4.21a – 4.23b show the results of each line scan taken across this grain boundary. For each line scan the grain boundary is the large peak approximately at the centre with the reference grain (grain 1) to the right of this peak. Although every care was taken to place the line scan across areas without intersecting boundary or matrix precipitates it can be seen that the line has crossed precipitates in several of the scans. Precipitates intersected by the electron probe can be seen as large peaks in the line scan. It has been noted in section 4.2.1.2. that the boundary between grains 1 and 8 is consistent with a Type II boundary. The boundary is highly decorated with fine T_1 precipitates and shows evidence of a T_1 PFZ. The reduced density of the Cu-rich T_1 phase, approaching the boundary, would suggest a reduction of the available Cu within the matrix. Each of the six line scans taken across this boundary appear to be in good agreement. To varying degrees each line scan shows a clear reduction in Cu approaching the grain boundary. It is interesting to note that the reduction in copper is more apparent on the reference grain side of each line scan (to the right of the grain boundary). The width of each Cu-depleted zone has been noted for this grain boundary and ranges from approximately 18 – 25nm, which is in line with the average width (26.4nm) of the PFZ measured above.

4.2.1.3. AA2096 UA4 Temper. Area 3.

Two grain boundaries adjacent to the reference grain were chosen to study. The grain boundary between grains 1 and 5 was identified as a high-angle boundary and the grain boundary between grains 1 and 2 was identified as a low-angle

boundary (3.51º). Figure 4.27 illustrates the bright field grain map and shows the angles of misorientation for the grains of interest. Figure 4.28a shows a dark field image highlighting T_1 precipitation throughout the reference grain and along the neighbouring grain boundaries. From this dark field image there appears to be little, if any, grain boundary T_1 precipitation along the boundary between grains 1 and 5. Although this boundary is consistent with a Type I grain boundary in respect of grain misorientation there are no large T_1 type precipitates apparent.

Figure 4.28b depicts a dark field image highlighting T_1 precipitation along the boundary between grains 1 and 2. The boundary is decorated with a high density of fine T_1 precipitates. Although there is some T_1 precipitation in the zone adjacent to the boundary, within grain 1, there is clearly a reduction in the density of the particles, approaching the boundary. The average width of the PFZ was calculated to be 25.7nm. Similar to the boundary observed in Figure 4.13b this boundary is consistent with a Type II grain boundary in both angle of misorientation and T_1 precipitation density.

Figure 4.29 depicts the approximate position, length and direction of three line scans taken across the boundary between grains 1 and 2. Figures 4.30a – 4.31 show the line scans. This boundary has been identified as a Type II grain boundary, having a low angle of misorientation (3.51º), dense boundary T_1 precipitation, and a narrow T_1 PFZ. Once again the three line scans show a clear reduction in Cu content, approaching the grain boundary from both sides. The width of the Cu depleted zones ranges from approximately 19 to 26nm. Referring to Figure 4.28b, the width of the

Cu depleted zone correlates well with the average width of the T_1 PFZ measured above (25.7nm).

Figure 4.32 illustrates the approximate position, length and direction of three line scans taken across the high-angle boundary between grains 1 and 5. Figures 4.33 – 4.34b show the result of each line scan. This boundary has been identified as a Type I grain boundary in respect of its high-angle of misorientation, absence of boundary T_1 precipitation and lack of a T_1 PFZ. However, there were no large, puckered T_1 type particles apparent along this grain boundary as previously seen along other high-angle grain boundaries in the UA4 temper. The three line scans taken correlate well with observations made from the dark field image. There is no clear drop in Cu approaching the grain boundary.

4.2.1.4. AA2096 UA12 Temper.

For the UA12 temper one area was studied as a comparison with the UA4 temper (Figure 4.35). From the SAD pattern (Figure 4.36) it is possible to identify characteristic spots and streaks associated with superlattice reflections of the β', δ', T_1, S' and Ω phases. Faint streaks associated with the θ' phase can also be observed indicating a low volume fraction of precipitates.

Four grain boundaries adjacent to the reference grain were chosen to study. The grain boundaries between the reference grain and grains 2 and 4 were identified as very low-angle boundaries (0.95º and 0.85º respectively). The grain boundaries

between the reference grain and grains 3 and 6 were identified as low-angle boundaries (3.51º and 7.15º respectively).

Figure 4.39 depicts the bright field grain map with the angles of misorientation. Figure 4.40 depicts a dark field image, highlighting T_1 precipitates throughout the reference grain and the adjacent grains of interest. It is immediately apparent that a much higher density of large T_1 precipitates exists throughout the reference grain when compared to the UA4 temper.

Figures 4.41a and 4.42a show the grain boundaries between the reference grain and grains 2 and 4, respectively. Both boundaries show a much higher density of fine T_1 particles than in the matrix (boundary between grain 1 and grain 2 to a lesser extent). However, unlike low-angle boundaries of the UA4 temper, no apparent PFZ can be observed with the area adjacent to the boundary having no less T_1 precipitation than the matrix. Figures 4.41b and 4.42b show the grain boundaries between the reference grain and grains 3 and 6, respectively. Both of these low-angle grain boundaries show no apparent T_1 precipitation for the plate variant imaged. Faint illumination of a T_1 plate variant can be seen decorating the boundary between grain 1 and grain 6.

EDX line scans were taken across a single, low-angle grain boundary to compare to the Cu depletion profiles measured in the UA4 temper. As discussed above, the boundary between grains 1 and 4 (figure 4.42a) contained a high density of fine T_1 precipitates but no apparent T_1 PFZ, as observed on the low-angle boundaries

of the UA4 temper. Figure 4.43 depicts the approximate position, length and direction of three line scans taken across the low-angle (0.85º) boundary between grains 1 and 4. Figures 4.44a – 4.45 show each line scan taken across this low-angle boundary. No obvious Cu depletion is apparent in any of the line scans. The lack of Cu depletion in the grain boundary area correlates well with the lack of a T_1 PFZ, observed in Figure 4.42a. From this example there appears to be a levelling of available matrix Cu in the vicinity of the grain boundary.

As a point of interest, the average size of T_1 precipitates within the matrix was calculated for both the UA4 and UA12 tempers. A sample group of twenty particles was selected across a wide area for each temper and measured. The results are displayed in Table 4.2 with the calculated standard deviation. The average particle length for the UA4 temper was 28nm with average length of a UA12 particle being distinctly larger at 52nm.

AA2096 Temper	Mean Grain Matrix T_1 Precipitate Length (nm)
AA2096 – UA4	28nm ± 8nm
AA2096 – UA12	52nm ± 11nm

Table 4.3. Measurement of average T_1 precipitate length within the grain matrix as a function of aging time.

4.3. Results Summary

For the UA4 tempe, 3 areas of interest were studied and one area of interest was studied for the UA12 temper. SAD patterns were taken from a [112] zone axis and compared to a previous study [20]. From these diffraction patterns it was possible

to identify characteristic spots and streaks associated with the following precipitate phases:

- UA4: β', δ', T_1, and faint streaks associated with S'
- UA12: β', δ', T_1, S', Ω and faint streaks associated with θ'

The CBED technique was used to measure the degree of grain misorientation for all grain boundaries studied. Dark field images were acquired to analyse T_1 precipitate density near to and on all grain boundaries. The grain misorientation in conjunction with the T_1 precipitate density was used to identify three types of grain boundary in the UA4 temper (see Table 4.2.). EDX line scan analysis was used to investigate the occurrence of copper solute depletion as a function of grain misorientation and aging time. Areas 2 and 3 of the UA4 temper and area 1 of the UA12 temper were analysed using this technique.

From area 1 of the UA4 temper the boundary between grain 1 and grain 3 and the boundary between grain 1 and grain 2 were consistent with a Type II boundary in both angle of misorientation and T_1 precipitate density. A near continuous decoration of fine T_1 precipitates was visible along the full length of the boundary. The boundary between grain 1 and grain 5 was consistent with a Type I boundary in angle of misorientation and similar in respect of T_1 precipitate density although no large isolated precipitates were observed in the limited area analysed.

From area 2 of the UA4 temper one boundary (grains 1 – 6) was consistent with a Type I grain boundary with one large T_1 particle growing along the boundary,

while another (grains 1 – 8) was consistent with a Type II boundary showing a PFZ of approximately 26nm and a heavy decoration of fine T_1 precipitates. EDX analysis of the Type I boundary revealed no copper depletion when line scans were taken away from the large particle but some copper depletion was apparent when the line scans were taken directly across the large particle. EDX line scans across the Type II grain boundary showed copper depletion in the range of 18 – 25nm, which is consistent with the PFZ observed.

From area 3 of the UA4 temper one boundary (grains 1 – 5) was consistent with a type II boundary in angle of misorientation and T_1 precipitate density, with a PFZ of approximately 26nm. A second boundary was identified as a Type I grain boundary in angle of misorientation but not in respect of T_1 precipitate density. EDX line scans of the Type II boundary showed copper depletion in the range of 19 – 26nm while the Type I boundary showed no signs of copper solute depletion.

From the UA12 temper dark field analysis of four grain boundaries ranging from 0.85º to 7.15º showed no PFZs. EDX analysis of a very low-angle boundary showed no sign of copper solute depletion.

	Copper Depletion		T1 PFZ		Precipitates Phases Present
Grain Boundary Misorientation	Low-Angle	High-Angle	Low-Angle	High-Angle	
UA4	Yes	No	Yes	No	β', δ', T1 and faint S'
UA12	na	na	No	No	β', δ', T_1, S', Ω and faint θ'

Table 4.4. Summary of observed results.

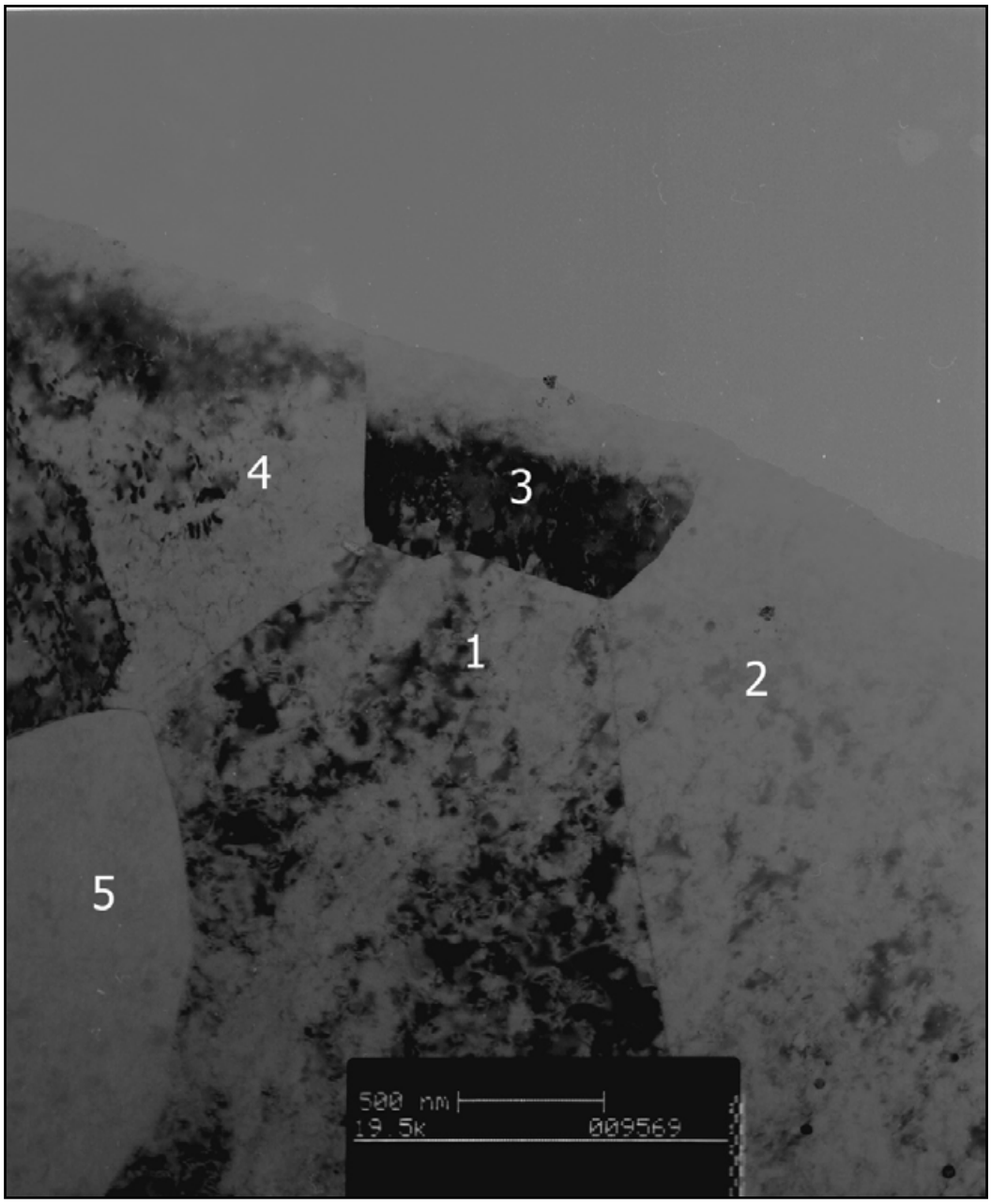

Figure 4.1. TEM Study: AA2096 UA4 Temper. Area 1. Bright Field Grain Map.
Grain 1 was taken as the reference grain and tilted to a [112] zone axis. From this grain, convergent beam electron diffraction (CBED) was used to measure the degree of misorientation of the adjacent grains from the reference. Dark field images were used to highlight T_1 precipitates within the reference grain.

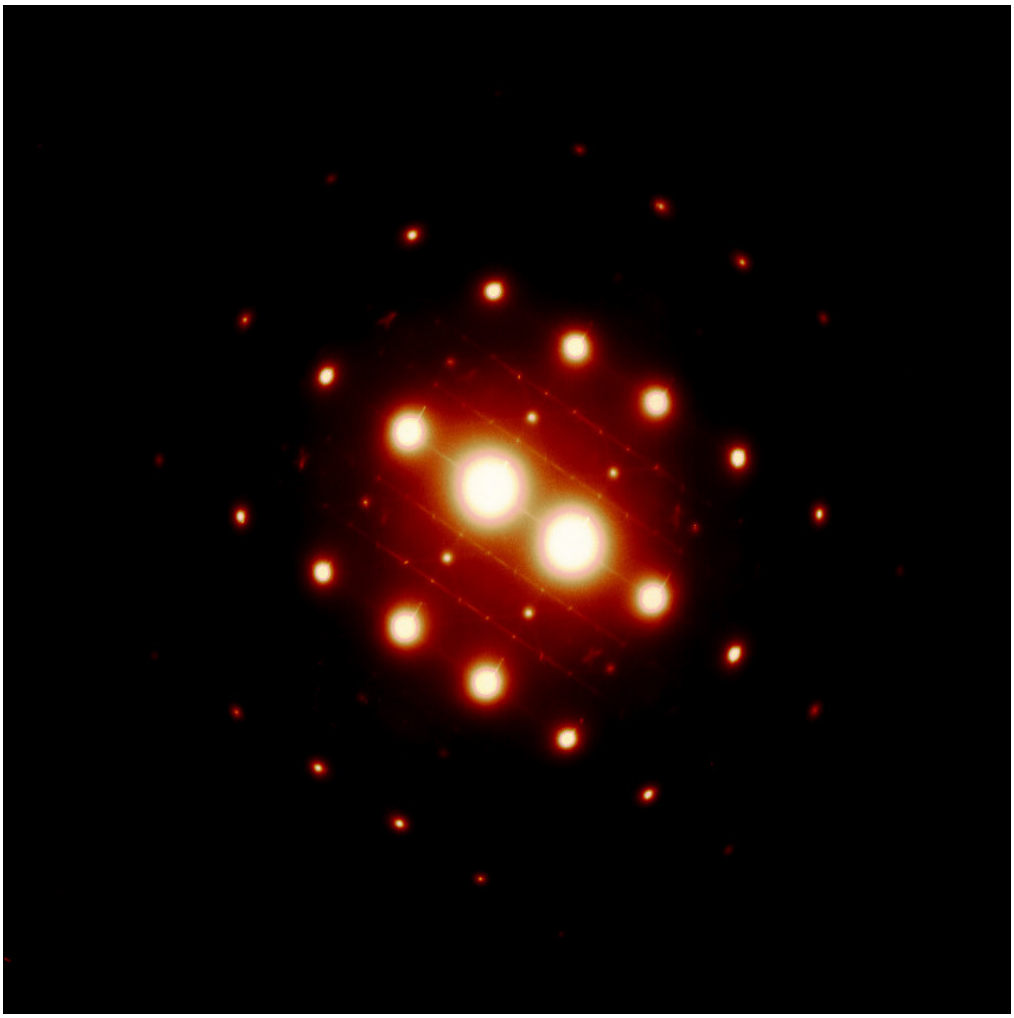

Figure 4.2. TEM Study: AA2096 UA4 Temper. Area 1. Diffraction Pattern.
Selected area diffraction pattern of a [112] zone axis. Bright spots and streaks associated with the β', δ' and T_1 phases are clearly visible. Faint streaks associated with S' phase can also be seen.

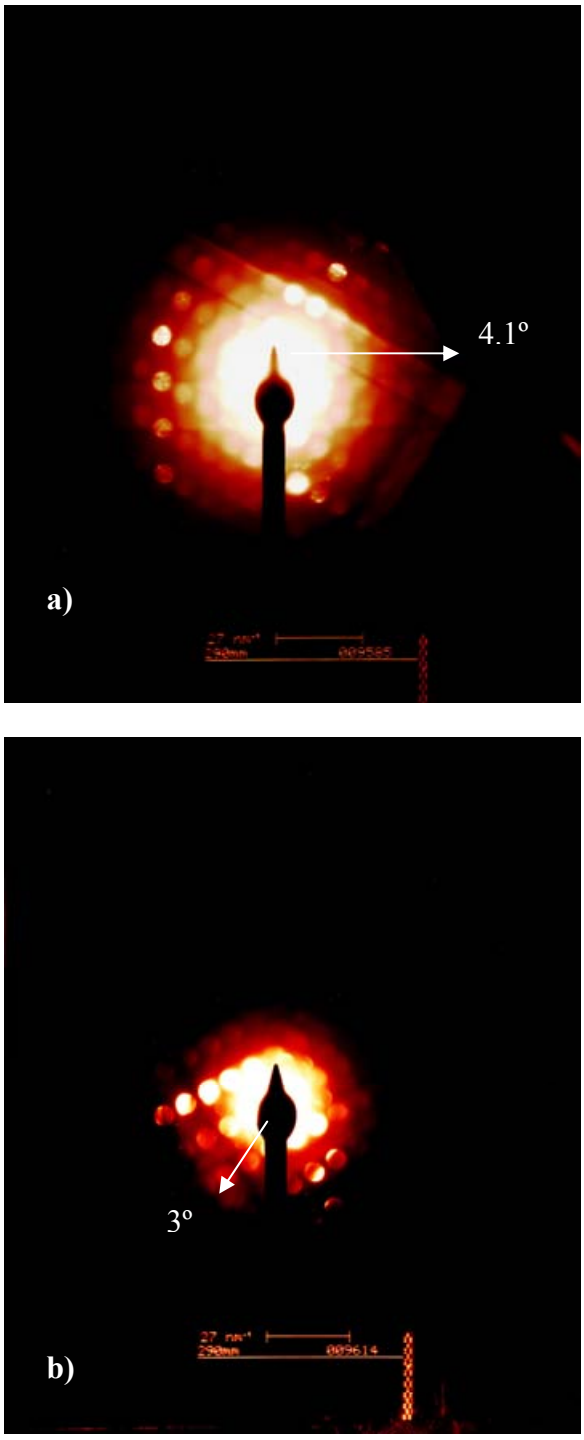

Figure 4.3. TEM Study: AA2096 UA4 Temper. Area 1. CBED.
Convergent beam electron diffraction (CBED) patterns of the following grains from Figure 1: a) Grain 2, b) Grain 3. The degree of misorientation from the reference grain is illustrated for each CBED pattern.

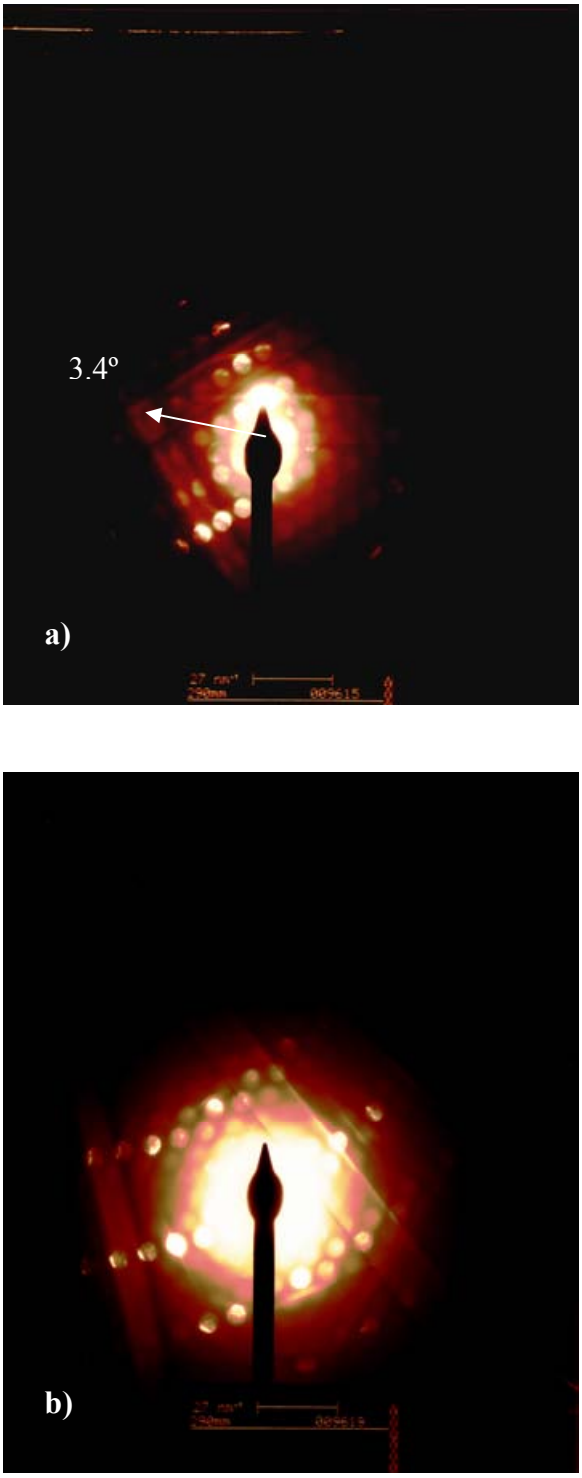

Figure 4.4. TEM Study: AA2096 UA4 Temper. Area 1. CBED.
Convergent beam electron diffraction (CBED) patterns of the following grains from Figure 2: a) Grain 4, b) Grain 5. The degree of misorientation from the reference grain is illustrated for grain 4 whereas grain 5 lies on [110] zone axis and is therefore designated as a high-angle grain boundary (Type I).

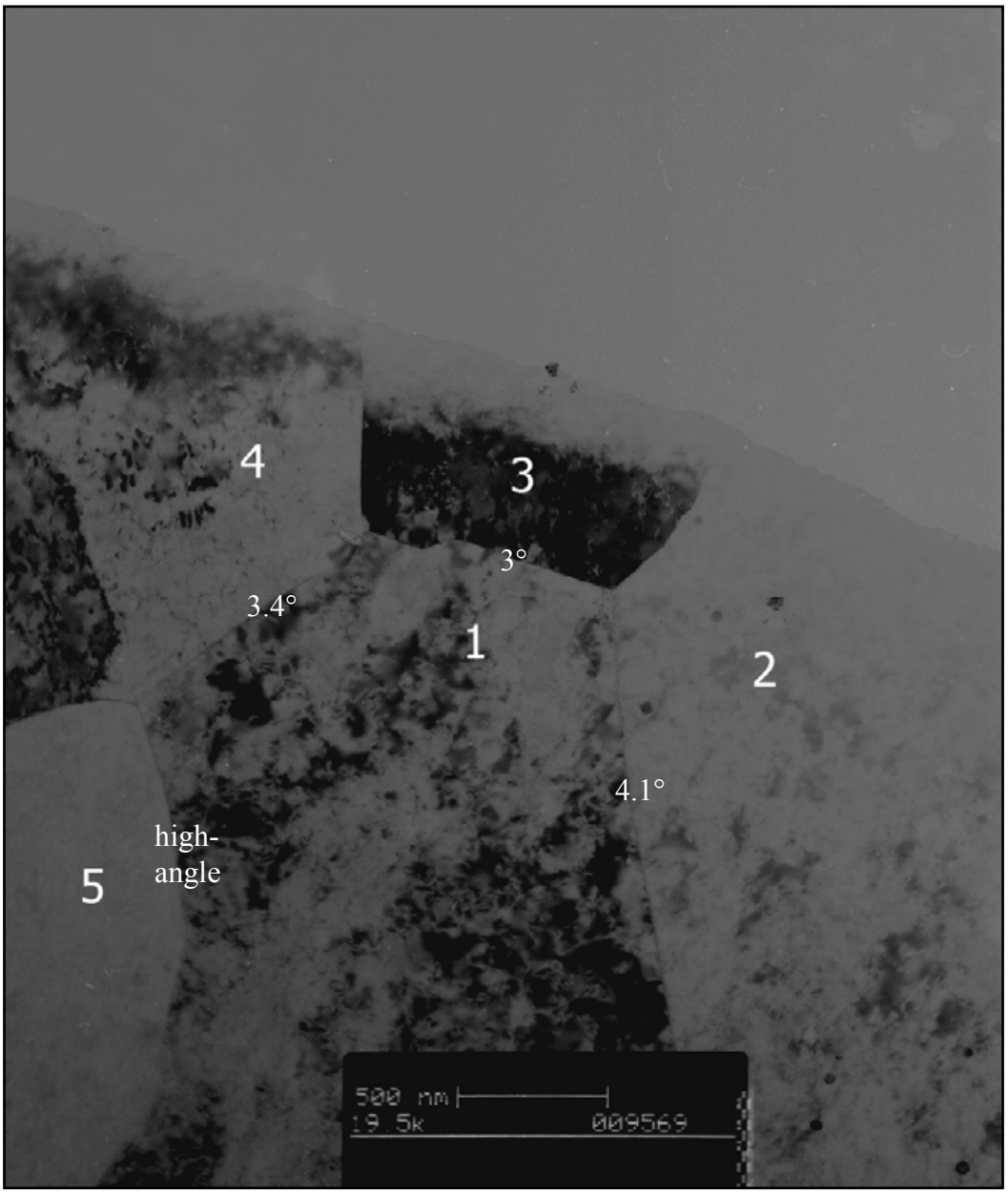

Figure 4.5. TEM Study: AA2096 UA4 Temper. Area 1. Bright Field Grain Map.

Bright field grain map from Figure 1, illustrating angles of misorientation for the grain boundaries of interest.

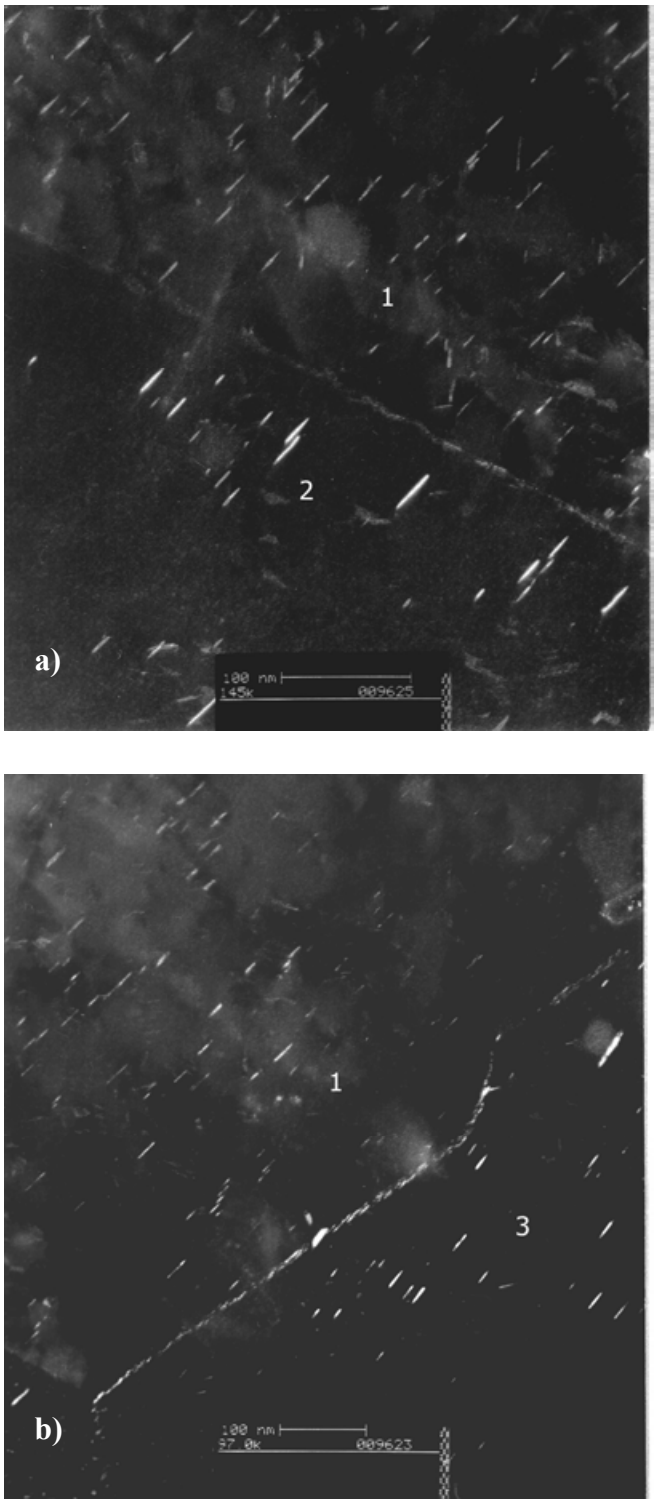

Figure 4.6. TEM Study: AA2096 UA4 Temper. Area 1. Dark Field Images.
a) Dark field TEM image highlighting one variant of the T_1 precipitate throughout the matrix and along the boundary of grains 1 and 2. b) Dark field TEM image highlighting one variant of the T_1 precipitate throughout the matrix and along the boundary of grains 1 and 3.

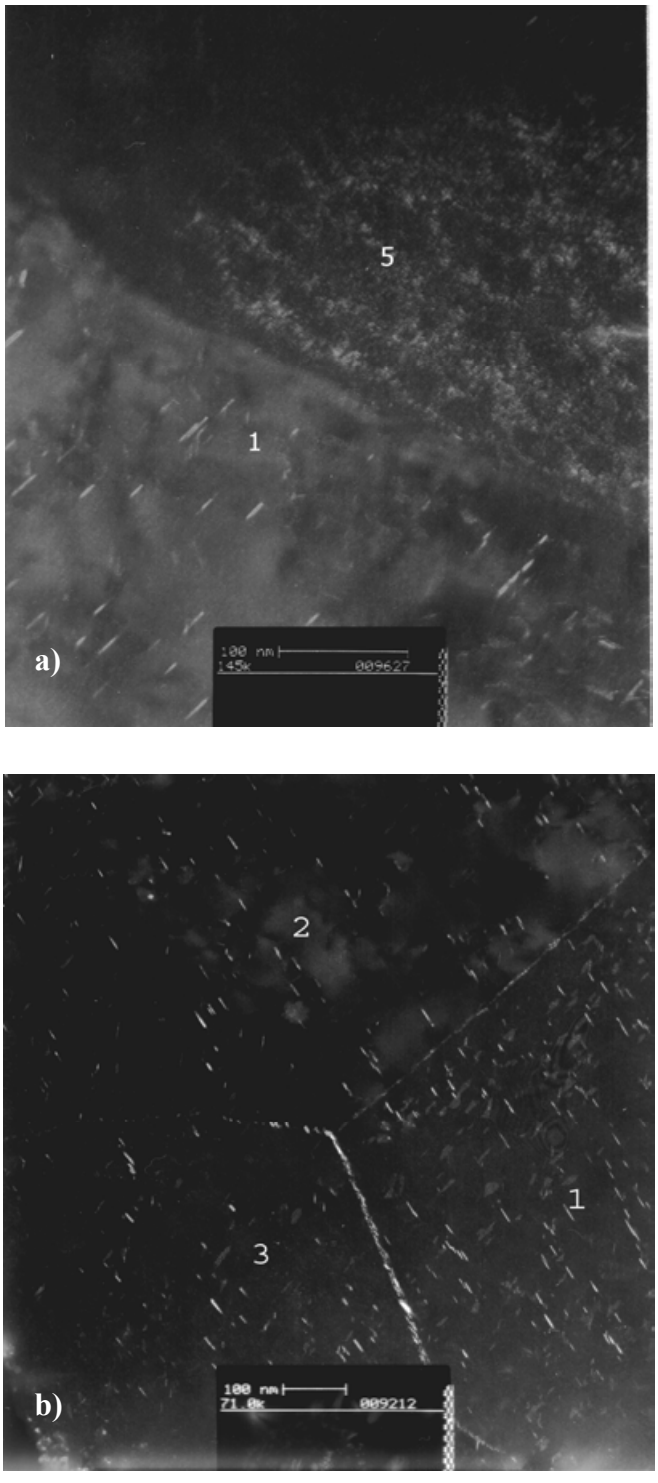

Figure 4.7. TEM Study: AA2096 UA4 Temper. Area 1. Dark Field Images.
a) Dark field TEM image highlighting one variant of the T_1 precipitate throughout the matrix and along the boundary of grains 1 and 5. b) Dark field TEM image highlighting one variant of the T_1 precipitate throughout the matrix and near to the triple point of grains 1, 2 and 3.

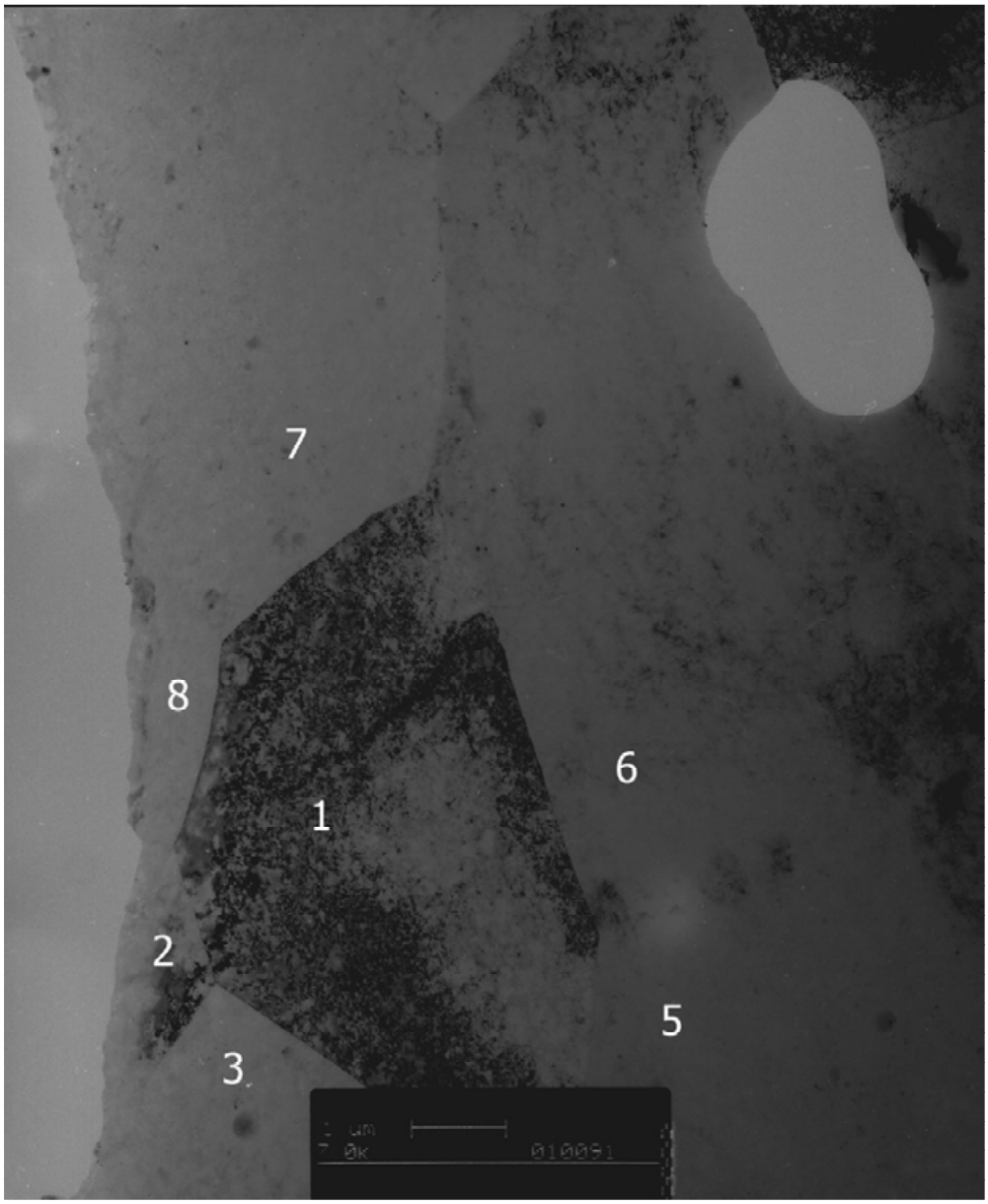

Figure 4.8. TEM Study: AA2096 UA4 Temper. Area 2. Bright Field Grain Map.
Grain 1 was taken as the reference grain and tilted to a [112] zone axis. From this grain, convergent beam electron diffraction (CBED) was used to measure the degree of misorientation of the adjacent grains of interest from the reference. Dark field images were used to highlight T_1 precipitates within the reference grain.

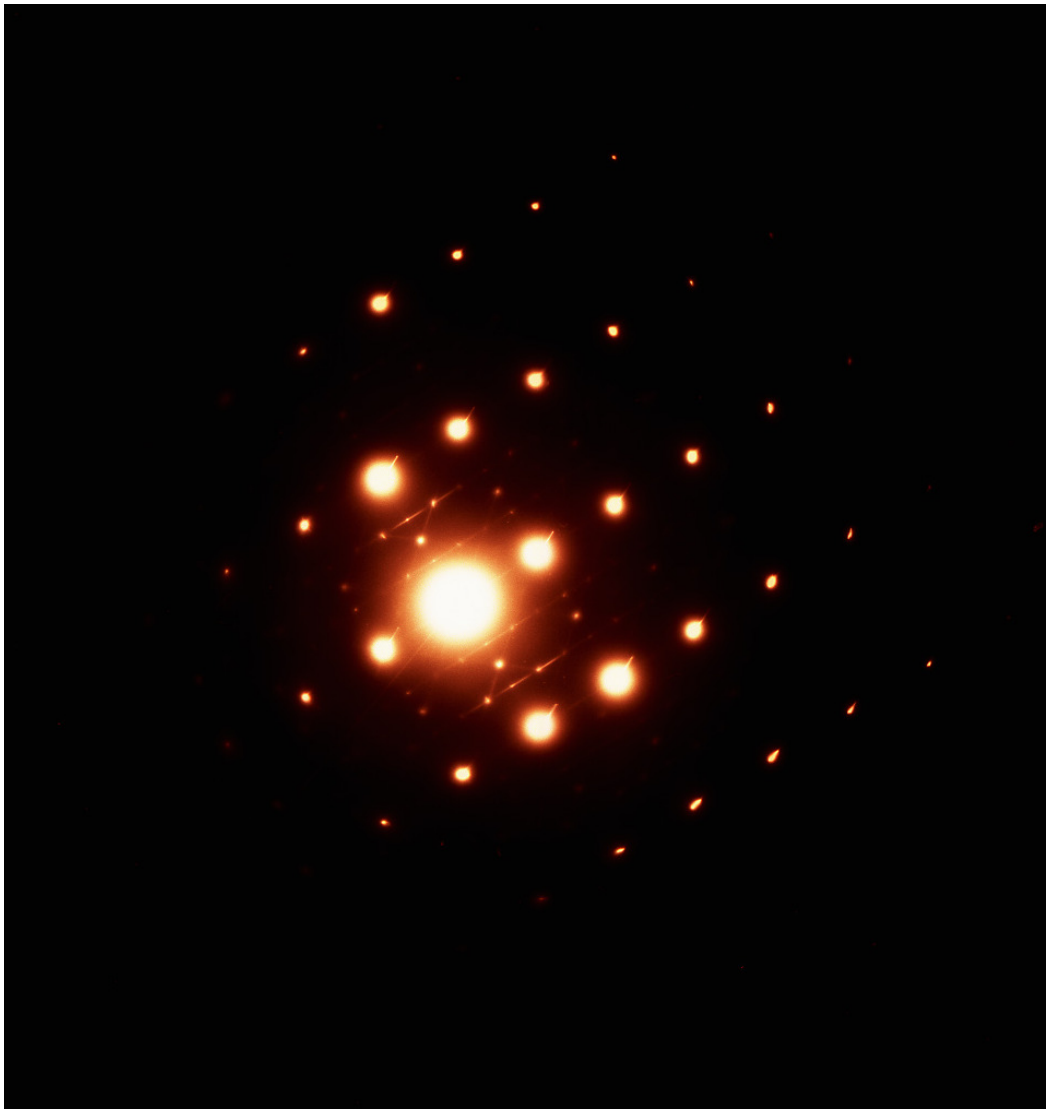

Figure 4.9. TEM Study: AA2096 UA4 Temper. Area 2. Diffraction Pattern.
Selected area diffraction pattern of a [112] zone axis. Bright spots and streaks associated with the β', δ' and T_1 phases are clearly visible. Faint streaks associated with S' phase can also be seen.

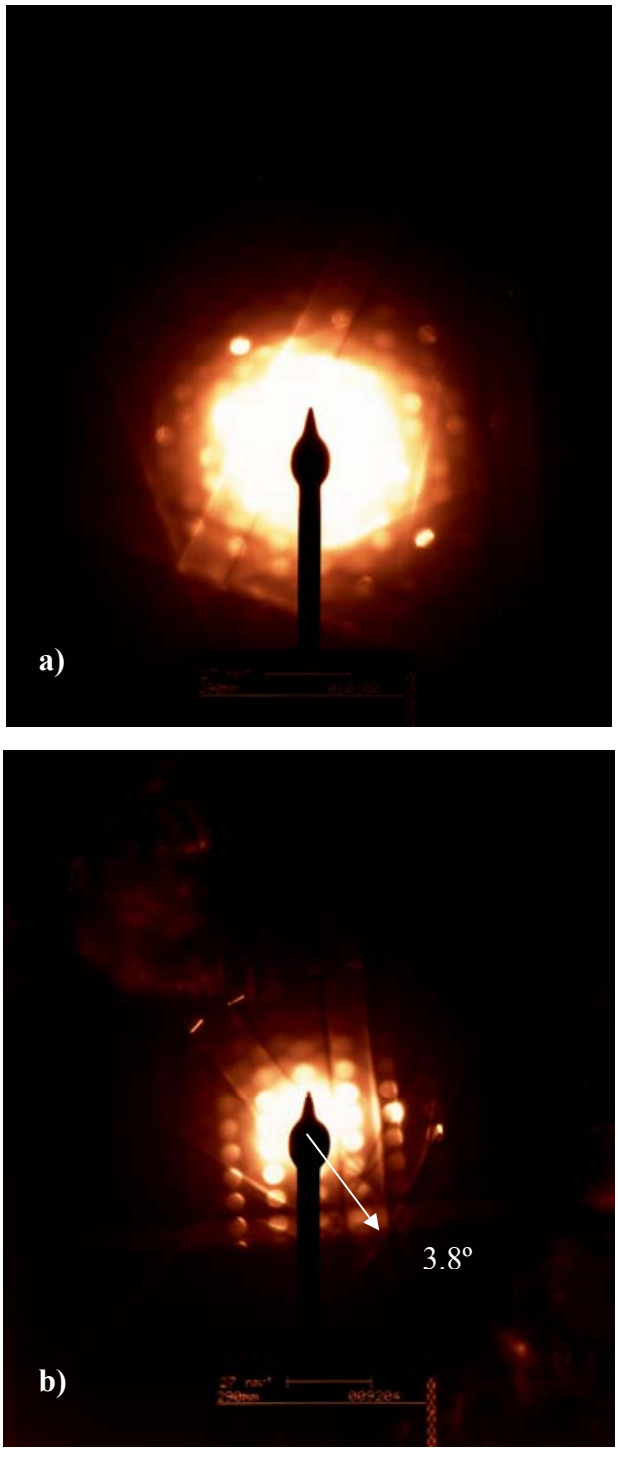

Figure 4.10. TEM Study: AA2096 UA4 Temper. Area 2. CBED.
Convergent beam electron diffraction (CBED) patterns of the following grains from Figure 7: a) Grain 6, b) Grain 8. The degree of misorientation from the reference grain is illustrated for grain 8 whereas grain 6 lies on [110] zone axis and is therefore designated as a high-angle grain boundary (Type I).

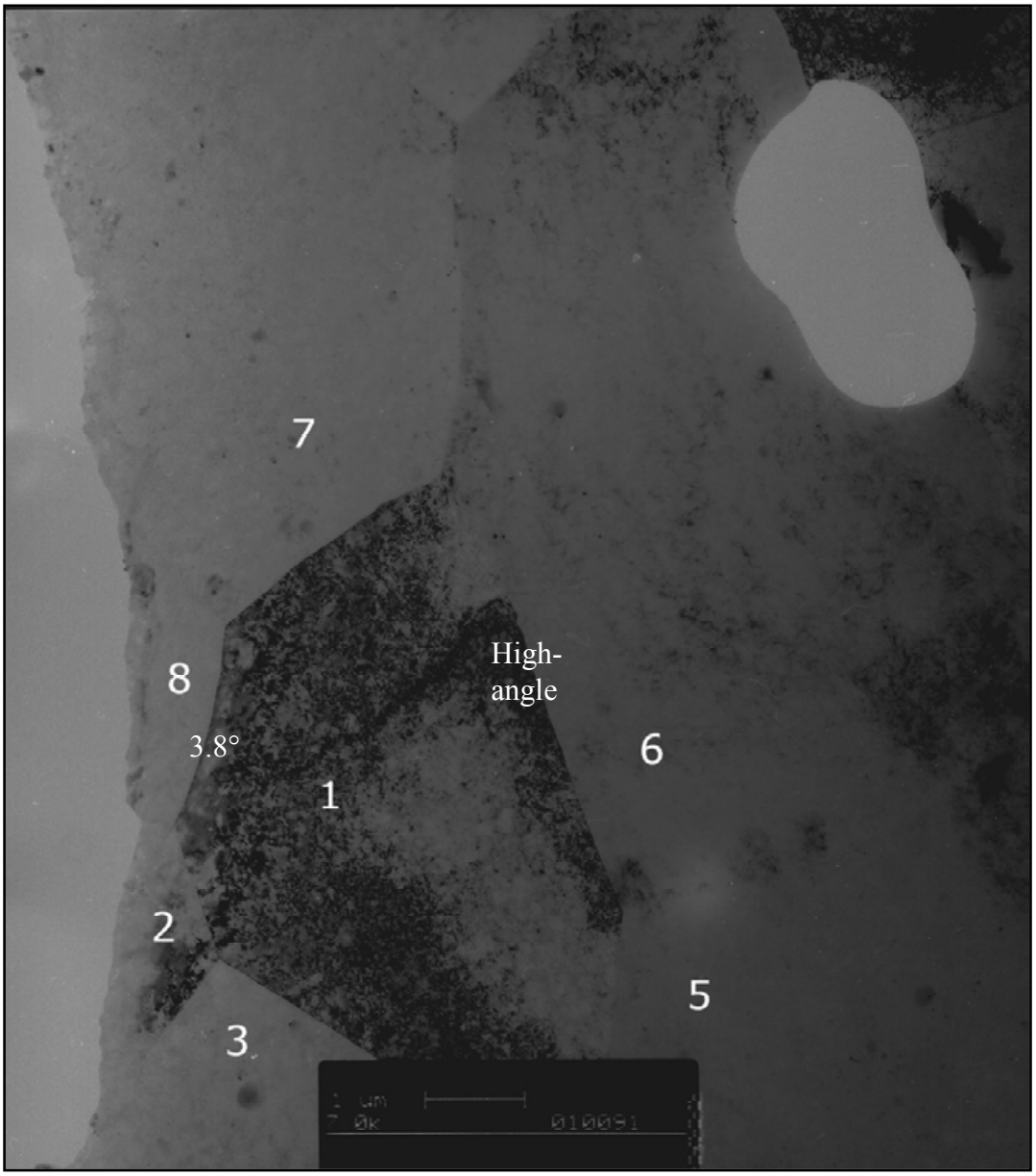

Figure 4.11. TEM Study: AA2096 UA4 Temper. Area 2. Bright Field Grain Map.

Bright field grain map from Figure 8, illustrating angles of misorientation for the grain boundaries of interest (grains 6 and 8).

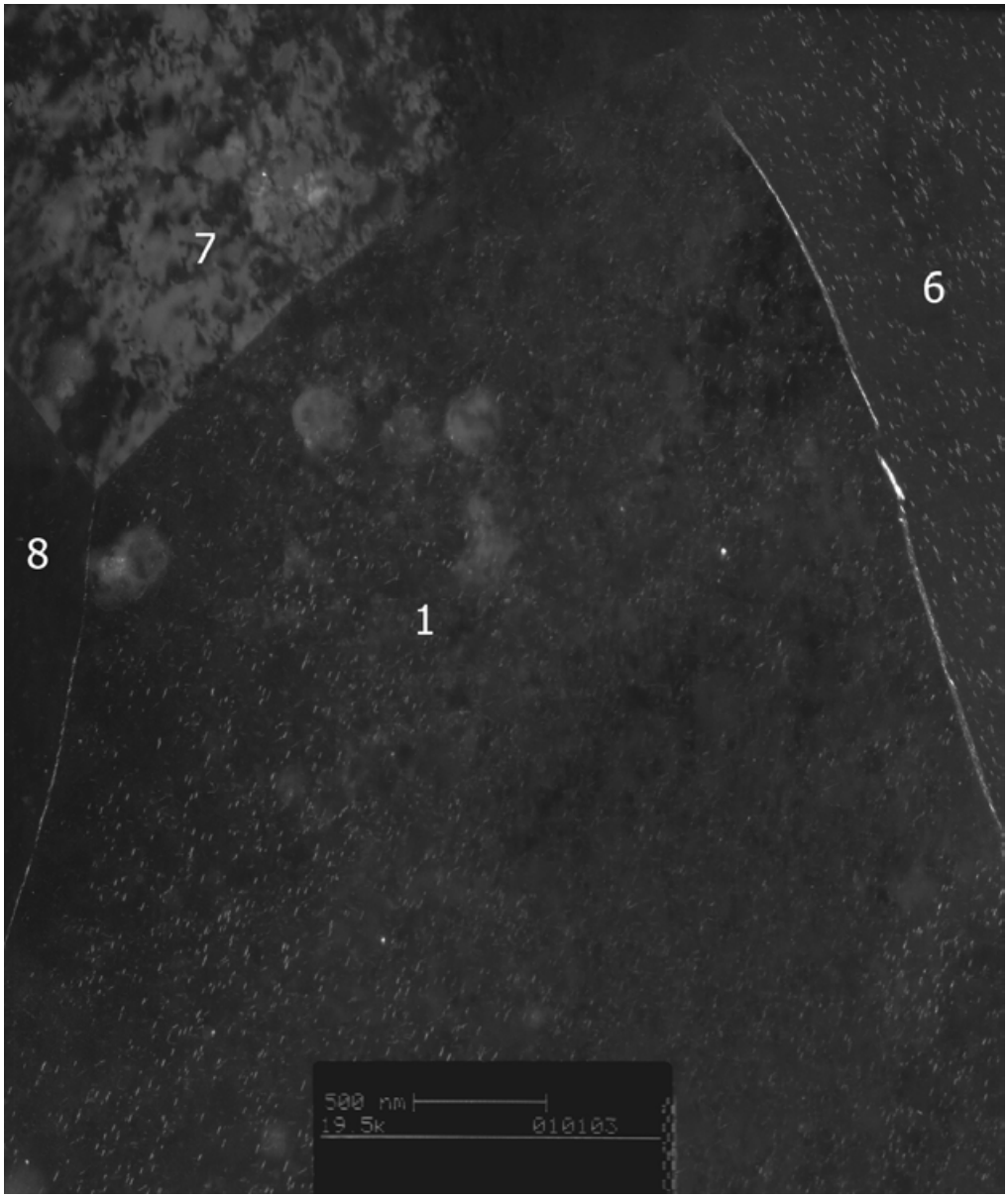

Figure 4.12. TEM Study: AA2096 UA4 Temper. Area 2. Dark Field Image.
a) Dark field TEM image highlighting one variant of the T_1 precipitate throughout the matrix of grain 1 and along the adjacent boundaries of interest (grains 6 and 8).

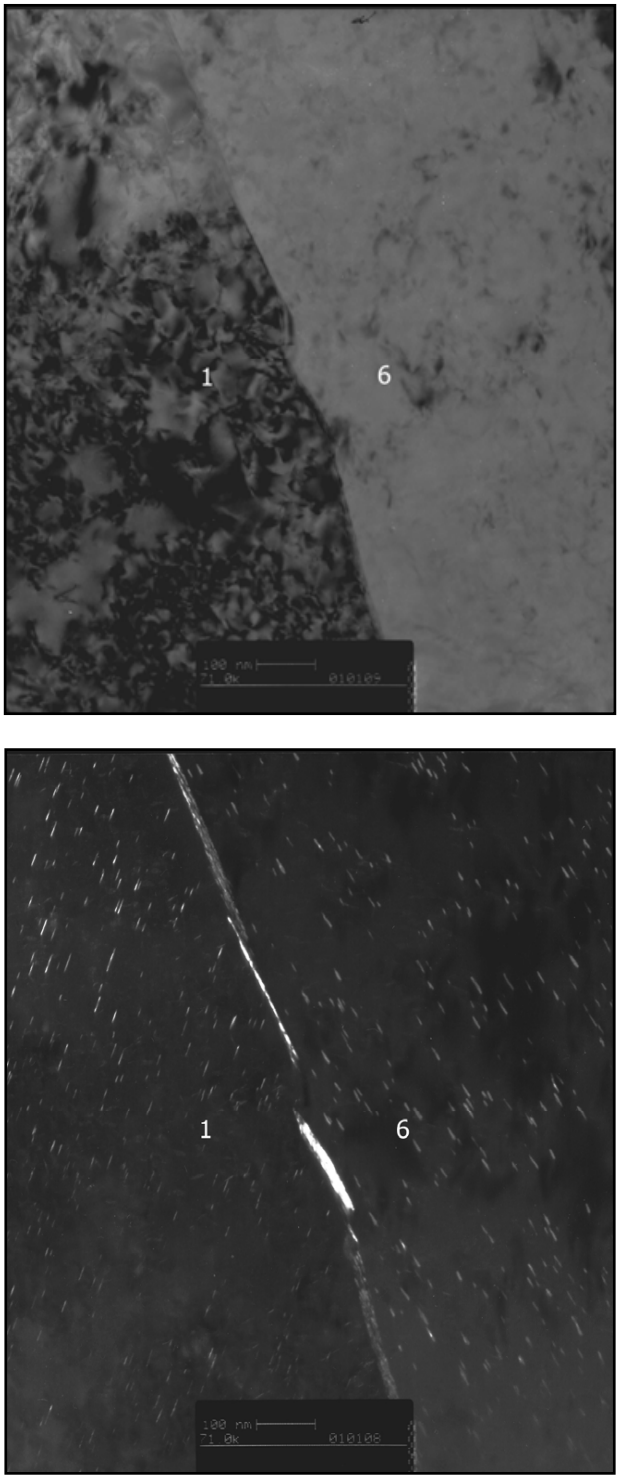

Figure 4.13. TEM Study: AA2096 UA4 Temper. Area 2. Bright and Dark Field Images.
a) Bright field TEM image of the boundary between grains 1 and 6. b) Corresponding dark field TEM image highlighting one variant of the T_1 precipitate throughout the matrix of grains 1 and 6 as well as along the grain boundary.
Note: Line scans were taken across the large particle in the centre of the image and compared to line scans close to the particle and some distance from the particle. See Figures 4.16 - 4.18

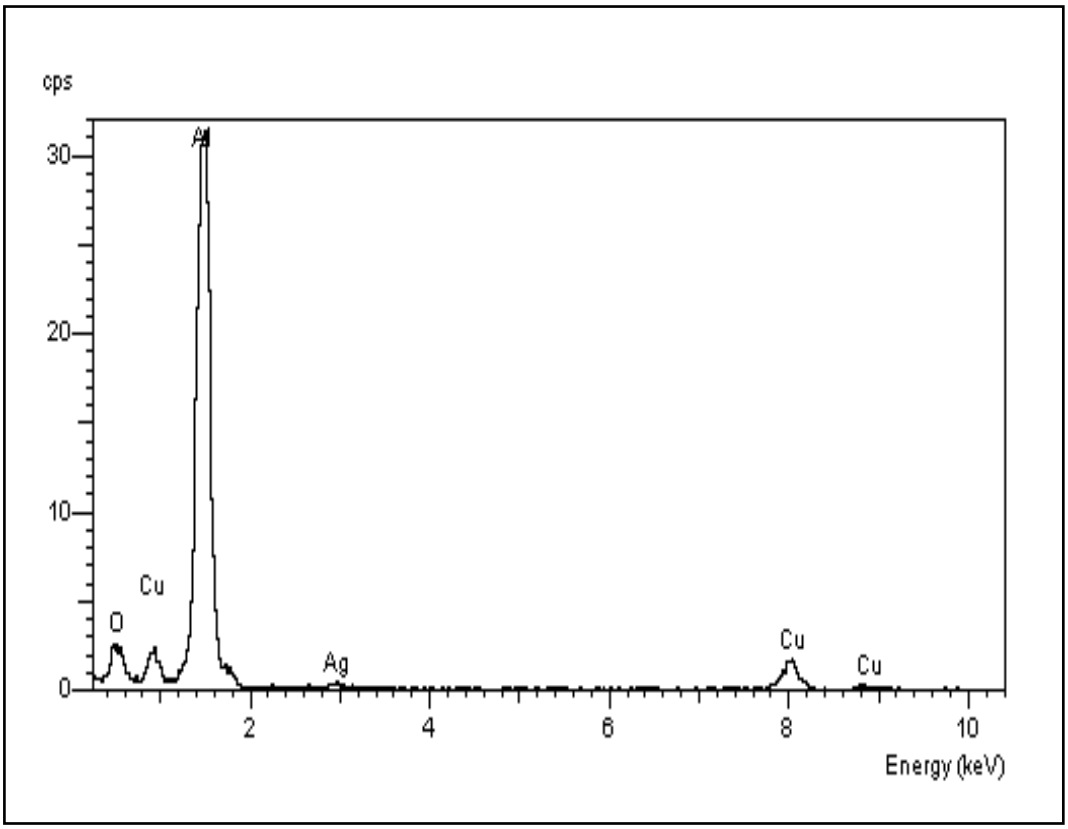

Figure 4.14. TEM Study: AA2096 UA4 Temper. Area 2. Typical EDX Spectra.
Typical energy dispersive X-ray (EDX) spectra obtained at 200 kV close to a grain boundary. Characteristic peaks for aluminium and copper are identified. The area beneath the primary Kα peaks was used to calculate the Al:Cu chemical composition ratio for a given distance fron the grain boundary. This technique was used to estimate the at.wt% of copper along the following line scans.

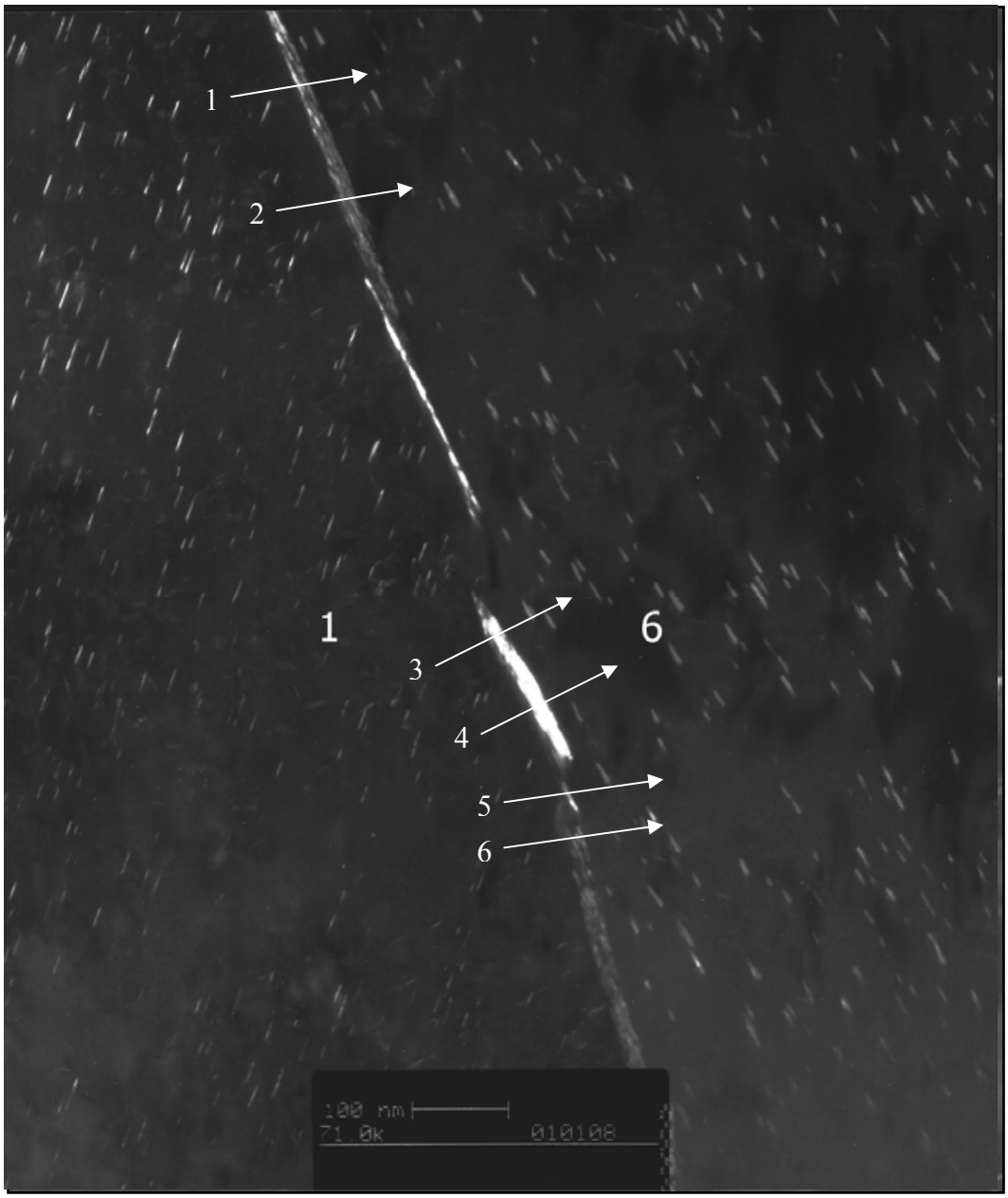

Figure 4.15. TEM Study: AA2096 UA4 Temper. Area 2. EDX Line Scans.

The markers show the approximate location, length and direction of the EDX line scans taken across the boundary between grains 1 and 6. The lines are numbered to correspond with the line scan results illustrated in Figures 4.16 - 4.18

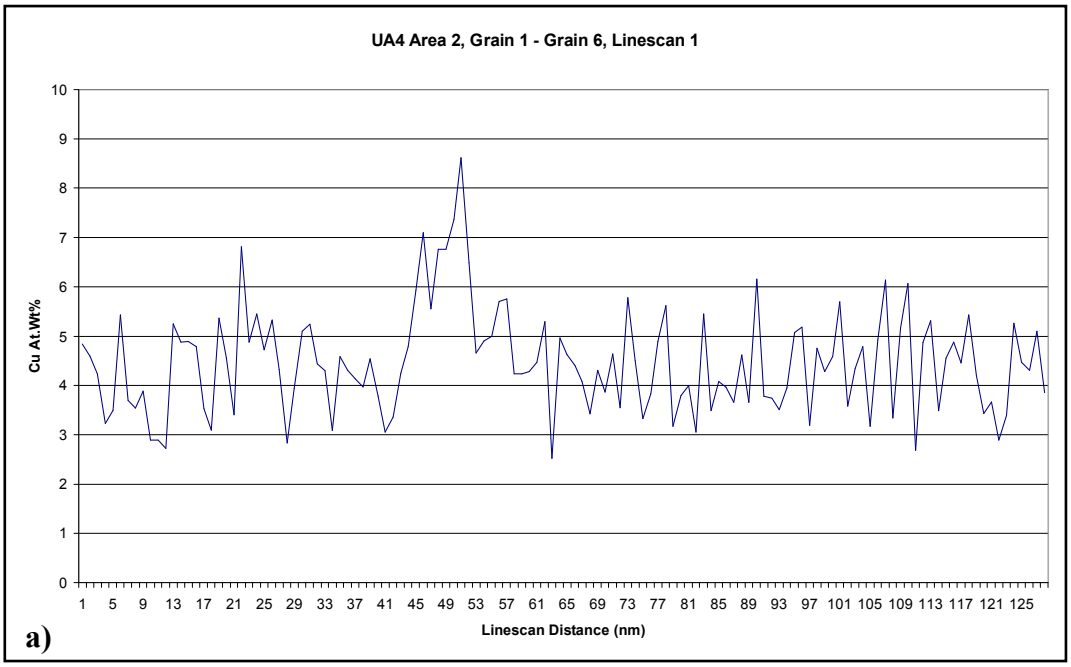

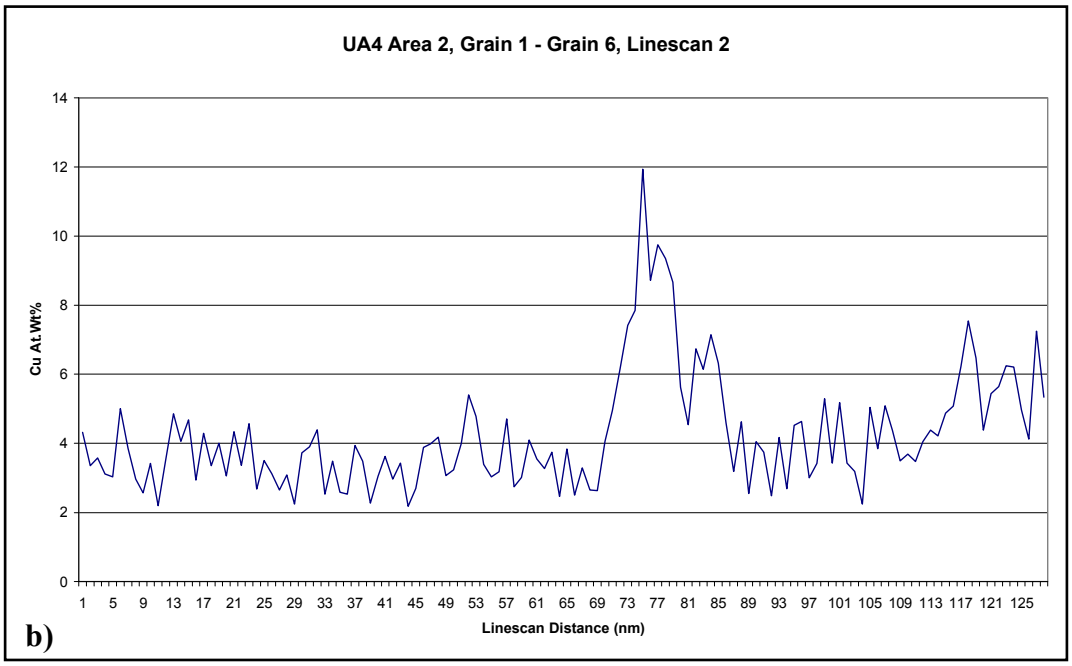

Figure 4.16. TEM Study: AA2096 UA4 Temper. Area 2. EDX Line scans across a high-angle grain boundary.
Energy dispersive X-ray (EDX) line scan analysis across the boundary of grain 1 and grain 6: a) Line scan 1. b) Line scan 2. Refer to Figure 4.15.
Note: Line scans taken away from the large particle.

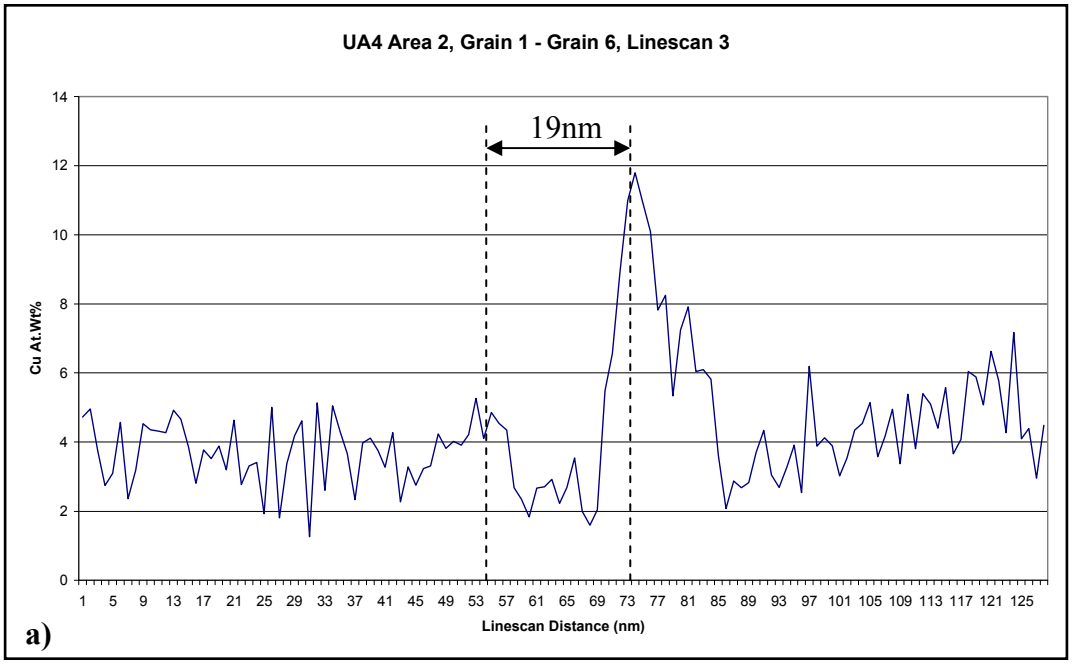

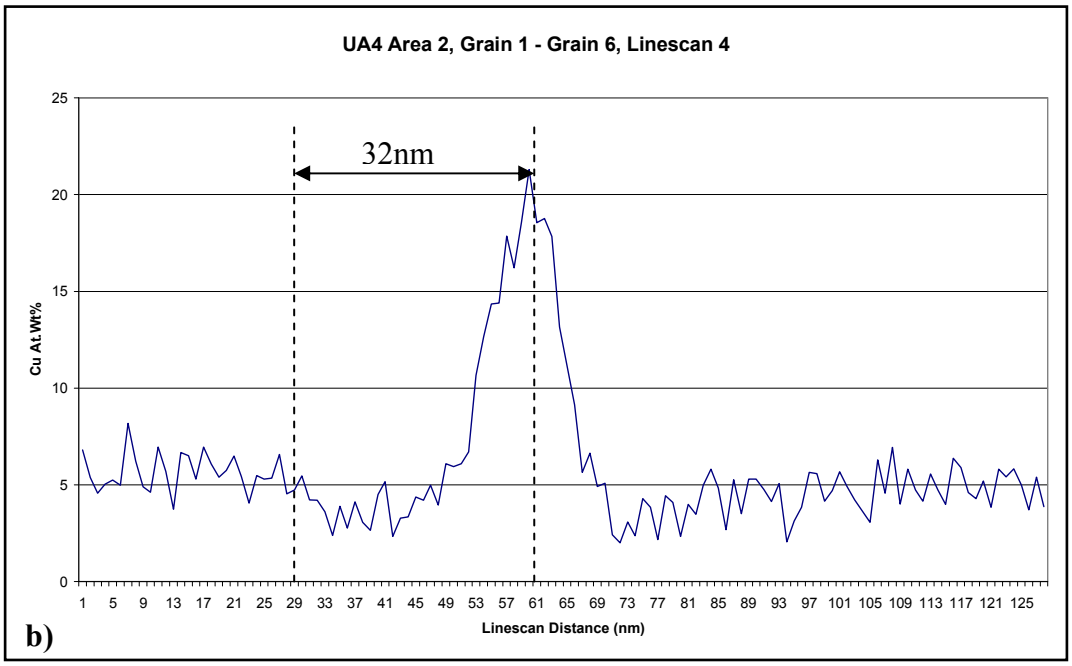

Figure 4.17. TEM Study: AA2096 UA4 Temper. Area 2. EDX Line scans across a high-angle grain boundary.
Energy dispersive X-ray (EDX) line scan analysis across the boundary of grain 1 and grain 6: a) Line scan 3. b) Line scan 4. Refer to Figure 4.15. Approximate width of possible Cu depleted zones is indicated.
Note: Line scans taken across the large particle.

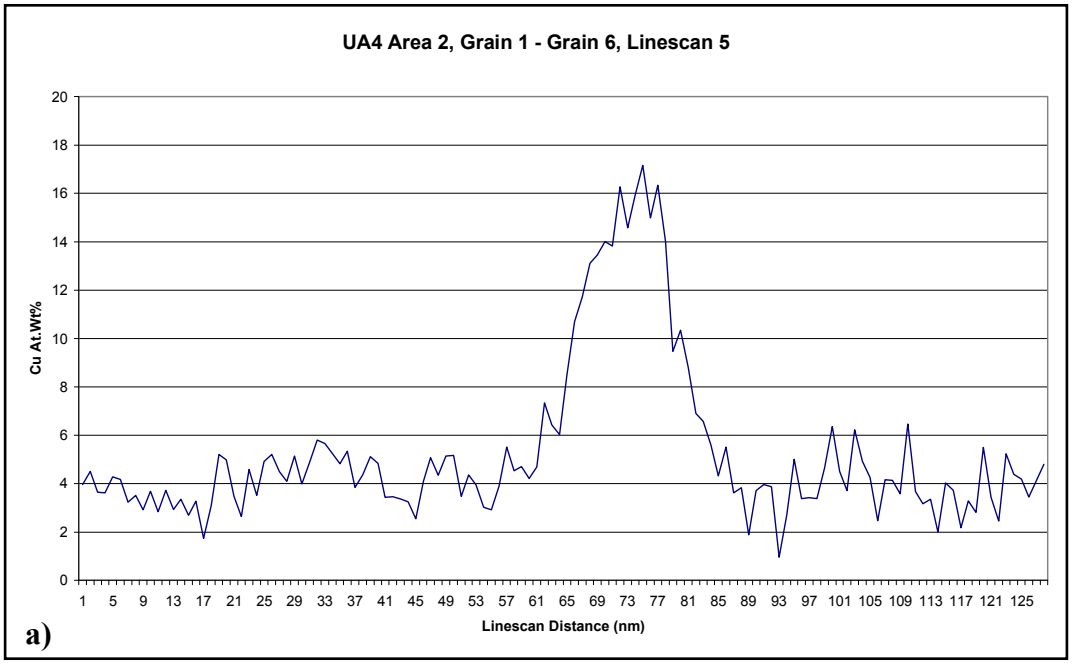

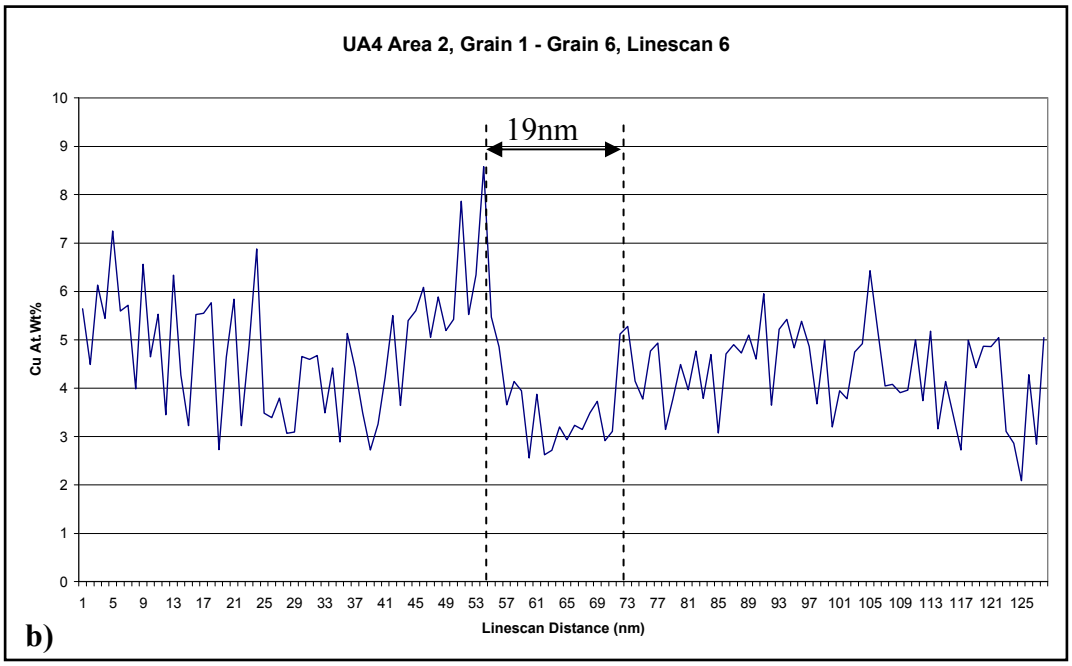

Figure 4.18. TEM Study: AA2096 UA4 Temper. Area 2. EDX Line scans across a high-angle grain boundary.
Energy dispersive X-ray (EDX) line scan analysis across the boundary of grain 1 and grain 6: a) Line scan 5. b) Line scan 6. Refer to Figure 4.15. The width of possible Cu depleted zones is indicated.
Note: Line scans taken in close proximity to the large particle.

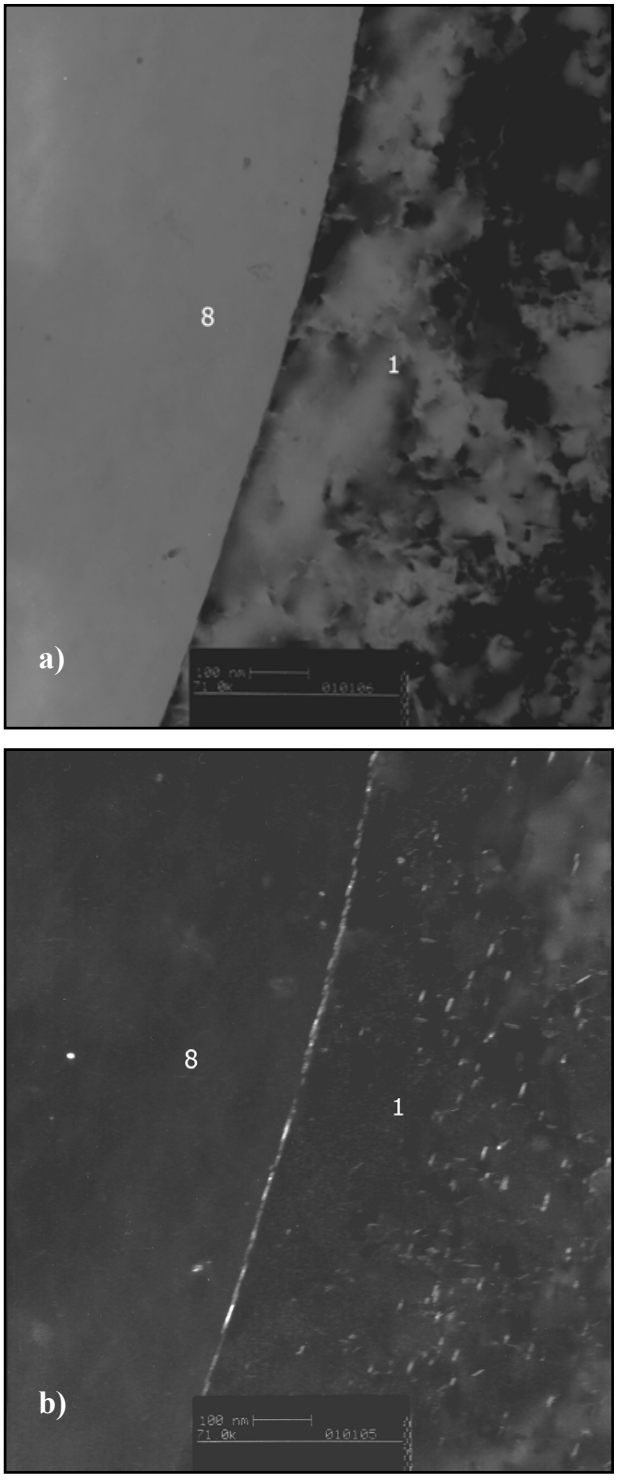

Figure 4.19. TEM Study: AA2096 UA4 Temper. Area 2. Bright and Dark Field Images.
a) Bright field TEM image of the boundary between grains 1 and 8. b) Corresponding dark field TEM image highlighting one variant of the T_1 precipitate throughout the matrix of grain 1 and along the boundary of grains 1 and 8. An apparent precipitate free zone (PFZ) is apparent on the grain 1 side of the boundary.
Note: Line scans were taken at various points along the boundary. See Figures 4.21 – 4.23.

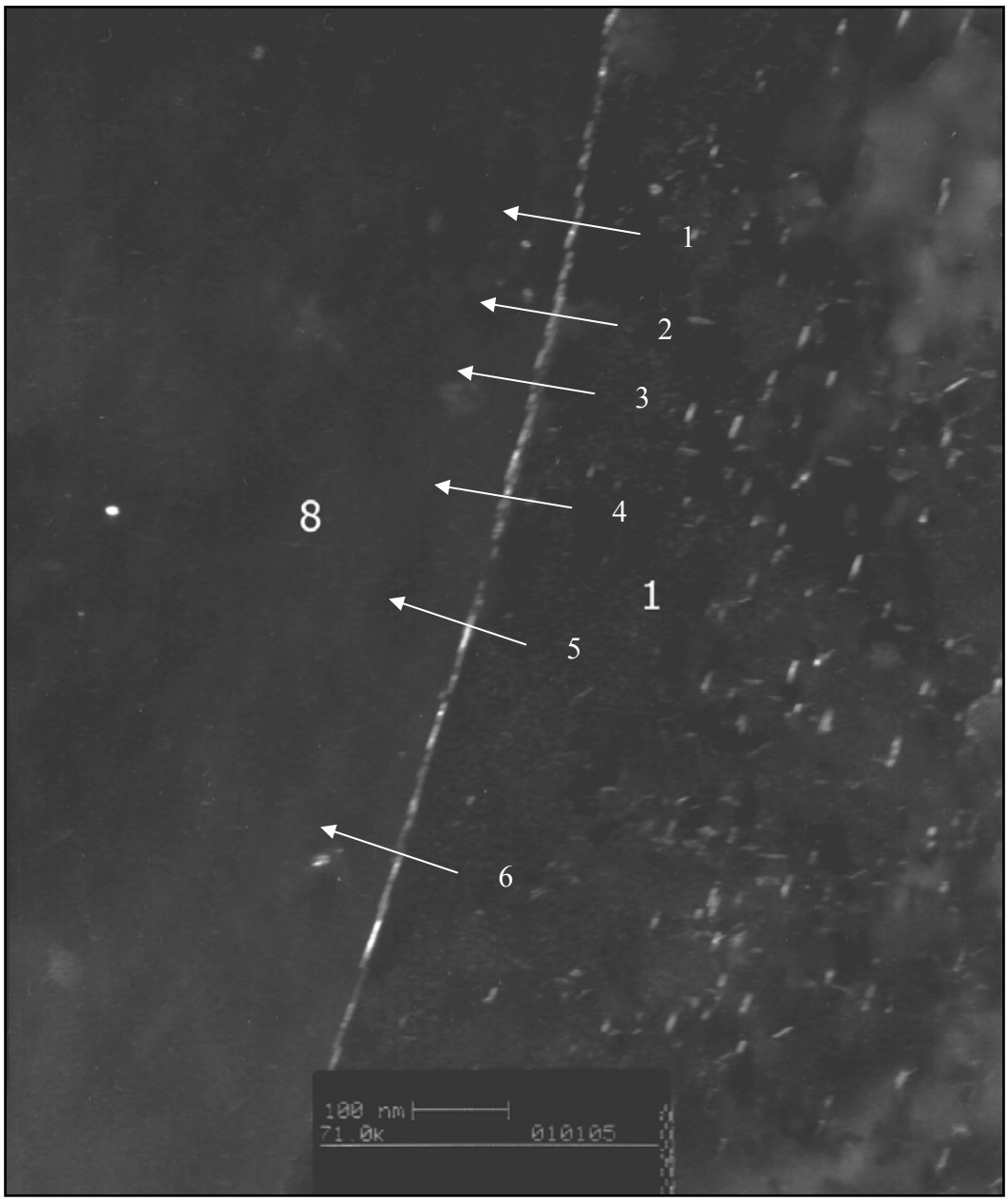

Figure 4.20. TEM Study: AA2096 UA4 Temper. Area 2. EDX Line Scans.

The markers show the approximate location, length and direction of the EDX line scans taken across the boundary between grains 1 and 8. The lines are numbered to correspond with the line scan results illustrated in Figures 17a to 19b.

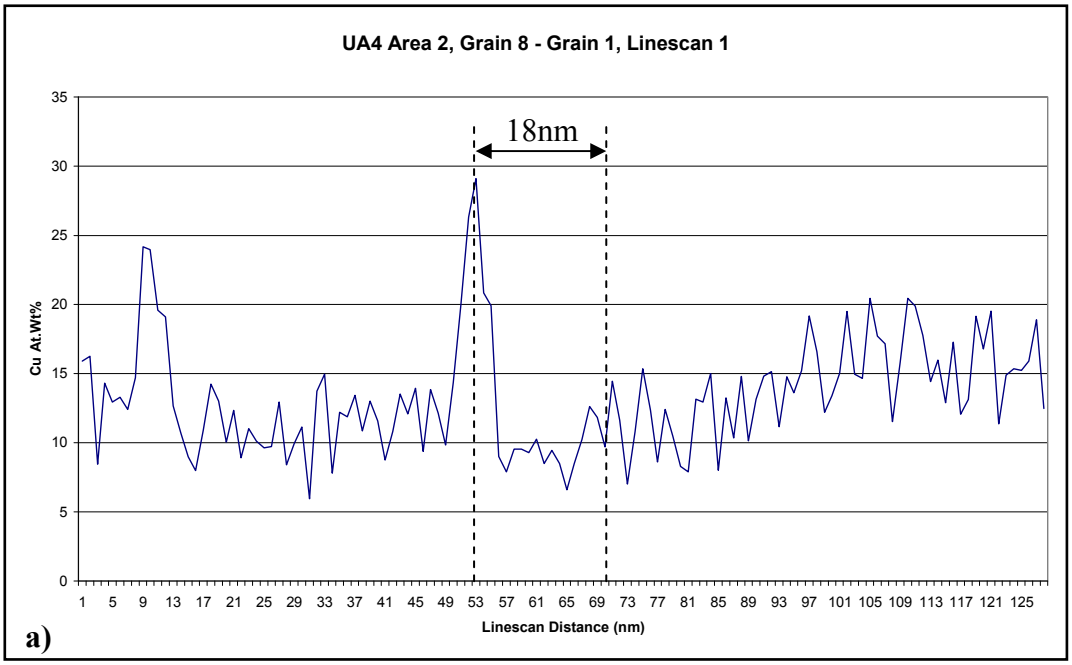

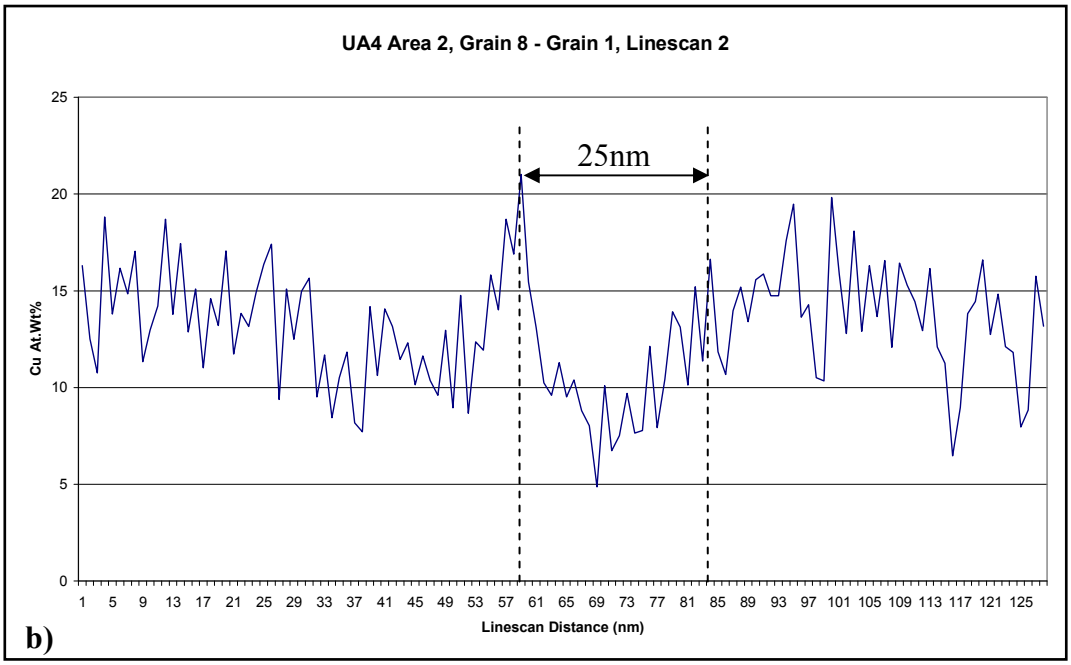

Figure 4.21. TEM Study: AA2096 UA4 Temper. Area 2. EDX Line scans across a low-angle grain boundary.
Energy dispersive X-ray (EDX) line scan analysis across the boundary of grain 1 and grain 8: a) Line scan 1. b) Line scan 2. Refer to Figure 4.20. Approximate width of Cu depleted zones is indicated.

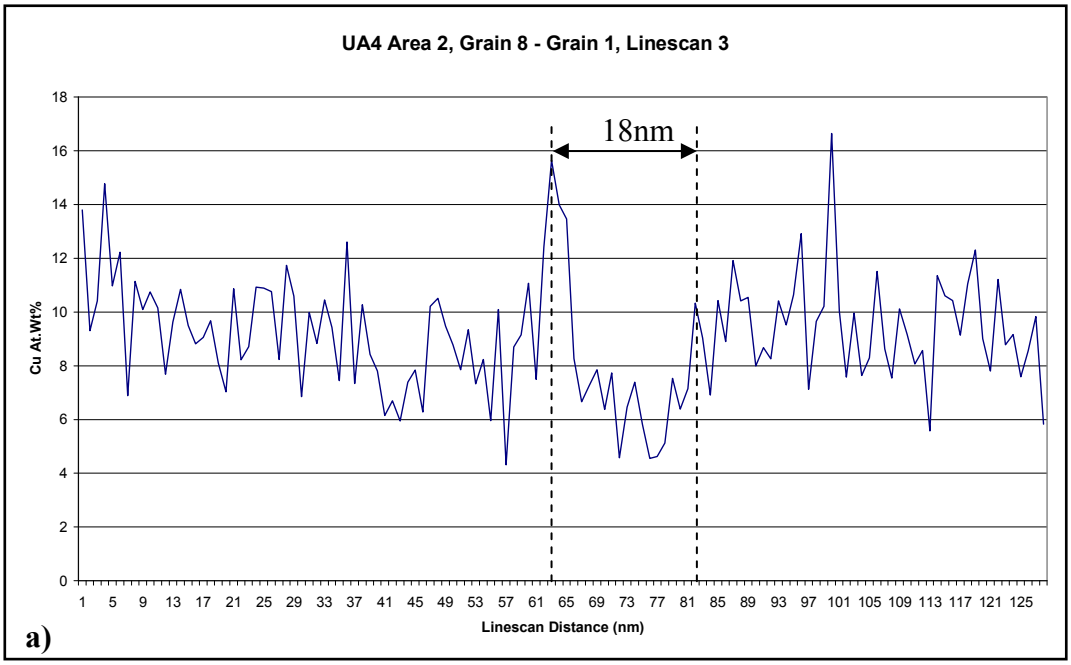

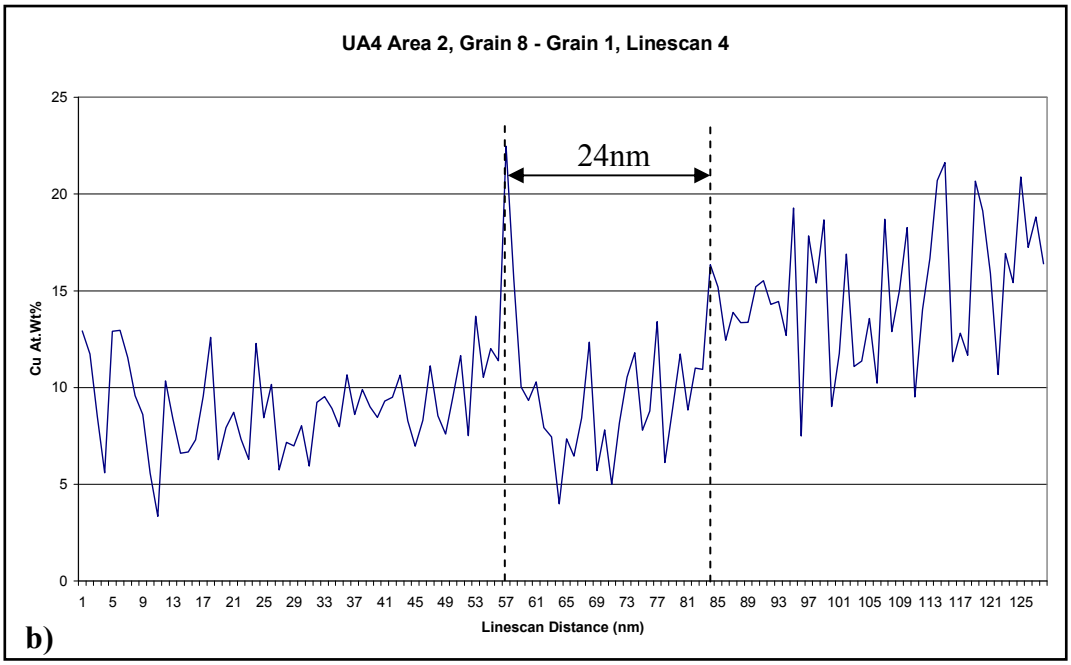

Figure 4.22. TEM Study: AA2096 UA4 Temper. Area 2. EDX Line scans across a low-angle grain boundary.
Energy dispersive X-ray (EDX) line scan analysis across the boundary of grain 1 and grain 8: a) Line scan 3. b) Line scan 4. Refer to Figure 4.20. Approximate width of Cu depleted zones is indicated.

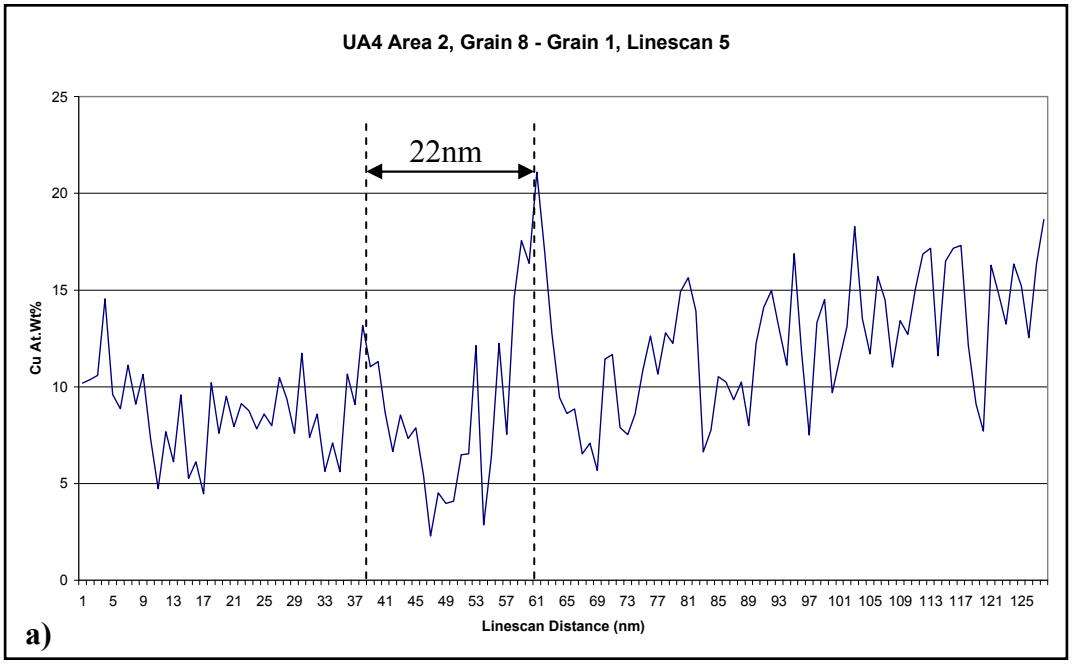

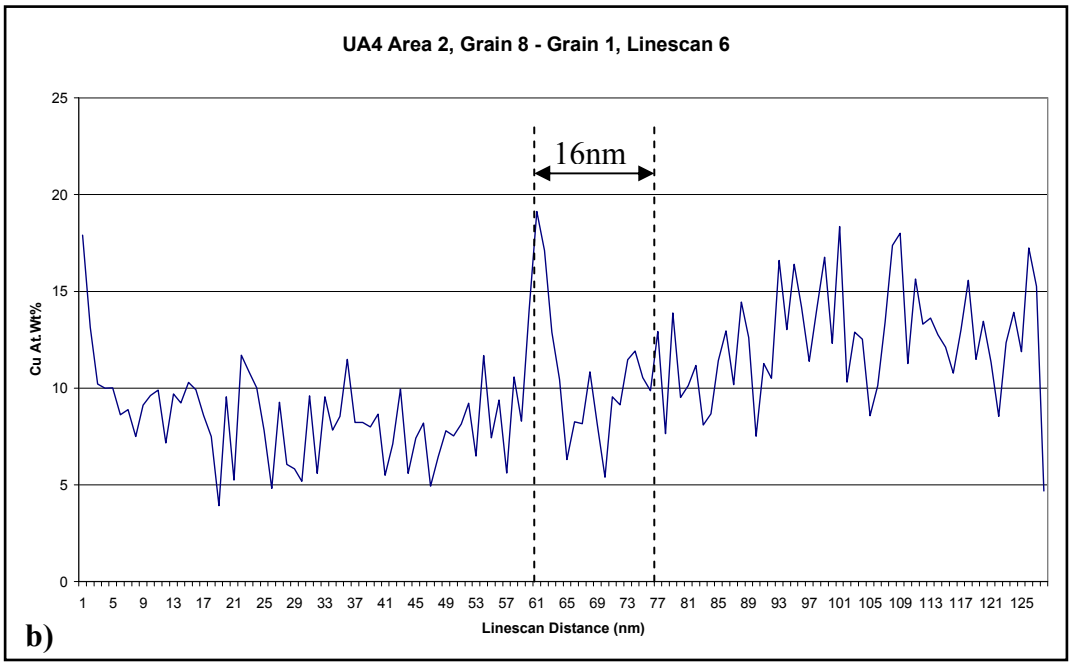

Figure 4.23. TEM Study: AA2096 UA4 Temper. Area 2. EDX Line scans across a low-angle grain boundary.
Energy dispersive X-ray (EDX) line scan analysis across the boundary of grain 1 and grain 8: a) Line scan 5. b) Line scan 6. Refer to Figure 4.20. Approximate width of Cu depleted zone is indicated.

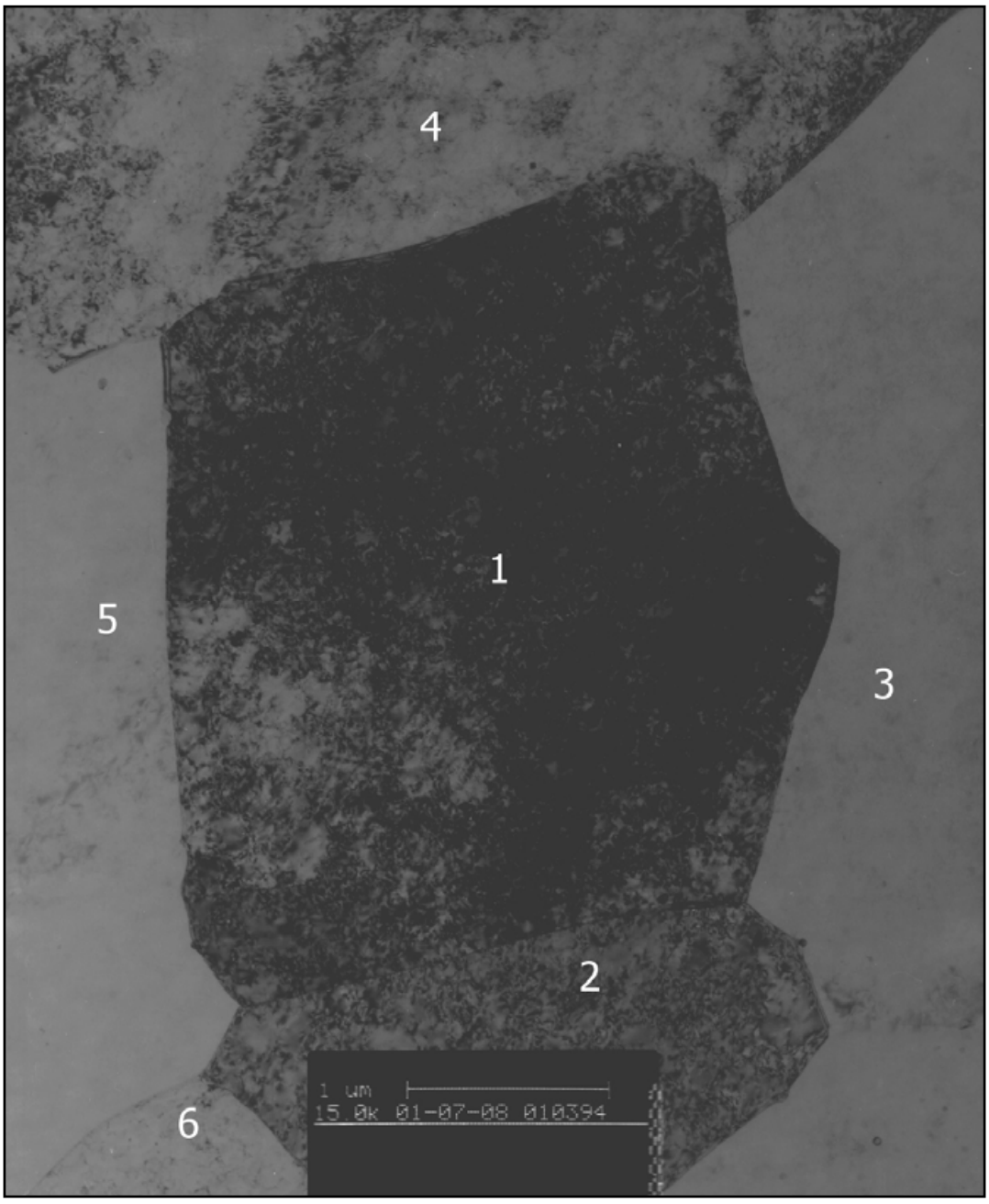

Figure 4.24. TEM Study: AA2096 UA4 Temper. Area 3. Bright Field Grain Map.

Grain 1 was taken as the reference grain and tilted to a [112] zone axis. From this grain, convergent beam electron diffraction (CBED) was used to measure the degree of misorientation of the adjacent grains of interest from the reference. Dark field images were used to highlight T_1 precipitation within the reference grain.

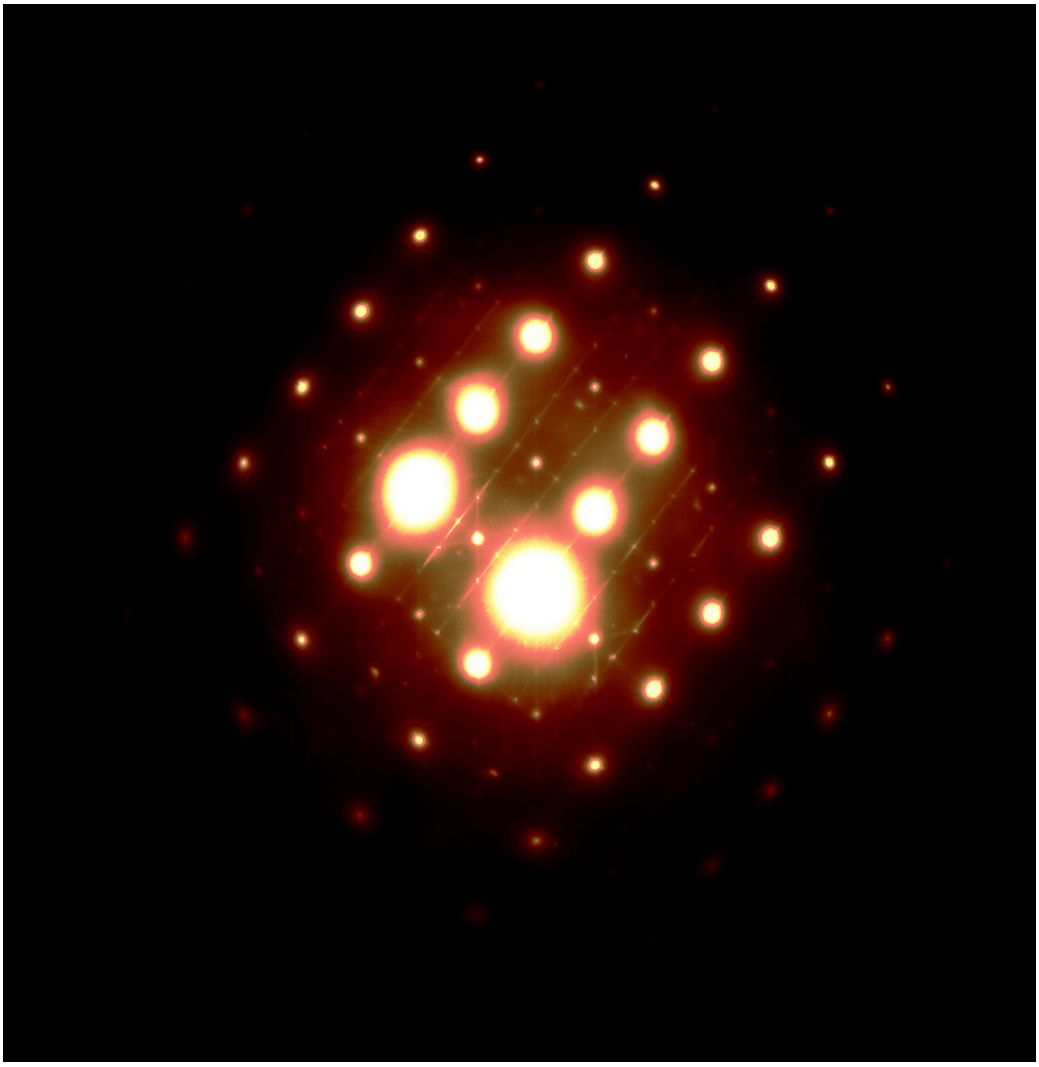

Figure 4.25. TEM Study: AA2096 UA4 Temper. Area 3. Diffraction Pattern.

Selected area diffraction pattern of a [112] zone axis. Bright spots and streaks associated with the β', δ' and T_1 phases are clearly visible. Faint streaks associated with S' phase can also be seen.

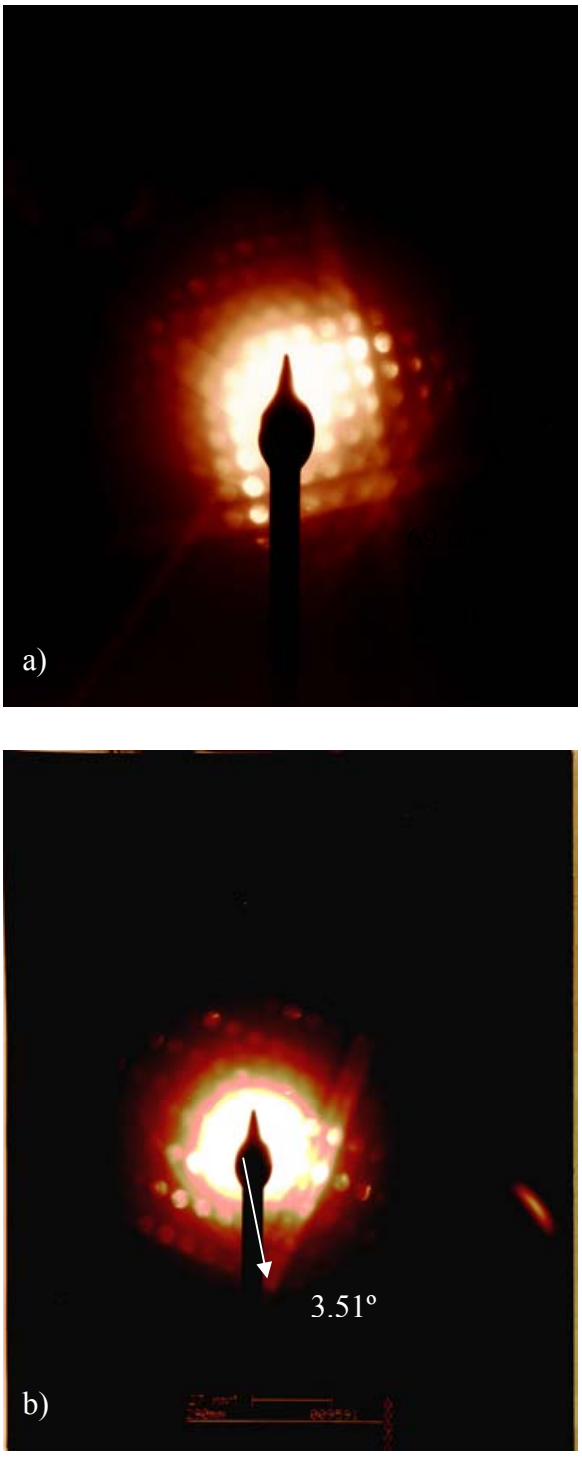

Figure 4.26. TEM Study: AA2096 UA4 Temper. Area 3. CBED.
Convergent beam electron diffraction (CBED) patterns of the following grains from Figure 2: a) Grain 5, b) Grain 2. The degree of misorientation from the reference grain is illustrated for grain 2 whereas grain 5 lies on [100] zone axis and is therefore designated as a high-angle grain boundary (Type I).

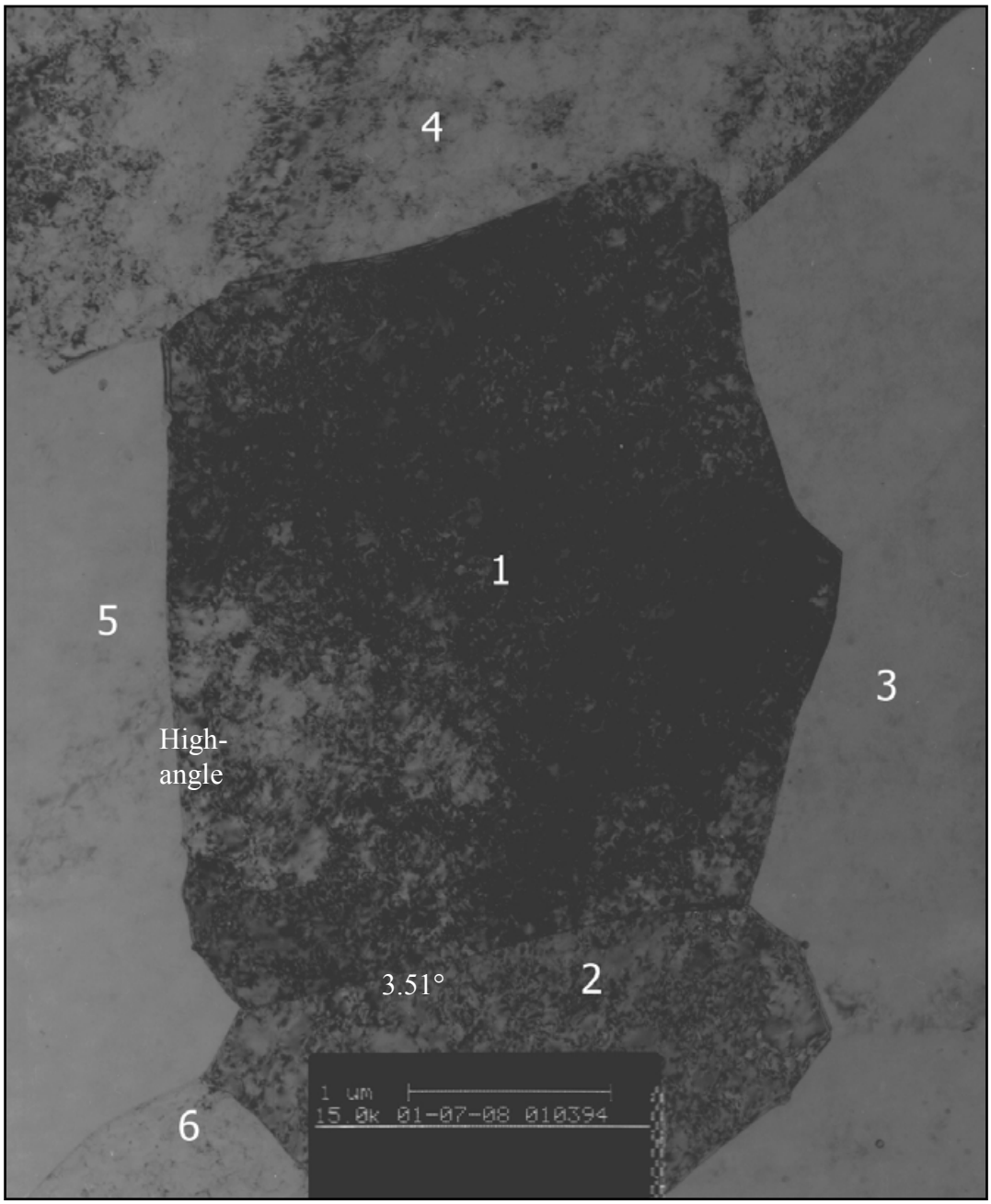

Figure 4.27. TEM Study: AA2096 UA4 Temper. Area 3. Bright Field Grain Map.

Bright field grain map from Figure 24, illustrating angles of misorientation for the grain boundaries of interest (Grains 2 and 5).

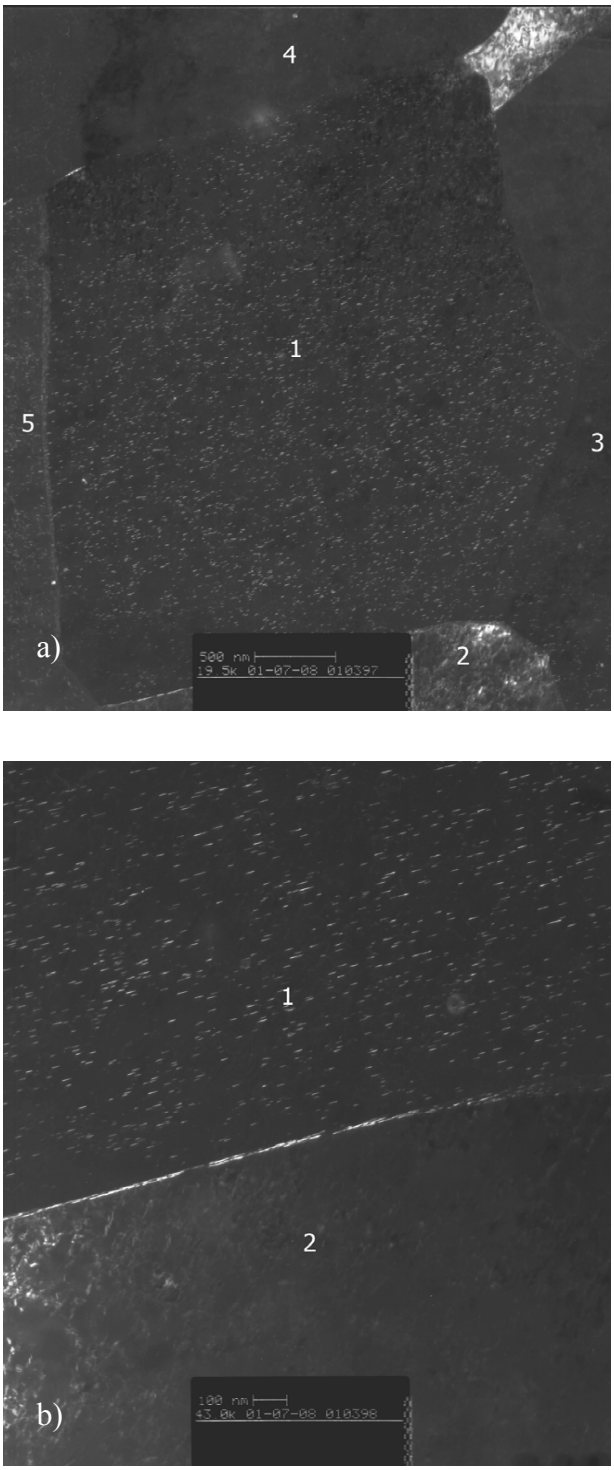

Figure 4.28. TEM Study: AA2096 UA4 Temper. Area 3. Dark Field Images.
a) Dark field image highlighting T_1 within the matrix of grain 1 and along the adjacent boundaries. b) Dark field TEM image highlighting one variant of the T_1 precipitate throughout the matrix of grain 1 and along the boundary between grains 1 and 2. An apparent PFZ is visible, particularly on the Grain 1 side of the boundary.
Note: Line scans were taken at various points along the boundaries of grains 2 (low-angle) and 5 (High-angle).

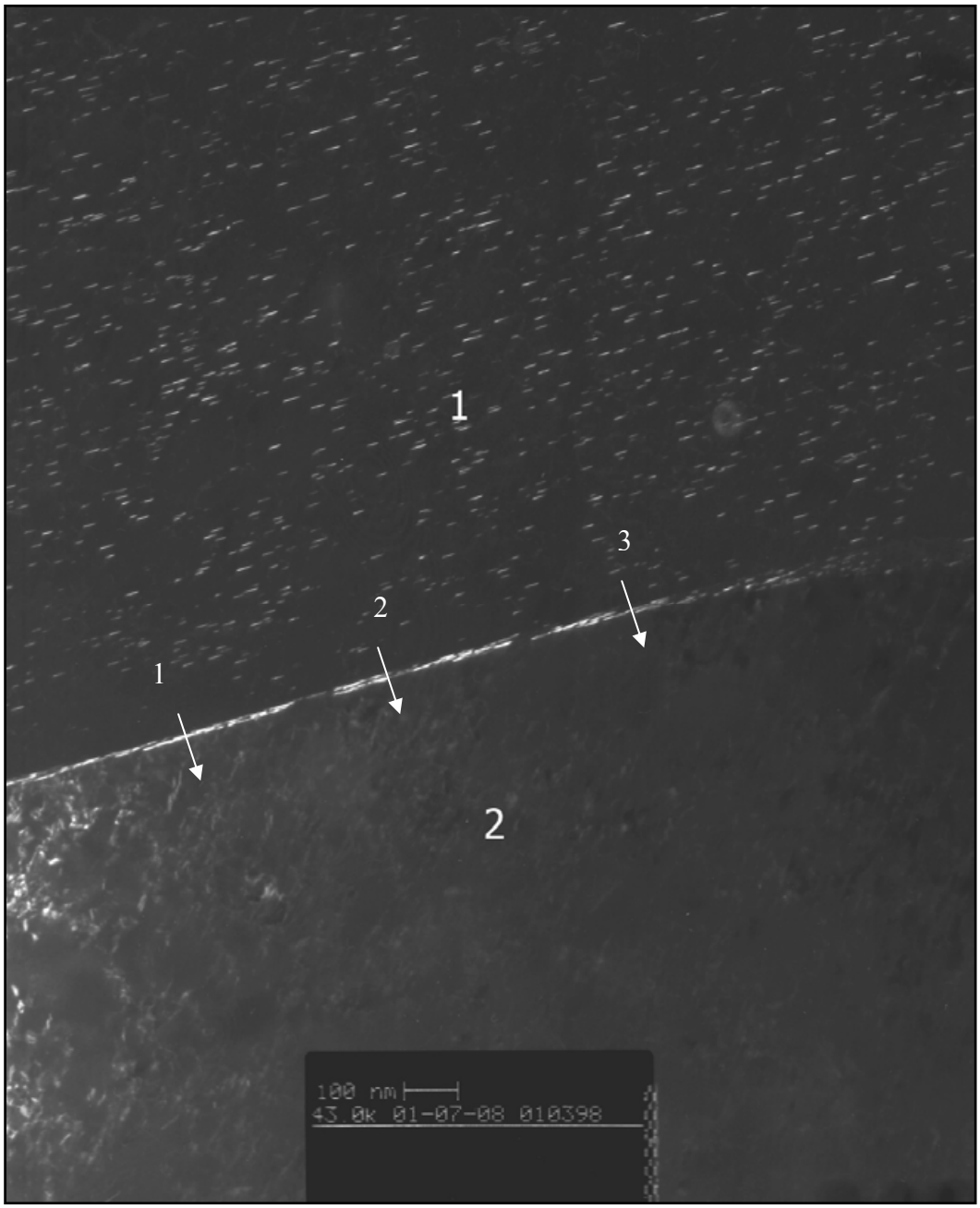

Figure 4.29. TEM Study: AA2096 UA4 Temper. Area 3. EDX Line Scans.

The markers show the approximate location, length and direction of the EDX line scans taken across the boundary between grains 1 and 2. The lines are numbered to correspond with the line scan results illustrated in Figures 4.30 – 4.31.

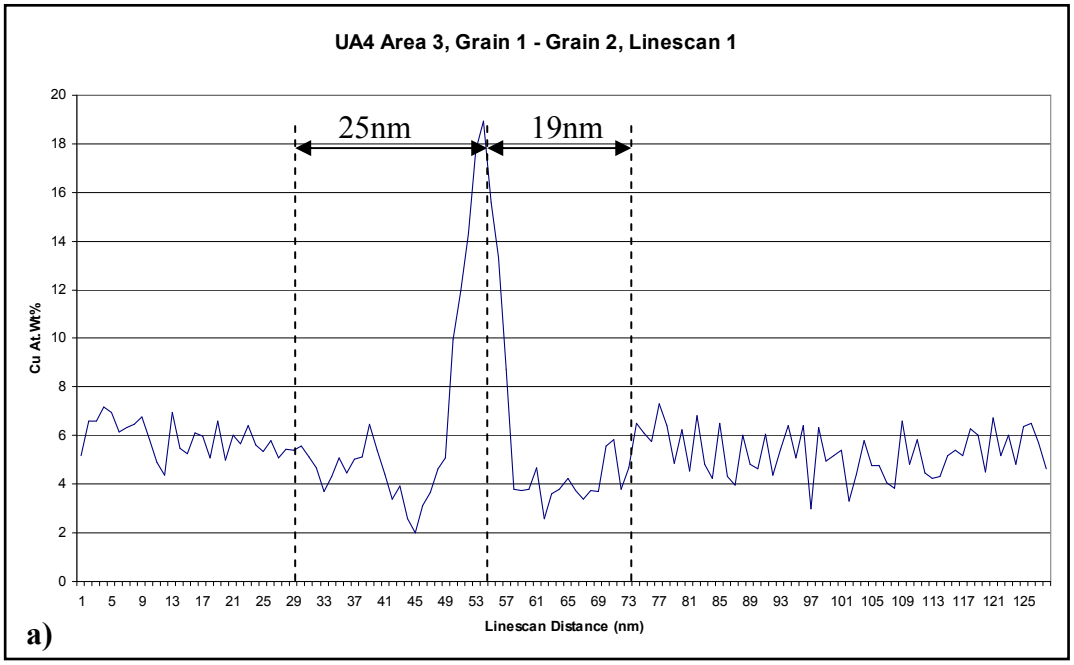

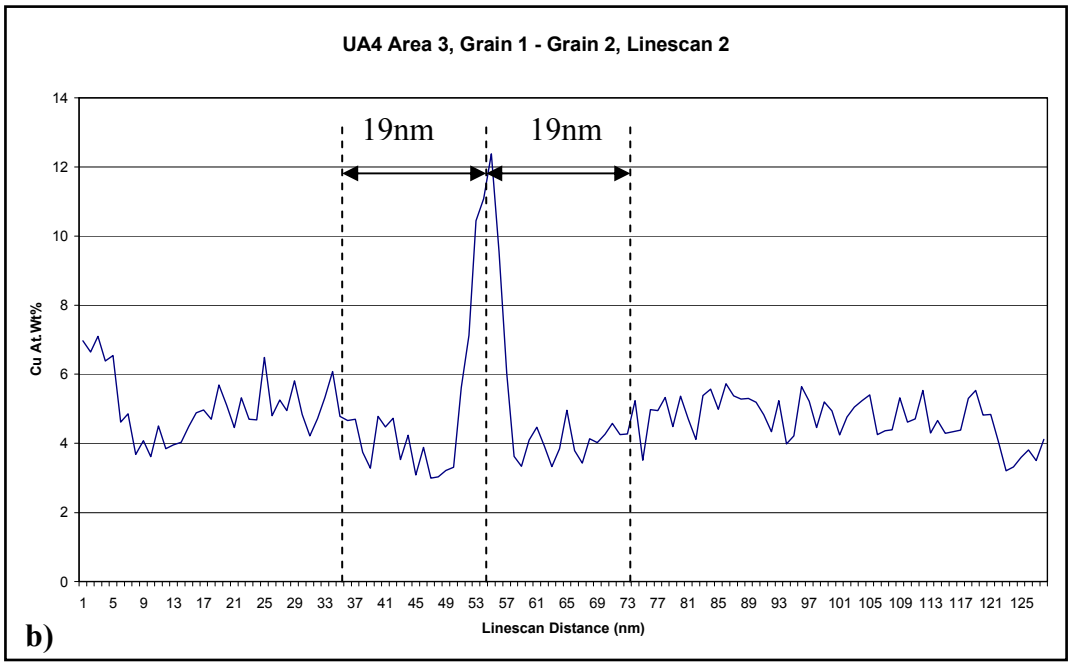

Figure 4.30. TEM Study: AA2096 UA4 Temper. Area 3. EDX Line scans across a low-angle grain boundary (3.51º).
Energy dispersive X-ray (EDX) line scan analysis across the boundary of grain 1 and grain 2: a) Line scan 1. b) Line scan 2. Refer to Figure 4.29. Approximate width of Cu depleted zone is indicated

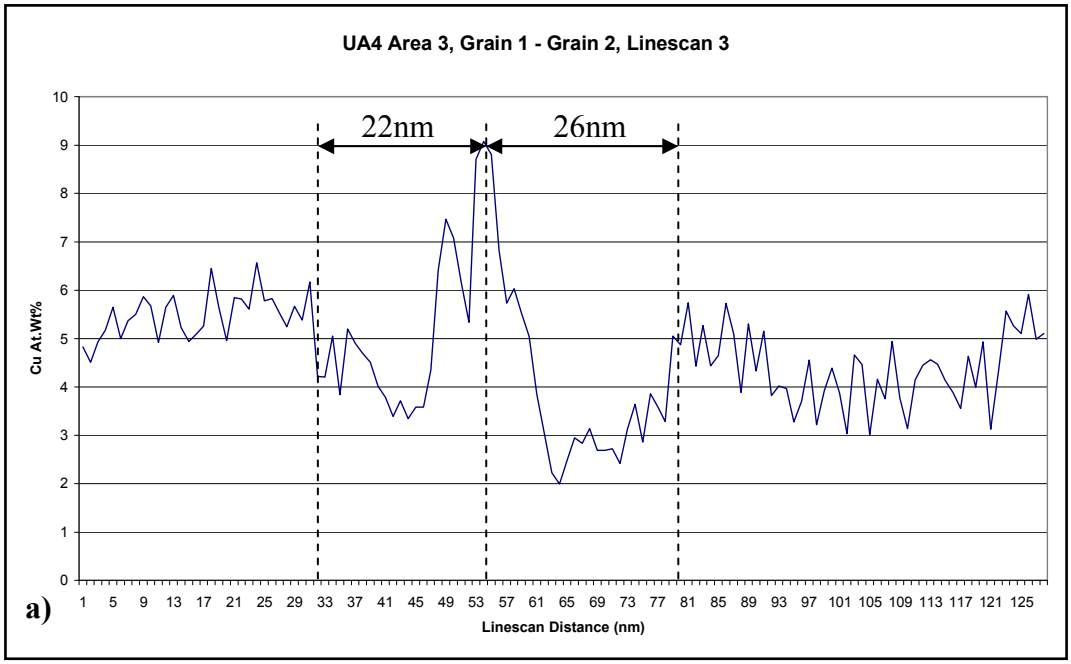

Figure 4.31. TEM Study: AA2096 UA4 Temper. Area 3. EDX Line Scan across a low angle grain boundary (3.51º).

Energy dispersive X-ray (EDX) line scan analysis across the boundary between grain 1 and grain 2 (low-angle), line scan 3. Refer to Figure 4.29. Approximate width of Cu depleted zone is indicated.

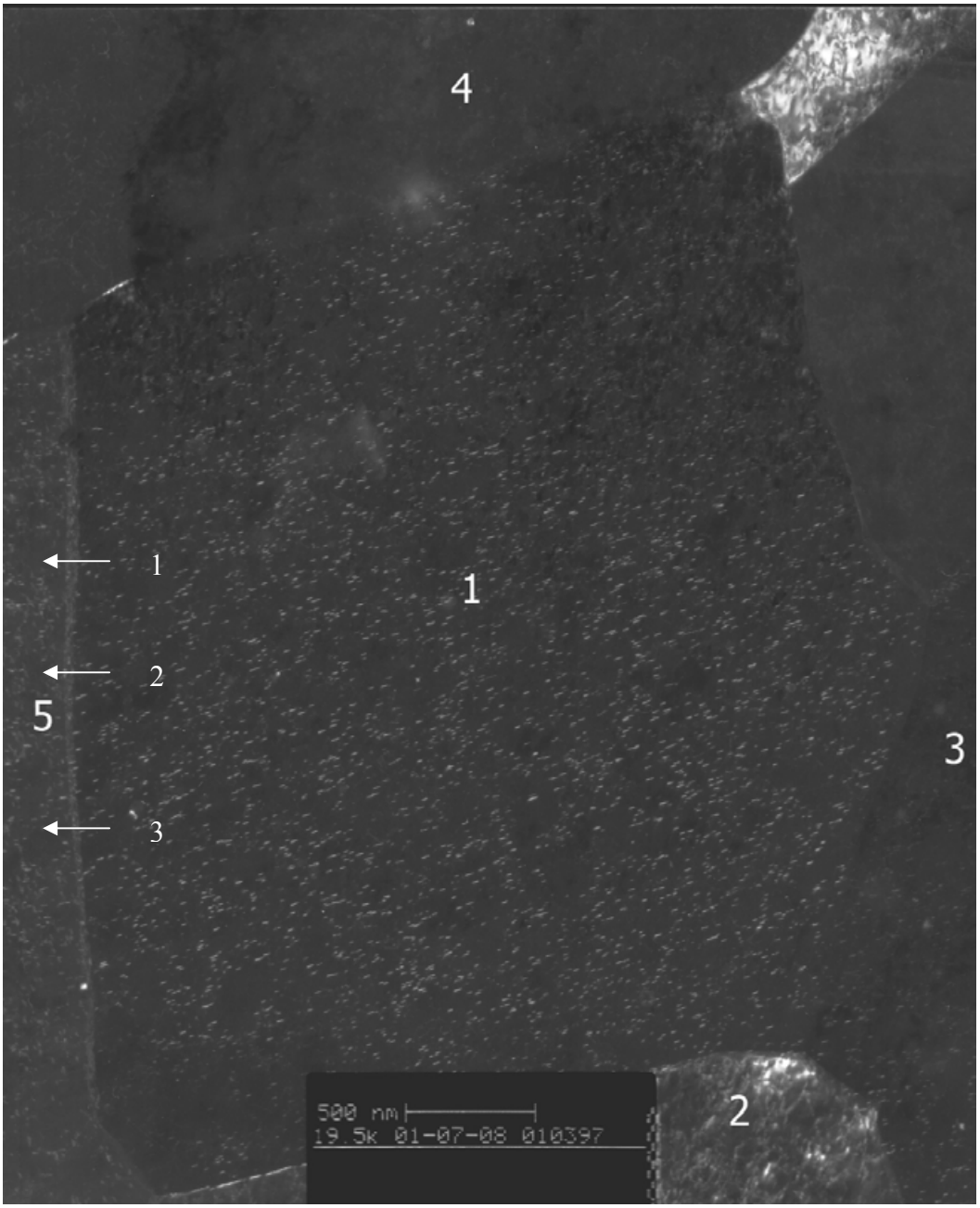

Figure 4.32. TEM Study: AA2096 UA4 Temper. Area 3. EDX Line Scans.

The markers show the approximate location, length and direction of the EDX line scans taken across the boundary between grains 1 and 5. The lines are numbered to correspond with the line scan results illustrated in Figures 4.33 - 4.34.

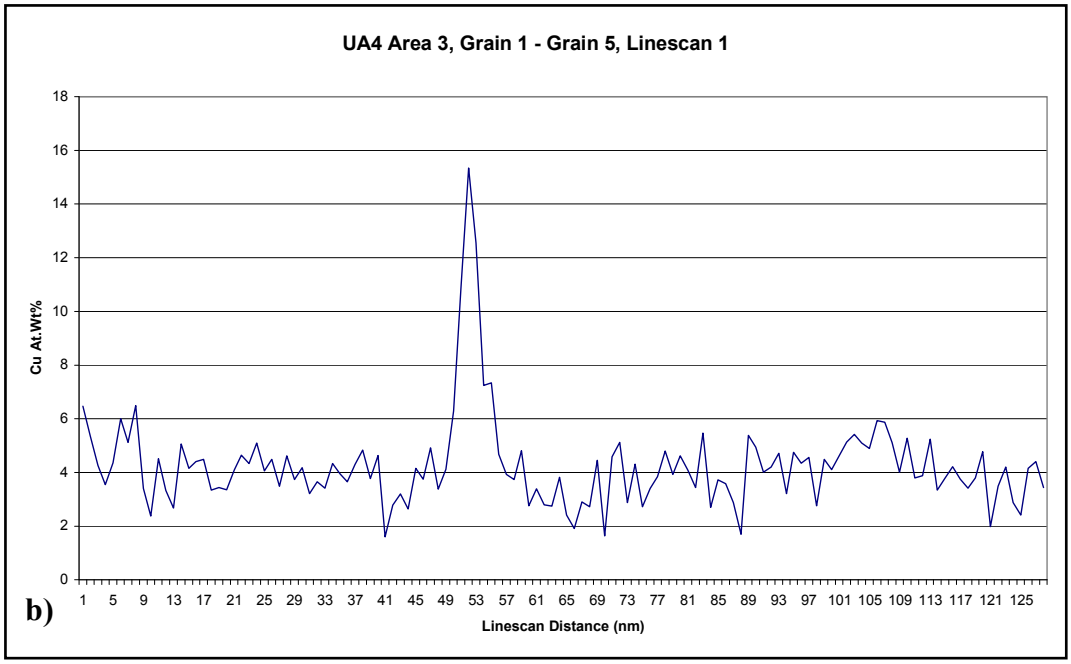

Figure 4.33. TEM Study: AA2096 UA4 Temper. Area 3. EDX Line Scan across a high angle grain boundary (69.07º).

Energy dispersive X-ray (EDX) line scan analysis across the boundary between grain 1 and grain 5 (high-angle), line scan 1. Refer to Figure 4.32.

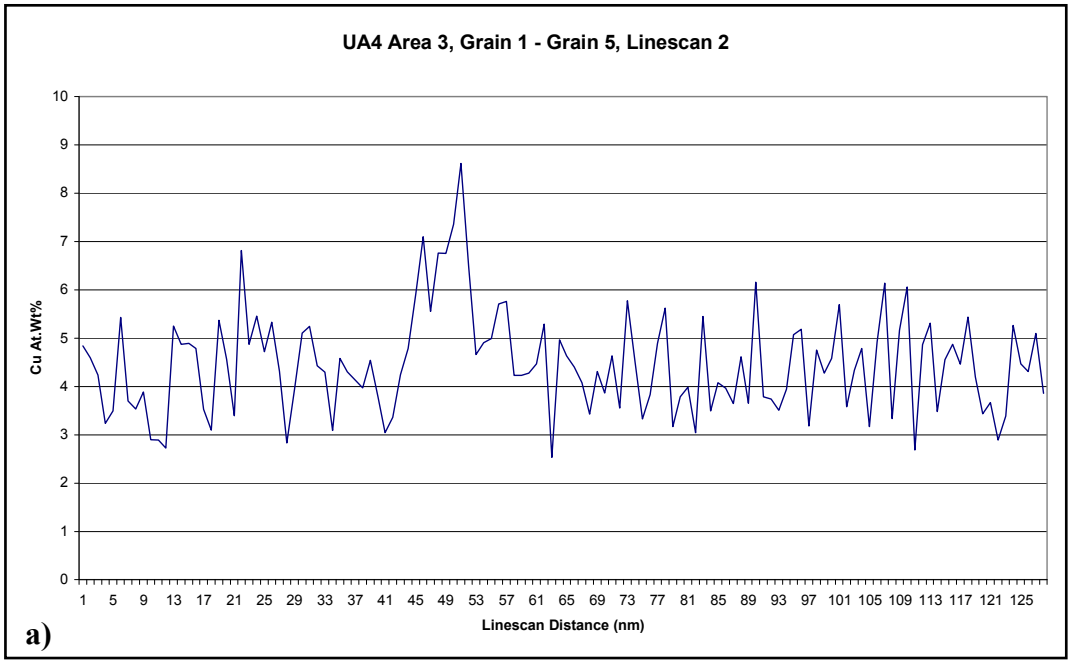

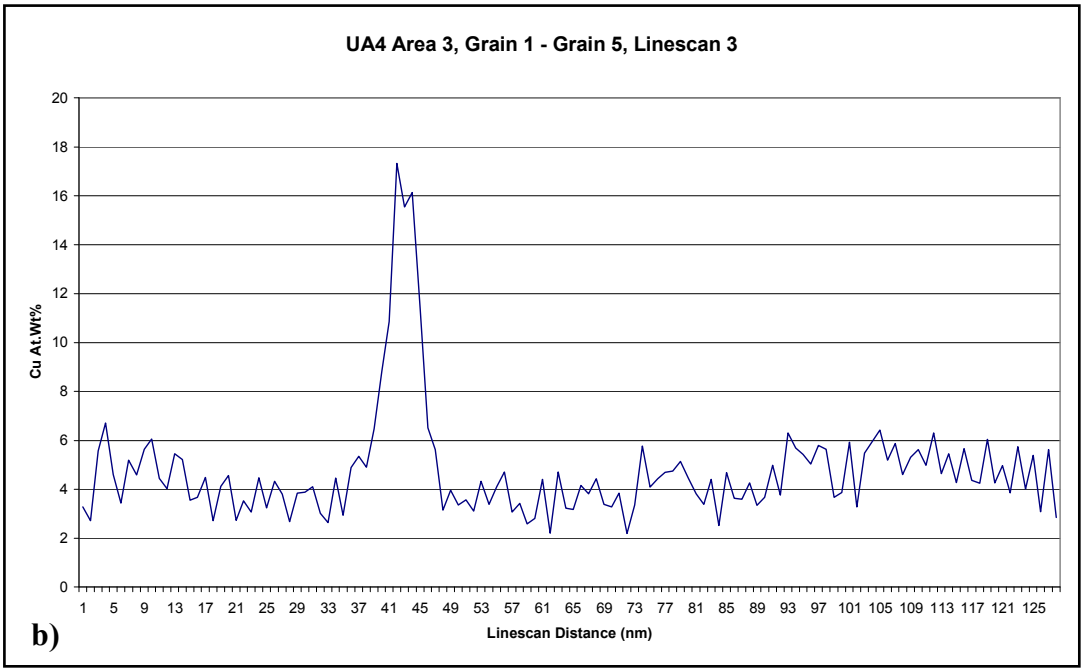

Figure 4.34. TEM Study: AA2096 UA4 Temper. Area 3. EDX Line scans across a high-angle grain boundary (69.07º).
Energy dispersive X-ray (EDX) line scan analysis across the boundary of grain 1 and grain 5: a) Line scan 2. b) Line scan 3. Refer to Figure 4.32.

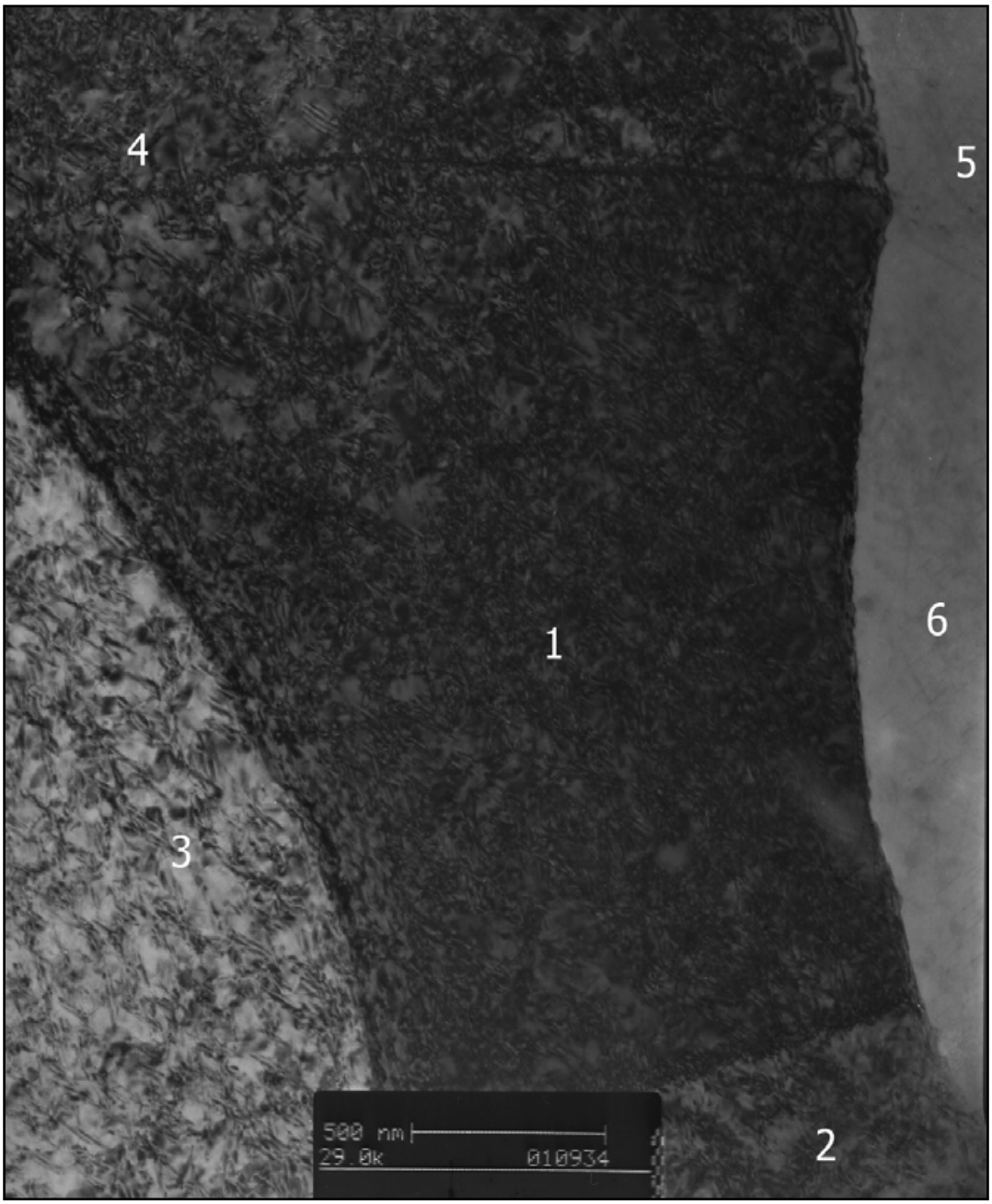

Figure 4.35. TEM Study: AA2096 UA12 Temper. Bright Field Grain Map.
Grain 1 was taken as the reference grain and tilted to a [112] zone axis. From this grain, convergent beam electron diffraction (CBED) was used to measure the degree of misorientation of the adjacent grains of interest from the reference. Dark field images were used to highlight T_1 precipitation within the reference grain.

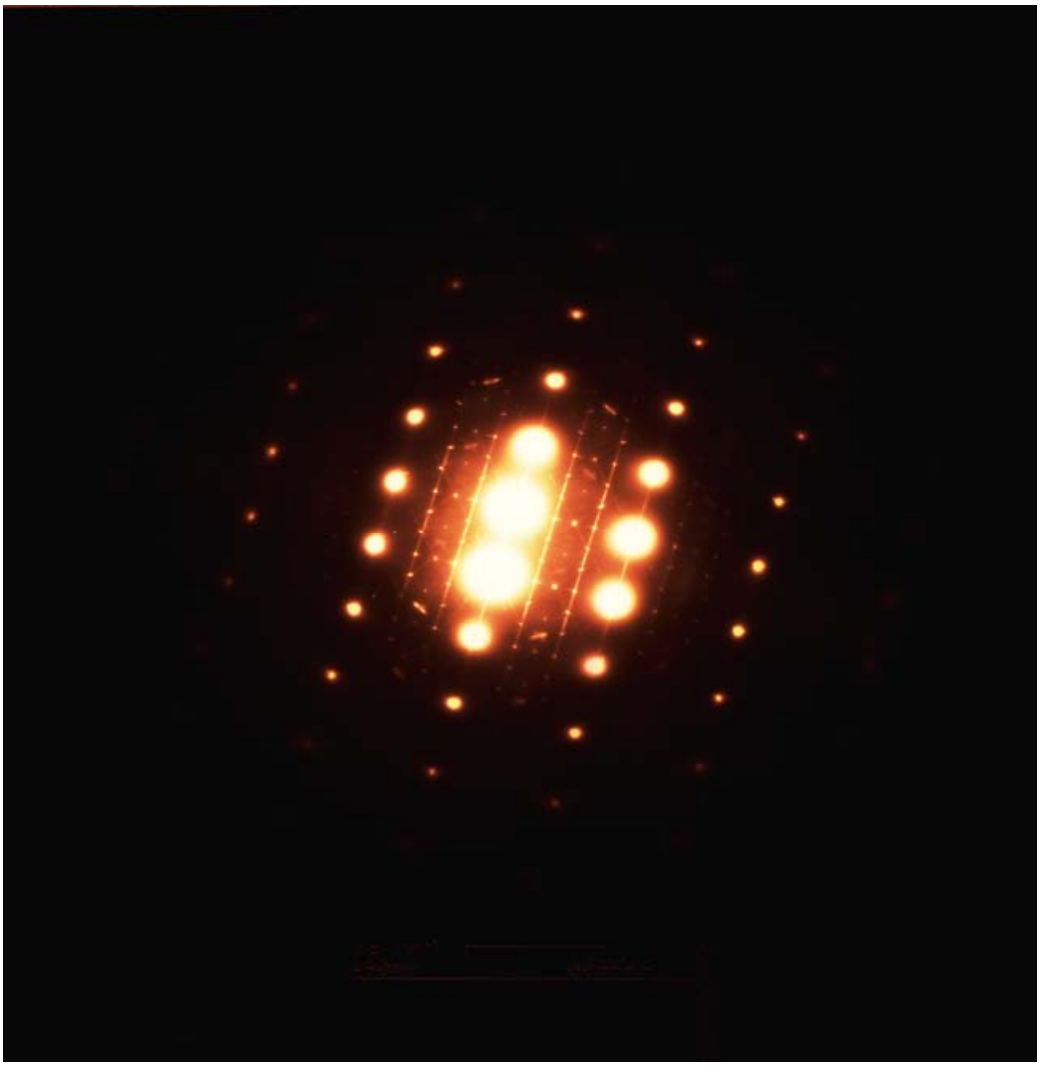

Figure 4.36. TEM Study: AA2096 UA12 Temper. Diffraction Pattern.
Selected area diffraction pattern of a [112] zone axis. Bright spots and streaks associated with the β', δ', T_1, S' and Ω phases are clearly visible. Faint streaks associated with the θ' phase can also be seen.

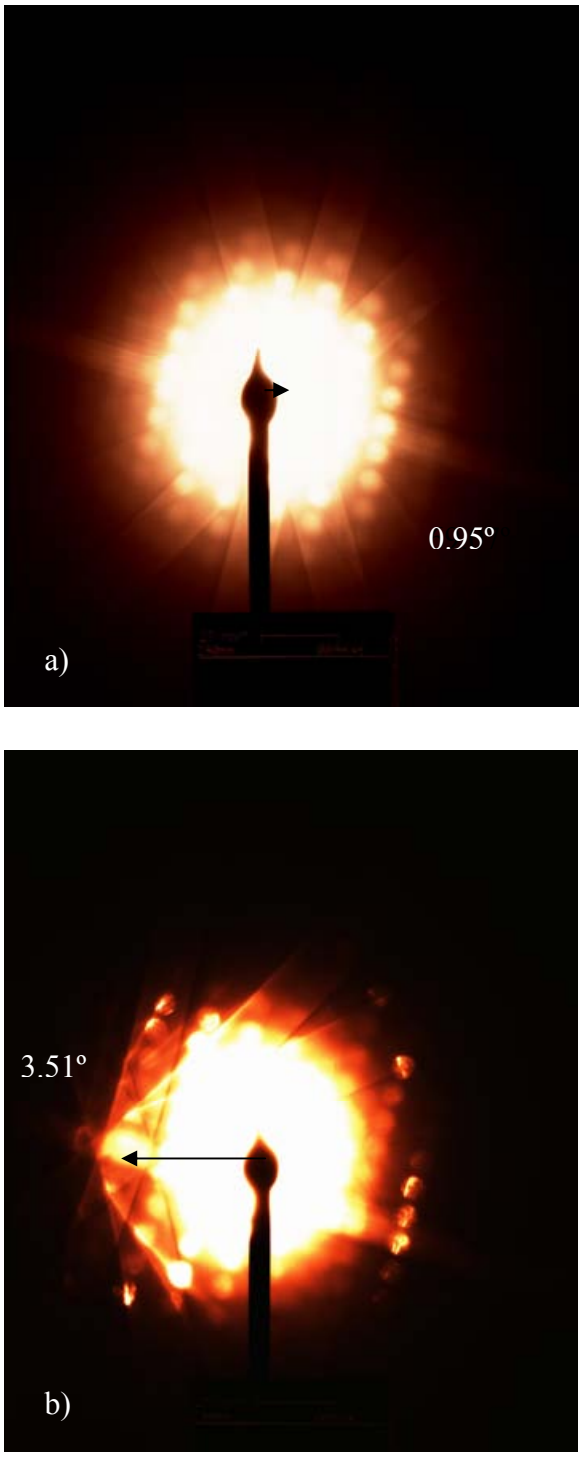

Figure 4.37. TEM Study: AA2096 UA12 Temper. CBED.
Convergent beam electron diffraction (CBED) patterns of the following grains from Figure 35: a) Grain 2, b) Grain 3. The degree of misorientation from the reference grain is illustrated for each CBED pattern.

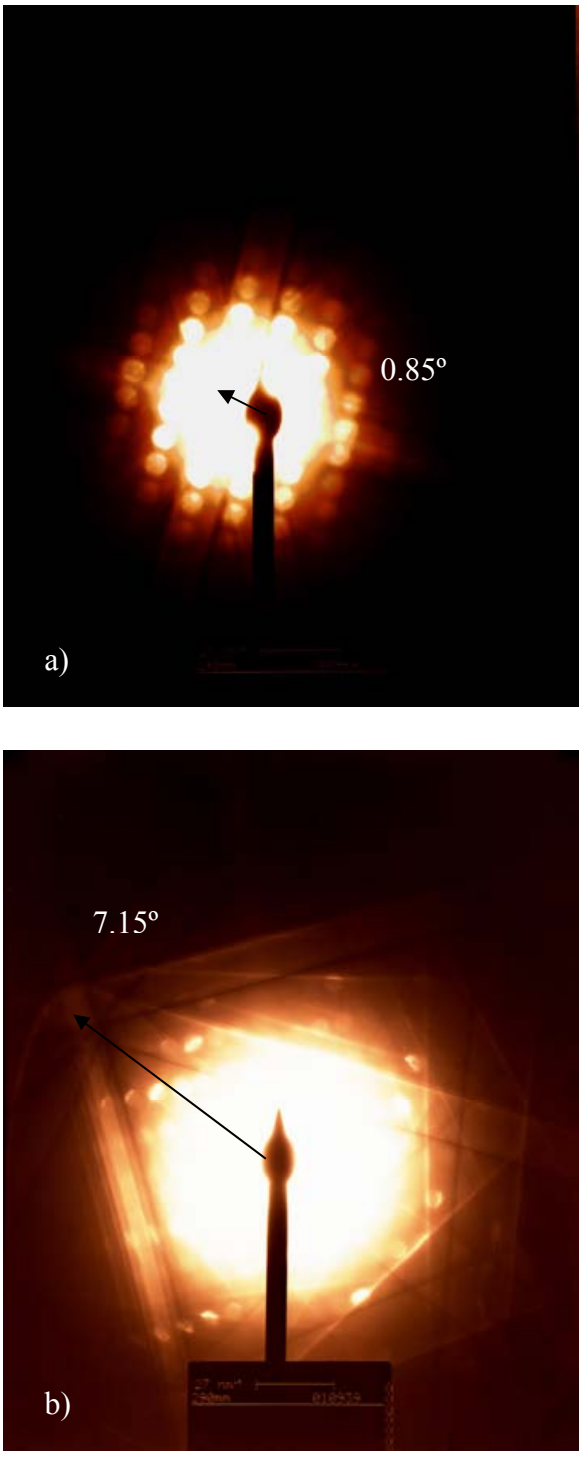

Figure 4.38. TEM Study: AA2096 UA12 Temper. CBED.
Convergent beam electron diffraction (CBED) patterns of the following grains from Figure 35: a) Grain 4, b) Grain 6. The degree of misorientation from the reference grain is illustrated for each CBED pattern.

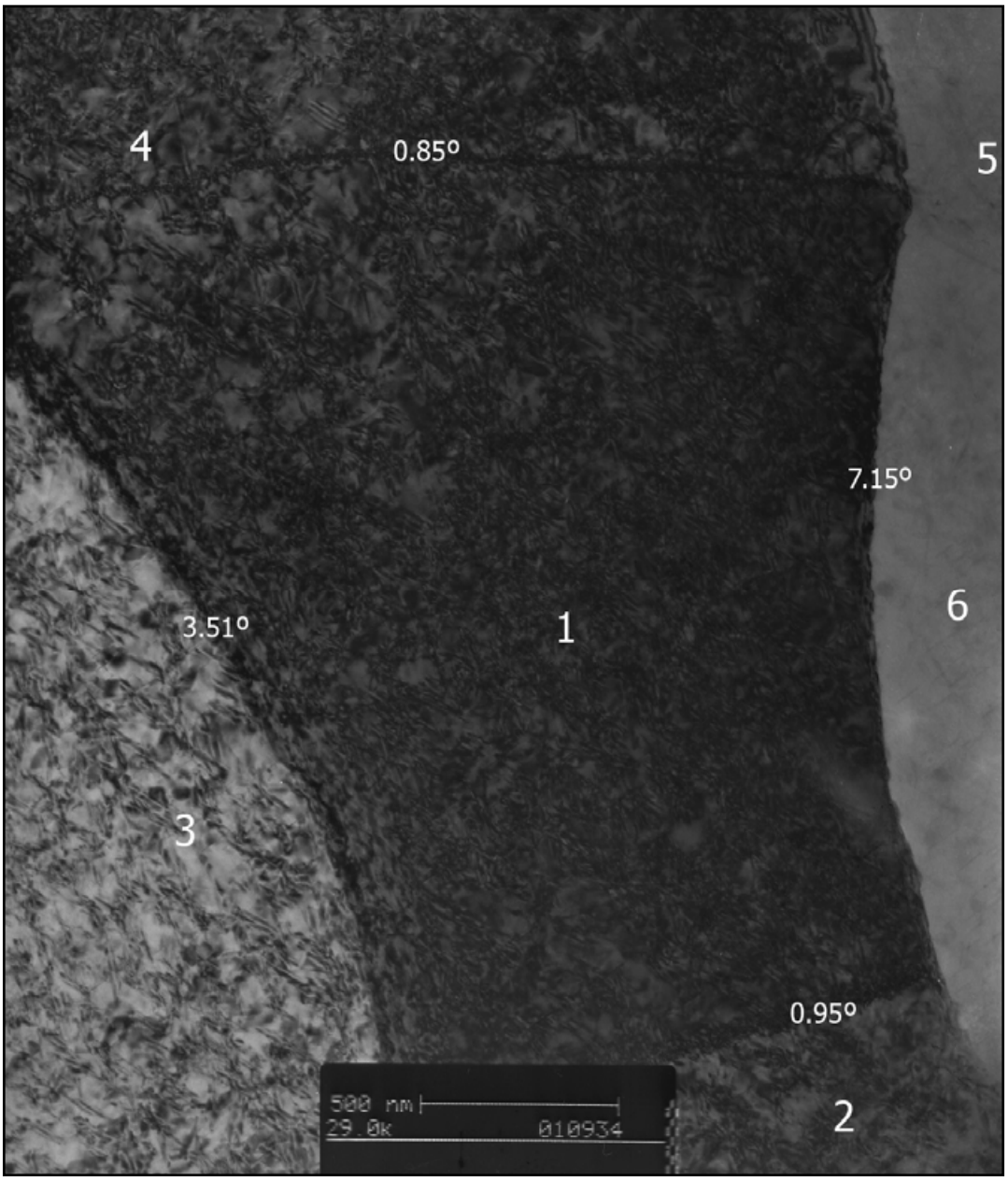

Figure 4.39. TEM Study: AA2096 UA12 Temper. Bright Field Grain Map.

Bright field grain map from Figure 35, illustrating angles of misorientation for the grain boundaries of interest.

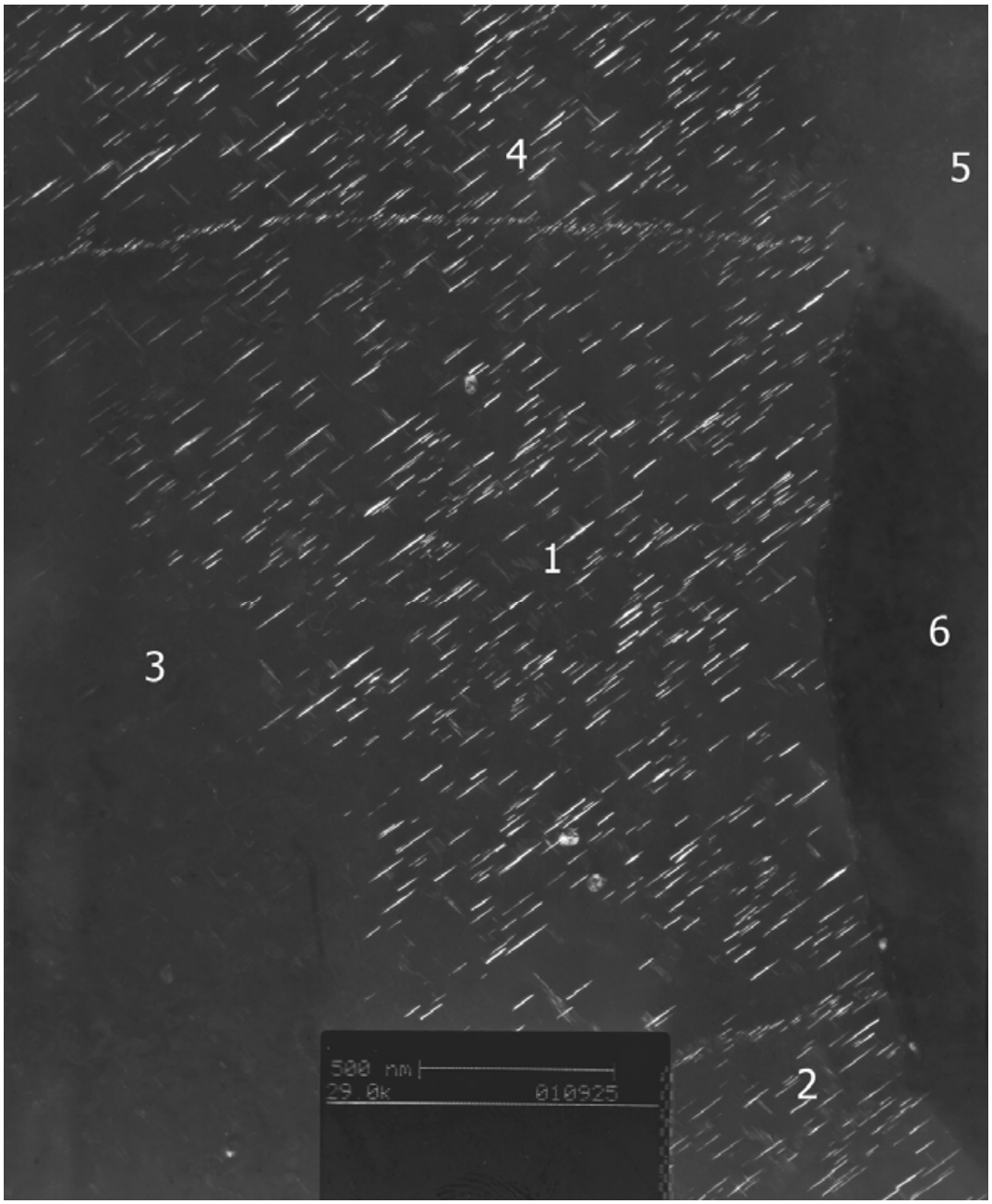

Figure 4.40. TEM Study: AA2096 UA12 Temper. Dark Field Image of Grain Map.

Corresponding dark field image to Figure 39, highlighting T_1 within the matrix of grain 1 and along adjacent grain boundaries.

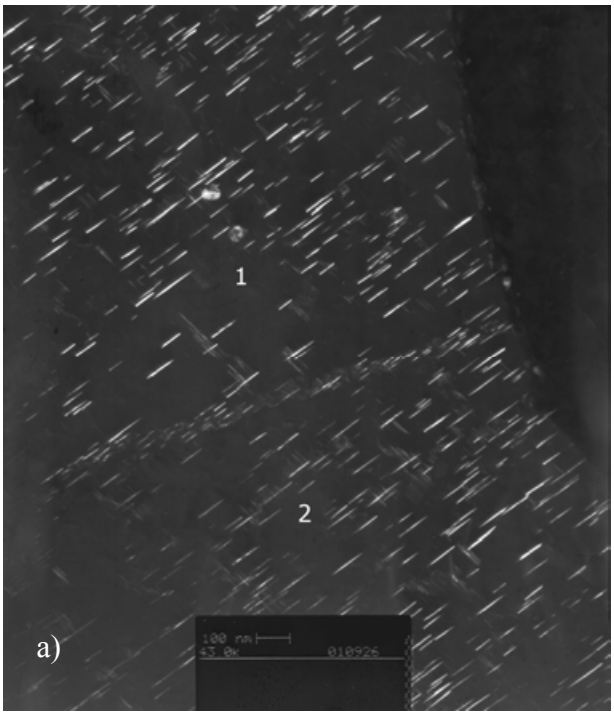

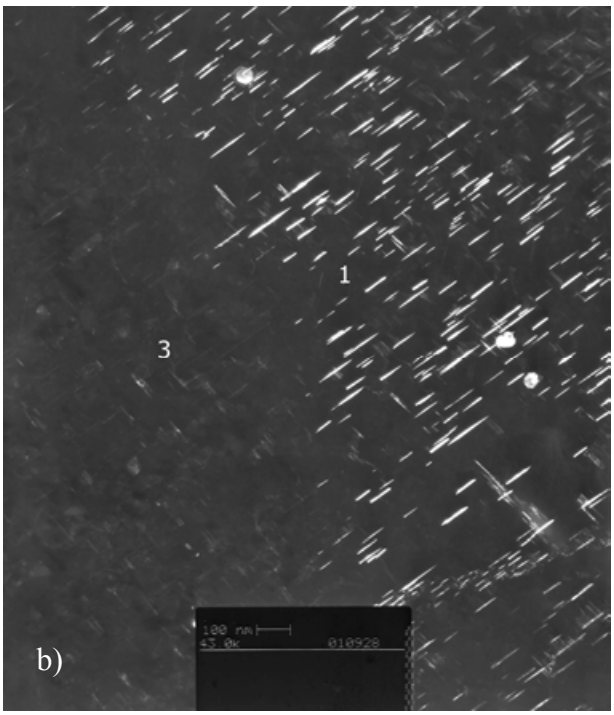

Figure 4.41. TEM Study: AA2096 UA12 Temper. Dark Field Images.
a) Dark field TEM image highlighting one variant of the T_1 precipitate throughout the matrix and along the boundary between grains 1 and 2. b) Dark field TEM image highlighting one variant of the T_1 precipitate throughout the matrix and along the boundary of grains 1and 3.

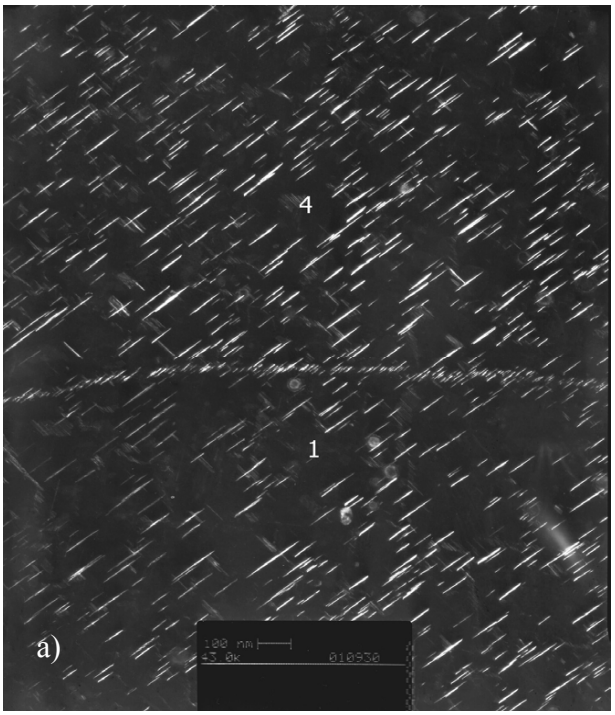

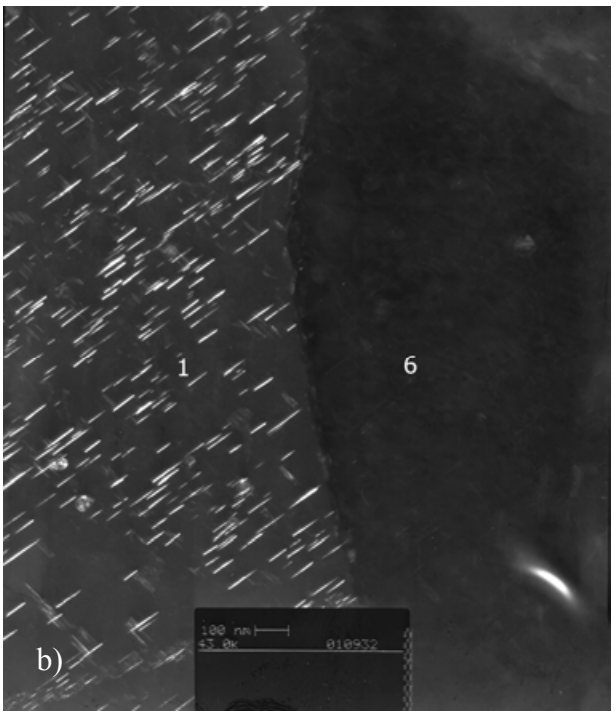

Figure 4.42. TEM Study: AA2096 UA12 Temper. Dark Field Images.
a) Dark field TEM image highlighting one variant of the T_1 precipitate throughout the matrix and along the boundary between grains 1 and 4. b) Dark field TEM image highlighting one variant of the T_1 precipitate throughout the matrix and along the boundary of grains 1and 6.

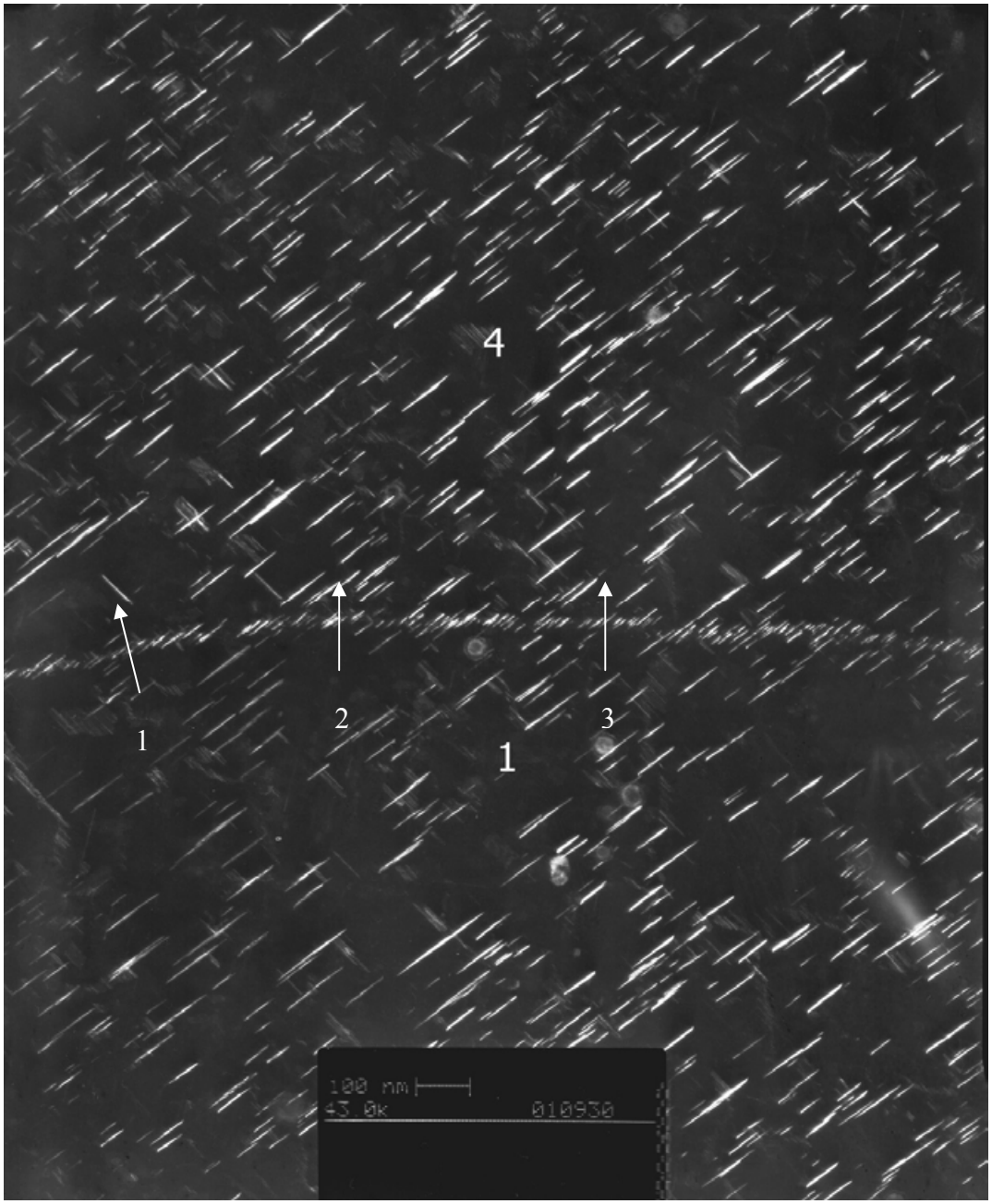

Figure 4.43. TEM Study: AA2096 UA12 Temper. EDX Line Scans.

The markers show the approximate location, length and direction of the EDX line scans taken across the boundary between grains 1 and 4. The lines are numbered to correspond with the line scan results illustrated in Figures 4.44 – 4.45.

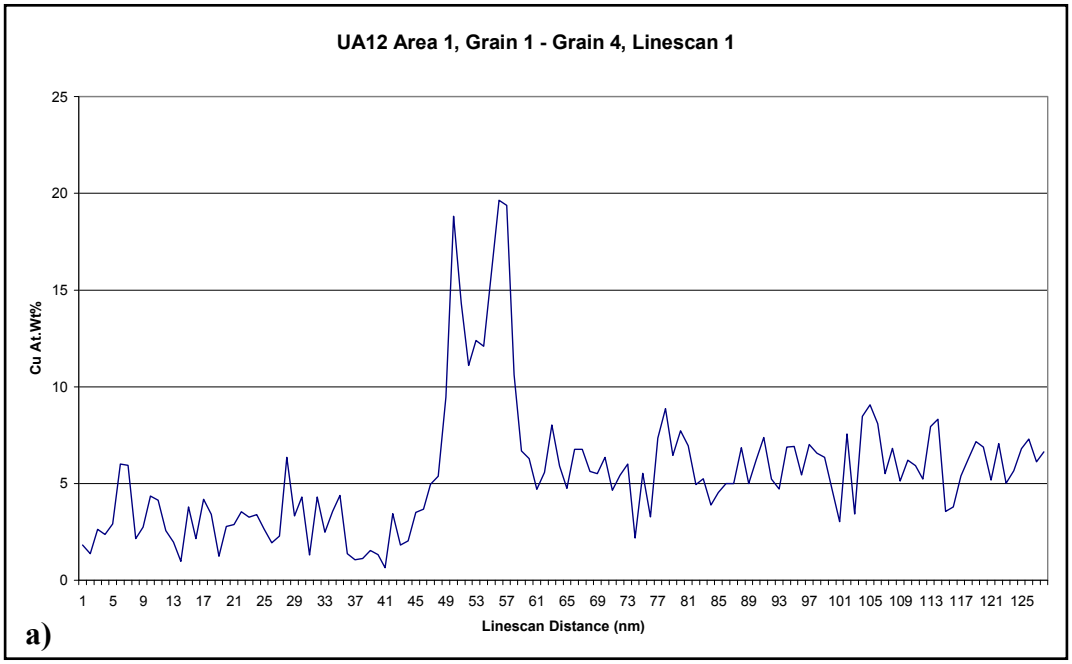

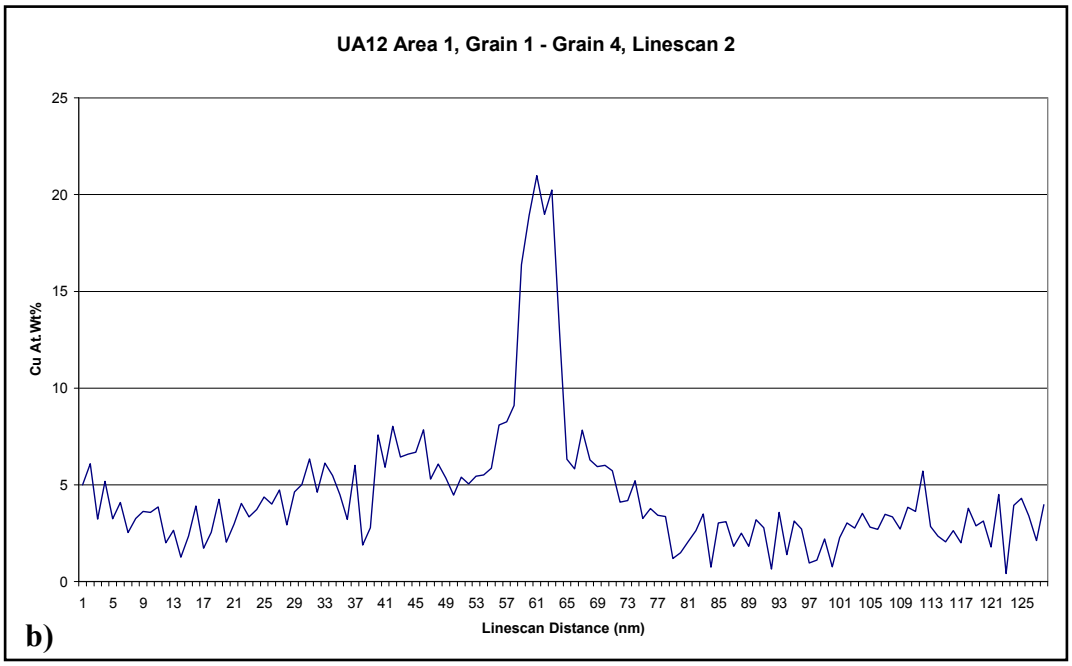

Figure 4.44. TEM Study: AA2096 UA12 Temper. EDX Line scans across a very low-angle grain boundary (0.85º).
Energy dispersive X-ray (EDX) line scan analysis across the boundary between grain 1 and grain 4: a) Line scan 2. b) Line scan 3. Refer to Figure 4.43.

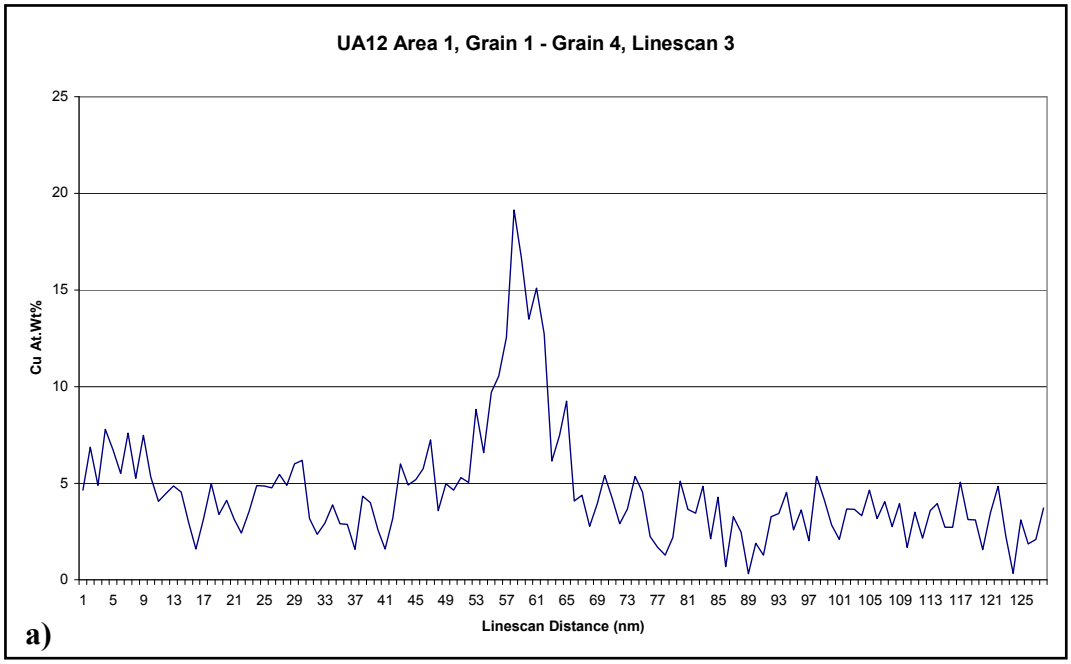

Figure 4.45. TEM Study: AA2096 UA12 Temper. EDX Line scans across a very low-angle grain boundary (0.85º).

Energy dispersive X-ray (EDX) line scan analysis across the boundary between grain 1 and grain 4: Line scan 2. Refer to Figure 4.43.

5. Discussion

Previous studies [19, 20, 55] have indicated that two distinct windows of SCC susceptibility exist for Al-Li-Cu-Ag alloy AA2096 as a function of isothermal aging time at 160ºC. The severely under-aged and over-aged tempers exhibit high susceptibility to IGC/SCC (refer to Figure 1.3). This current study has investigated possible microstructural/electrochemical culprits primarily in the severely under-aged temper (UA4).

It has been discussed in Chapter 1 that for IGC/SCC to occur an electrochemically active path must exist leading to preferential dissolution at or near to grain boundaries. The most popular models for the formation of this electrochemically active path are a solute-depleted zone neighbouring the grain boundary and/or the presence of continuous electrochemically active precipitates on the grain boundary. Whether the dominating factor is an actively corroding precipitate, a solute-depleted zone or a combination of the two remains unresolved.

From Connolly's previous work [20] orientation imaging microscopy (OIM) was used to investigate the occurrence of SCC in the UA4 temper of AA2096 in a alternate immersion (AI) 0.6 M NaCl environment as a function of grain misorientation. It is clear from the study that the occurrence of intergranular stress corrosion cracking is affected by the grain misorientation angle. Cracking was observed predominately on low-angle grain boundaries (3 – 9º).

The precipitate phase of most interest in this study is the copper-rich T_1 phase. The precipitation of the T_1 phase draws copper from the surrounding area leading to a solute-depleted zone neighbouring the particle. Depending on the nature and distribution of the T_1 phase an electrochemical framework for the preferential dissolution in the vicinity of grain boundaries can be established. Two distinctly different forms of T_1 precipitation has been observed as a function of grain misorientation. On high angle boundaries ($\geq 9^{o}$), in the UA4 temper, large isolated T_1 particles were observed while on the low angle ($3 - 9^{o}$) boundaries a near continuous decoration of fine T_1 precipitates was observed. It stands to reason that two different precipitate nucleation mechanisms exist for grain boundaries of different misorientations. The fine precipitation along low-angle grain boundaries would suggest a volume (Zener) diffusion growth mechanism. At high angles of misorientation, the large isolated T_1 particles observed would suggest a collector plate growth mechanism as grain boundary transport of copper becomes a dominating factor. Conventional metallurgical thinking would suggest that SCC susceptibility would vary according to the nature of the grain misorientation and the form of resultant grain boundary precipitation.

There are two possible mechanisms for preferential anodic dissolution along a grain boundary: 1) dissolution of a near continuous path of anodic precipitates and 2) dissolution of an anodically active solute-depleted zone due to precipitation. On low angle grain boundaries in the UA4 temper the fine, near continuous precipitation of the copper-rich T_1 phase can lead to depletion of copper from the adjacent area and results in the formation of a path for preferential anodic dissolution at the grain

boundary-matrix interface. Referring to Figure 1.4 it can be seen that in Al-Cu binary alloys the corrosion/pit repassivation potential decreases as the copper content is decreased from the solid solution. This difference in electrochemical potential provides the electrochemical mechanism for an active path adjacent to the grain boundaries in the UA4 temper leaving the copper depletion mechanism as a viable culprit for the high SCC susceptibility observed on low-angle grain boundaries of the UA4 temper. The EDX study of low-angle grain boundaries in this temper certainly corroborates the hypothesis. Copper depletion was observed on all of the investigated low-angle grain boundaries of the UA4 temper with a corresponding T_1 PFZ of a similar width. The question now must be addressed as to the viability of the mechanism where the electrochemically active path along a grain boundary is provided by a near-continuous precipitation of an anodically-active phase. From this work it is has been shown (see Figures 4.29 and 4.43 for UA4 and UA12, respectively) that for both the SCC susceptible UA4 temper and the non-SCC susceptible UA12 temper a near continuous decoration of T_1 particles is observed on low angle boundaries. It is therefore reasonable to conclude that T_1 dissolution is not the controlling feature for preferential anodic dissolution and resultant SCC susceptibility; the increased aging treatment from 4 to 12 hours at 160ºC is unlikely to result in dramatic differences in T_1 chemistry and resultant electrochemical character. Though it has been shown (Figure 1.5) that there appears to be a electrochemical framework where T_1 is more active than the 2096 matrix (i.e., T_1 has lower pitting potentials compared to the 2096 matrix) the evidence in these former studies may be questioned as the electrochemistry was performed on synthesised bulk T_1 and may not be representative of the anodic activity of actual precipitates.

For high angle boundaries in the UA4 temper (≥ 9º), one or two large T_1 phase precipitates can often be observed growing along the grain boundary. Figures 4.15 – 4.18 show the results of an EDX study to compare the variation in copper solute depletion as a function of distance from a large T_1 type precipitate on a high-angle boundary. Solute transport along the grain boundary (collector plate mechanism) will play a major role in the growth of a precipitate of this size and nature. It is interesting to note from the results that a distinct difference in copper depletion existed in the EDX measurements taken away from the large precipitate and the measurements taken close to or directly across the precipitate. Copper depletion was observed in the area adjacent to the large precipitate while no depletion was observed in measurements taken away from the precipitate. Although there is evidence of copper depletion adjacent to the large T_1 type precipitates on the high angle grain boundaries of the UA4 temper, the particles are few and far between, meaning that there is a large amount of bulk material between the zones susceptible to preferential dissolution. On the low-angle grain boundaries, the copper-depleted zone runs the whole length of the boundary due to the near continuous decoration of T_1 precipitates. In this case the whole of the adjacent area is more susceptible to preferential dissolution due to solute depletion. It is reasonable to suggest that this variation in preferential dissolution susceptibility as a function of grain misorientation affects the likelihood of intergranular cracking in the UA4 temper. This variation must be considered as a factor when referring to the previous OIM results [20].

The window of SCC susceptibility in the under-aged tempers ranges from the UA4 temper to the UA8 temper (see Figure 1.3). For the UA10 temper through to the

peak-aged (30 hours at 160ºC) temper no SCC susceptibility was observed. Connolly's work [20] employed several techniques to investigate the variation in SCC susceptibility as a function of isothermal aging time at 160ºC (discussed in section 1.2.3.). The results of electrochemical, XRD and electrical conductivity tests [20] correlated well with the window of SCC recorded for the under-aged tempers of AA2096. A levelling of the interplanar spacing and the electrical conductivity were observed at approximately 6 – 10 hours of isothermal aging at 160ºC. This is the same time frame over which the extremely SCC susceptible under-aged tempers cease to exhibit IGSCC. The study suggests that as further precipitation of copper-rich phases occurs within the matrix upon further aging a draining/levelling of the solid solution copper from the matrix eliminates the path for preferential dissolution. The elimination of a preferential path could be a driving mechanism to explain the resistive nature of the intermediate to peak-aged tempers to SCC.

The brief work carried out with the UA12 temper of AA2096 in the current study shows some signs to support the levelling of copper in the grain matrix. Figure 4.40. shows a dark field image of a grain group in the UA12 temper. Two low-angle grain boundaries (grains 3 and 6) show no sign of a T_1 PFZ. The low-angle grain boundaries of the UA4 temper exhibited distinct T_1 PFZs that correlated with the measured copper depleted zones. In addition a much higher volume fraction of T_1 precipitates can be observed within the grain matrix when compared to the UA4 temper. The matrix T_1 precipitates are also much larger than the T_1 precipitates in the UA4 temper. It is reasonable to suggest that the lack of a T_1 PFZ combined with a higher density of large T_1 matrix precipitates in the UA12 temper would indicate a

levelling of the available solid solution copper at the grain boundary-matrix interface. Therefore a reduction/elimination of the copper-depleted zone adjacent to the grain boundary would be expected.

6. Conclusions

1.) T_1 precipitation exists on both low-angle (3 – 9º) and high-angle (≥ 9º) grain boundaries in the UA4 temper of AA2096.

2.) Low-angle grain boundaries of the UA4 temper exhibit a dense, near continuous decoration of T_1 precipitates suggesting a Zener bulk diffusion growth mechanism. High-angle boundaries of the UA4 temper exhibit one or two large T_1 type precipitates that grow along the grain boundary, suggesting a collector plate growth mechanism.

3.) A T_1 PFZ can be observed on low-angle grain boundaries of the UA4 temper. No such T_1 PFZ exists on high-angle grain boundaries.

4.) EDX line scans show distinct bands of copper-depletion adjacent to low-angle grain boundaries of the UA4 temper. The measured copper-depleted bands correlate well with the width of the T_1 PFZ.

5.) EDX line scans across high-angle grain boundaries of the UA4 temper show no copper depleted zone adjacent to the boundary when measured away from any large T_1 type precipitates. However a small amount of copper-depletion was observed when an EDX line scan was taken directly across a large T_1 type precipitate on a high-angle grain boundary.

6.) The EDX results of this study corroborate the suggestion of Connolly's work [19, 20, 55] that the copper-depletion mechanism is a controlling feature for the preferential anodic dissolution along grain boundaries of the UA4 temper of AA2096.

7.) No T_1 PFZ was observed along low-angle grain boundaries of the UA12 temper. This factor combined with a higher volume fraction of large T_1 matrix precipitates than that observed in the UA4 temper would suggest a levelling of the available solid solution copper in the matrix thereby reducing/eliminating copper depletion at the grain boundary-matrix interface.

7. Future Work

It was originally intended to carry out a full microstructural TEM and EDX investigation into the UA4 and UA12 tempers of AA2096. The SCC susceptibility window observed in Connolly's work [19, 20, 55] suggested a significant change in the electrochemical behaviour of AA2096 from the severely under-aged tempers to the near peak-aged tempers. There is strong evidence to suggest that the observed copper depleted zones in the UA4 temper are reduced/eliminated with further isothermal aging. To confirm this, a thorough analysis of a near peak-age temper (i.e., UA12) is required. Unfortunately, due to equipment failure during the later stages of this project, further analysis of the UA12 temper was prevented.

To complete this study, further grain boundaries of the UA12 temper should be analysed. In particular EDX line scan analysis of grain boundaries in the range of 3 – 12º misorientation should be carried out to investigate the possibility of copper depletion. The results of such a study would help to explain the change in electrochemical behaviour observed between the under-aged and near peak-aged tempers of AA2096.

8. References

[1] **Porter, D.A.E., KE.**, *Phase Transformations in Metals and Alloys*. 2nd ed. 1992: London : Chapman & Hall. .

[2] **Starke, E.A., Jr., Sanders, T.H., Jr., and Palmer, I.G.**, *New Approaches to Alloy Development in the Al-Li System.* Journal of Metals, 1981. **33**(8): p. 24-32.

[3] **Vasudevan, A.K., Ziman, P.R., Jha, S.C., and Sanders, T.H., Jr.** *Stress Corrosion Resistance of Al-Cu-Li-Zr Alloys*. 1986. Oxford, England: Inst of Metals, London, England.

[4] **Quist, W.E., Narayanan, G.H., and Wingert, A.L.** *Aluminum-Lithium Alloys for Aircraft Structure - an Overview*. 1984. Monterey, CA, USA: Metallurgical Soc of AIME, Warrendale, PA, USA.

[5] **Silcock, J.M.**, *Structural Ageing Characteristics of Aluminium-Copper-Lithium Alloys.* Institute of Metals -- Journal, 1960. **88**(Part 8): p. 357-364.

[6] **Nock, J.J.A., Holt, M., Sprowls, D.O., Collins, F.R., Nelson, F.G., and Robinson, I.B.**, *New High-Strength Aluminum Alloy.* Metal Progress, 1961. **80**(3, 5).

[7] **Spuhler, E.H., Knoll, A.H., and Kaufman, J.G.**, *Lithium in Aluminum -- X2020.* Metal Progress, 1960. **77**(6): p. 80-82.

[8] **Sankaran, K.K. and Grant, N.J.**, *The Structure and Properties of Splat-Quenched Aluminium Alloy 2024 Containing Lithium Additions.* Material Science and Engineering, 1980. **44**(2): p. 213-27.

[9] LeBaron, I. 1945.

[10] **Hardy, H.K. and Silcock, J.M.**, *Phase Sections at 500 and 350 C of Aluminium-Rich Aluminium-Copper-Lithium Alloys.* Institute of Metals Journal, 1956. **84**(Part 2): p. 423-428.

[11] **Hardy, H.K.**, *Trace-Element Effects in Some Precipitation-Hardening Aluminium Alloys.* Institute of Metals -- Journal, 1956. **84**(Part 2): p. 429-439.

[12] **Balmuth, E.S. and Schmidt, R.**, *Perspective on the Development of Aluminum-Lithium Alloys.* Bulletin de l'Association Technique Maritime et Aeronautique, 1981: p. 69-88.

[13] **Huang, J.C. and Ardell, A.J.**, *Strengthening Mechanisms Associated with T_1 Particles in 2 Al-Li-Cu Alloys.* Journal De Physique, 1987. **48**(C-3): p. 373-383.

[14] **Wang, S.C. and Starink, M.J.**, *Precipitates and Intermetallic Phases in Precipitation Hardening Al-Cu-Mg-(Li) Based Alloys.* International Materials Reviews, 2005. **50**(4): p. 193-215.

[15] **Suresh, S., Vasudevan, A.K., Tosten, M., and Howell, P.R.**, *Microscopic and Macroscopic Aspects of Fracture in Lithium-Containing Aluminum Alloys.* Acta Metallurgica, 1987. **35**(1): p. 25-46.

[16] **Gao, N., Starink, M.J., Davin, L., Cerezo, A., Wang, S.C., and Gregson, P.J.**, *Microstructure and Precipitation in Al-Li-Cu-Mg-(Mn,Zr) Alloys.* Materials Science and Technology, 2005. **21**(9): p. 1010-18.

[17] **Wang, S.C. and Starink, M.J.**, *Two Types of S Phase Precipitates in Al-Cu-Mg Alloys.* Acta Materialia, 2007. **55**(3): p. 933-941.

[18] **Huang, J.C. and Ardell, A.J.** *Microstructural Evolution in Two Al-Li-Cu Alloys*. 1986. Oxford, England: Inst of Metals, London, England.

[19] **Connolly, B.J. and Scully, J.R.**, *Corrosion Cracking Susceptibility in Al-Li-Cu Alloys 2090 and 2096 as a Function of Isothermal Aging Time.* Scripta Materialia, 2000. **42**(11): p. 1039-45.

[20] Connolly, B.J., *The Transition from Localised Corrosion to Scc of Al-Li-Cu Alloy Aa2096 as a Function of Isothermal Aging Treatment at 160ºC. Ph.D. Dissertation*, The University of Virginia. 2002.

[21] **Williams, D.B. and Edington, J.W.**, *The Discontinuous Precipitation Reaction in Dilute Al-Li Alloys.* Acta Metallurgica, 1976. **24**(4): p. 323-32.

[22] **Muddle, B.C. and Polmear, I.J.**, *The Precipitate Ω Phase in Al-Cu-Mg-Ag Alloys.* Acta Metallurgica, 1989. **37**(3): p. 777-89.

[23] **Wilson, R.N. and Partridge, P.G.**, *The Nucleation and Growth of S' Precipitates in an Aluminium-2.5% Copper-1.2% Magnesium Alloy.* Acta Metallurgica, 1965. **13**(12): p. 1321-1328.

[24] **Noble, B. and Thompson, G.E.**, *Precipitation Characteristics of Aluminium-Lithium Alloys.* Metal Science Journal, 1971. **5**: p. 114-20.

[25] **Williams, D.B. and Edington, J.W.**, *The Precipitation of δ'(Al3Li) in Dilute Aluminium-Lithium Alloys.* Metal Science, 1975. **9**(12): p. 529-32.

[26] **Edgar, A., Starke, Jr.**, *The Causes and Effects of 'Denuded' or Precipitate Free Zones at Grain Boundaries in Aluminium Base-Alloys.* Journal of Metals, 1970. **22**: p. 64-64.

[27] **Noble, B. and Trowsdale, A.J.**, *Evidence for Pre δ' Precipitation Events in an Al-Li Alloy.* Scripta Metallurgica et Materialia, 1995. **33**(1): p. 33-8.

[28] **Ohmori, Y., Ito, S., and Nakai, K.**, *Aging Behavior of an Al-Li-Cu-Mg-Zr Alloy.* Metallurgical and Materials Transactions A: Physical Metallurgy and Materials Science, 1999. **30A**(3): p. 741-749.

[29] **Gu, B.P., Liedl, G.L., Kulwicki, J.H., and Sanders, T.H., Jr.**, *Coarsening of δ' (Al3Li) Precipitates in an Al-2.8Li-0.3mn Alloy.* Material Science and Engineering, 1985. **70**: p. 217-28.

[30] **Sanders, T.H., Jr. and Starke, E.A., Jr.** *Overview of the Physical Metallurgy in the Al-Li-X Systems*. 1984. Monterey, CA, USA: Metallurgical Soc of AIME, Warrendale, PA, USA.

[31] **Baumann, S.F. and Williams, D.B.**, *Experimental Observations on the Nucleation of Growth of δ' (Al3Li) in Dilute Al-Li Alloys.* Metallurgical Transactions A (Physical Metallurgy and Materials Science), 1985. **16A**(7): p. 1203-11.

[32] **Starink, M.J. and Gregson, P.J.**, *Thermodynamics and Precipitation in 8090 (Al-Li-Cu-Mg-Zr) Alloys Studied by DSC and TEM.* Materials Science Forum, 1996. **217-222**(pt 2): p. 673-678.

[33] **Noble, B., Harris, S.J., and Dinsdale, K.**, *Yield Characteristics of Aluminium-Lithium Alloys.* Metal Science, 1982. **16**(9): p. 425-30.

[34] **Sanders, T.H., Jr. and Starke, E.A., Jr.**, *Effect of Slip Distribution on the Monotonic and Cyclic Ductility of Al-Li Binary Alloys.* Acta Metallurgica, 1982. **30**(5): p. 927-939.

[35] **Tosten, M.H., Vasudevan, A.K., and Howell, P.R.** *Grain Boundary Precipitation in Al-Li-Cu Alloys*. 1986. Oxford, England: Inst of Metals, London, England.

[36] **Tosten, M.H., Vasudevan, A.K., and Howell, P.R.** *Microstructural Development in Al-2%Li-3%Cu Alloy*. 1986. Oxford, England: Inst of Metals, London, England.

[37] **Ahmad, M.**, *Effects of Environment and Microstructure on Stress Corrosion Crack Propagation in an Al-Li-Cu-Mg Alloy.* Materials Science & Engineering A (Structural Materials: Properties, Microstructure and Processing), 1990. **A125**(1): p. 1-14.

[38] **Vasudevan, A.K., Ludwiczak, E.A., Baumann, S.F., Doherty, R.D., and Kersker, M.M.**, *Fracture Behaviour in Al-Li Alloys: Role of Grain Boundary δ.* Material Science and Engineering, 1985. **72**(2): p. 25-30.

[39] **Baur, R. and Gerold, V.**, *Clustering in Aluminium-Copper Alloys. I. Quantitative X-Ray Determination of the Sizes and Amount of Guinier-Preston-Zones. I.* Zeitschrift fur Metallkunde, 1966. **57**(3): p. 181-186.

[40] **Grant, N.J., Kang, S., and Wang, W.**, *Structure and Properties of Rapidly Solidified 2000 Series Al-Li Alloys.* Bulletin de l'Association Technique Maritime et Aeronautique, 1981: p. 171-188.

[41] **Rinker, J.G., Marek, M., and Sanders, T.H., Jr.**, *Microstructure, Toughness and Stress Corrosion Cracking Behavior of Aluminum Alloy 2020.* Materials Science and Engineering, 1984. **64**(2): p. 203-221.

[42] **Starke, E.A., Jr. and Lin, F.S.**, *Influence of Grain Structure on the Ductility of the Al-Cu-Li-Mn-Cd Alloy 2020.* Metallurgical Transactions A (Physical Metallurgy and Materials Science), 1982. **13A**(12): p. 2259-2269.

[43] **Kang, S. and Grant, N.J.**, *Rapidly Solidifying P/M X2020 Aluminum Alloys.* Metallurgical Transactions A (Physical Metallurgy and Materials Science), 1987. **18A**(12): p. 2037-46.

[44] **Noble, B. and Thompson, G.E.**, *T_1 (Al2CuLi) Precipitation in Aluminium-Copper-Lithium Alloys [Electron Microscope Examination of Microstructure]*. Metal Science Journal, 1972. **6**: p. 167-74.

[45] **Flower, H.M. and Gregson, P.J.**, *Solid State Phase Transformations in Aluminium Alloys Containing Lithium.* Materials Science and Technology, 1987. **3**(2): p. 81-90.

[46] **Gregson, P.J. and Flower, H.M.**, *Microstructural Control of Toughness in Aluminium-Lithium Alloys.* Acta Metallurgica, 1985. **33**(3): p. 527-37.

[47] **Sainfort, P. and Guyot, P.** *Fundamental Aspects of Hardening in Al-Li and Al-Li-Cu Alloys*. 1986. Oxford, England: Inst of Metals, London, England.

[48] **Huang, J.C. and Ardell, A.J.**, *Crystal Structure and Stability of T_1 Precipitates in Aged Al-Li-Cu Alloys.* Materials Science and Technology, 1987. **3**(3): p. 176-188.

[49] **Howe, J.M., Lee, J., and Vasudevan, A.K.**, *Structure and Deformation Behavior of T_1 Precipitate Plates in an Al-2Li-Cu Alloy.* Metallurgical Transactions A (Physical Metallurgy and Materials Science), 1988. **19A**(12): p. 2911-2920.

[50] **Zhao, Z., Liu, L., and Chen, Z.**, *Co-Strengthening Contribution of δ' and T_1 Precipitates in Al-Li Alloys 2090 and 2090 + Ce.* Rare Metals, 2006. **25**(3): p. 197-201.

[51] **Gregson P. J., C.S.A.**, *Grain Boundary Precipitation of I-Phase in 8090 Alloy Sheet.* Scripta metallurgica et materialia, 1994. **30**(10): p. 1359-1363.

[52] **Liu, Y.Z., Y; HU, ZQ; SHI, CX**. *The Influence of Mg and Zr on T_2 Phase and Precipitation Free Zone of Al-Li Alloy*. in *6th International Aluminium Conference*. 1991 Garmisch Partenkirchen Germany: DGM Metallurgy Information, New York.

[53] **Rioja, R.J. and Ludwiczak, E.A.** *Identification of Metastable Phases in Al-Cu-Li Alloy (2090)*. 1986. Oxford, England: Inst of Metals, London, England.

[54] **White, J., Miller, W.S., Palmer, I.G., Davis, R., and Saini, T.S.** *Effect of Precipitation on Mechanical Properties of Al-Li-Cu-Mg-Zr Alloy*. 1986. Oxford, Engl: Inst of Metals, London, Engl.

[55] **Connolly, B.J. and Scully, J.R.**, *Transition from Localized Corrosion to Stress Corrosion Cracking in an Al-Li-Cu-Ag Alloy.* Corrosion, 2005. **61**(12): p. 1145-1166.

[56] **Crooks, R.E. and Starke, E.A., Jr.**, *Microstructure and Tensile Properties of a Splat-Quenched Al-Cu-Li-Mg-Zr Alloy.* Metallurgical Transactions A (Physical Metallurgy and Materials Science), 1984. **15A**(7): p. 1367-1377.

[57] **Ludwiczak, E.A. and Rioja, R.J.**, *Tb Precipitates in an Al-Cu-Li Alloy.* Scripta Metallurgica et Materialia, 1991. **25**(6): p. 1415-19.

[58] **Stimson, W., Tosten, M.H., Howell, P.R., and Williams, D.B.** *Precipitation and Lithium Segregation Studies in Al-2wt%Li-0. 1wt%Zr*. 1986. Oxford, England: Inst of Metals, London, England.

[59] **Makin, P.L. and Ralph, B.**, *On the Ageing of an Aluminium-Lithium-Zirconium Alloy.* Journal of Materials Science, 1984. **19**(12): p. 3835-43.

[60] **Galbraith, J.M., Tosten, M.H., and Howell, P.R.**, *On the Nucleation of Ω' and T_1 on Al3Zr Precipitates in Al-Li-Cu-Zr Alloys.* Journal of Materials Science, 1987. **22**(1): p. 27-36.

[61] **Niskanen, P., Sanders, T.H., Jr., Marek, M., and Rinker, J.G.**, *Influence of Microstructure on the Corrosion of Al-Li, Al-Li-Mn, Al-Li-Mg and Al-Li-Cu Alloys in 3.5% NaCl Solution.* Bulletin de l'Association Technique Maritime et Aeronautique, 1981: p. 347-376.

[62] **Rystad, S. and Ryum, N.**, *Metallographical Investigation of the Precipitation and Recrystallization Process in an Al-Zr-Alloy.* Aluminium, 1977. **53**: p. 193-195.

[63] **Perlitz, H. and Westgren, A.**, *The Crystal Structure of Al2cumg.* Arkiv for Kemi, Mineralogi och Geologi, 1943. **16**(5): p. 5.

[64] **Reich, L., Ringer, S.P., and Hono, K.**, *Origin of the Initial Rapid Age Hardening in an Al-1.7 At.% Mg-1.1 At.% Cu Alloy.* Philosophical Magazine Letters, 1999. **79**(9): p. 639-648.

[65] **Wang, S.C. and Starink, M.J.**, *The Assessment of GPB2/S" Structures in Al-Cu-Mg Alloys.* Materials Science & Engineering A (Structural Materials: Properties, Microstructure and Processing), 2004. **A386**(1-2): p. 156-63.

[66] **Weatherly, G.C. and Nicholson, R.B.**, *An Electron Microscope Investigation of the Interfacial Structure of Semi-Coherent Precipitates.* Philosophical Magazine, 1968. **17**: p. 801-831.

[67] **Gregson, P.J., Dinsdale, K., Harris, S.J., and Noble, B.**, *Evolution of Microstructure in Al-Li-Zn-Mg-Cu Alloys.* Materials Science and Technology, 1987. **3**(1): p. 7-13.

[68] **Starink, M.J., Wang, P., Sinclair, I., and Gregson, P.J.**, *Microstructure and Strengthening of Al-Li-Cu-Mg Alloys and MMCS. Ii. Modelling of Yield Strength.* Acta Materialia, 1999. **47**(14): p. 3855-68.

[69] **Kerry, S. and Scott, V.D.**, *Structure and Orientation Relationship of Precipitates Formed in Al-Cu-Mg-Ag Alloys.* Metal Science, 1984. **18**(6): p. 289-94.

[70] **Knowles, K.M. and Stobbs, W.M.**, *The Structure of {111} Age-Hardening Precipitates in Al-Cu-Mg-Ag Alloys.* Acta Crystallographica, Section B (Structural Science), 1988. **B44**: p. 207-27.

[71] **Auld, J.H.** *Structure of a Metastable Precipitate in an Al-Cu-Mg-Ag Alloy*. 1972. Kyoto, Japan.

[72] **Garg, A., Chang, Y.C., and Howe, J.M.**, *Precipitation of the Ω Phase in an Al-4.0cu-0.5mg Alloy.* Scripta Metallurgica et Materialia, 1990. **24**(4): p. 677-680.

[73] **Garg, A. and Howe, J.M.**, *Nucleation and Growth of Ω Phase in Al-4.0 Cu-0.5 Mg-0.5 Ag Alloy. An in Situ Hot-Stage TEM Study.* Acta Metallurgica et Materialia, 1991. **39**(8): p. 1925-37.

[74] **Wang, S.C., Starink, M.J., and Gao, N.**, *Precipitation Hardening in Al-Cu-Mg Alloys Revisited.* Scripta Materialia, 2006. **54**(2): p. 287-291.

[75] **Polmear, I.J. and Couper, M.J.**, *Design and Development of an Experimental Wrought Aluminum Alloy for Use at Elevated Temperatures.* Metallurgical Transactions A (Physical Metallurgy and Materials Science), 1988. **19A**(4): p. 1027-35.

[76] **Lee, S.-M., Pyun, S.-I., and Chun, Y.-G.**, *Critical Evaluation of the Stress-Corrosion Cracking Mechanism in High-Strength Aluminum Alloys.* Metallurgical Transactions A (Physical Metallurgy and Materials Science), 1991. **22A**(10): p. 2407-2414.

[77] **Zohdi, T.I. and Meletis, E.I.**, *On the Intergranular Hydrogen Embrittlement Mechanism of Al-Li Alloys.* Scripta Metallurgica et Materialia, 1992. **26**(10): p. 1615-20.

[78] **Craig, J.G., Newman, R.C., Jarrett, M.R., and Holroyd, N.J.H.** *Local Chemistry of Stress-Corrosion Cracking in Al-Li-Cu-Mg Alloys*. 1987. France.

[79] **Kumai, C., Kusinski, J., Thomas, G., and Devine, T.M.**, *Influence of Aging at 200 C on the Corrosion Resistance of Al-Li and Al-Li-Cu Alloys.* Corrosion (Houston), 1989. **45**(4): p. 294-302.

[80] **Wall, F.D. and Stoner, G.E.**, *The Evaluation of the Critical Electrochemical Potentials Influencing Environmentally Assisted Cracking of Al-Li-Cu Alloys in Selected Environments.* Corrosion Science, 1997. **39**(5): p. 835-53.

[81] **Lynch, S.P., Wilson, A.R., and Byrnes, R.T.**, *Effects of Ageing Treatments on Resistance to Intergranular Fracture of 8090 Al-Li Alloy Plate.* Materials Science & Engineering A (Structural Materials: Properties, Microstructure and Processing), 1993. **A172**(1-2): p. 79-93.

[82] **Vasudevan, A.K., Miller, A.C., and Kersker, M.M.** *Contribution of Na-Segregation to Fracture Behavior of Al-11.4 At.% Li Alloys*. 1984. Warrendale, PA, USA: Metallurgical Soc of AIME.

[83] **Smith, S.W. and Scully, J.R.** *Hydrogen Trapping and Its Correlation to the Hydrogen Embrittlement Susceptibility of Al-Li-Cu-Zr Alloys*. 1996: Minerals, Metals & Materials Soc (TMS).

[84] **Narayanaswamy, K. and Balasubramaniam, R.**, *Theoretical Analysis of Stress Corrosion Cracking in Al-Li Alloys.* Transactions of the Indian Institute of Metals, 1992. **45**(4): p. 253-5.
[85] **Cherepanov, G.**, *Comprehensive Treatise of Electrochemistry, Ch. 7: Stress Corrosion Cracking*. Vol. 4. 1981: Plenum Press, New York.
[86] **Holroyd, N.J.H.V., A.K. and Christodoulou**, *Treatise on Materials Science and Technology, Ch 16: Stress Corrosion of High-Strength Aluminium Alloys*. Vol. 31. 1989: CA: Academic Press, San Diego.
[87] **Galvele, J.R. and Demichel.Sm**, *Mechanism of Intergranular Corrosion of Al-Cu Alloys.* Corrosion Science, 1970. **10**(11): p. 795-807.
[88] **Sugimoto, K., Hoshino, K., Kageyama, M., Kageyama, S., and Sawada, Y.**, *Stress Corrosion Cracking of Aged Al-4% Cu Alloy in NaCl Solution.* Corrosion Science, 1975. **15**(11-12): p. 709-20.
[89] **Muller, I.L. and Galvele, J.R.**, *Pitting Potential of High Purity Binary Aluminium Alloys. Al-Cu Alloys. Pitting and Intergranular Corrosion.* Corrosion Science, 1977. **17**(3): p. 179-193.
[90] **Urushino, K. and Sugimoto, K.**, *Stress-Corrosion Cracking of Aged Al-Cu-Mg Alloys in NaCl Solution.* Corrosion Science, 1979. **19**(4): p. 225-36.
[91] **Maitra, S. and English, G.C.**, *Mechanism of Localized Corrosion of 7075 Alloy Plate.* Metallurgical Transactions A (Physical Metallurgy and Materials Science), 1981. **12A**(3): p. 535-41.
[92] **Dorward, R.C. and Hasse, K.R.**, *Stress Corrosion Cracking Behavior of an Allicumg Alloy.* Corrosion, 1987. **43**(7): p. 408-13.
[93] **Dorward, R.C.**, *Influence of Grain Structure on Stress Corrosion Resistance and Tensile Properties of Al-2Li-2Cu-1.5Mg Alloy Sheet.* Corrosion (Houston), 1990. **46**(4): p. 348-352.
[94] **Marsac, S., Mankowski, G., and Dabosi, F.**, *Stress Corrosion Cracking Behaviour of 2091 Al-Li Alloy in Sulphate and Chloride Containing Solutions.* British Corrosion Journal, 1992. **27**(1): p. 50-8.
[95] **Komisarov, V., Talianker, M., and Cina, B.**, *The Effect of Retrogression and Reaging on the Resistance to Stress Corrosion of an 8090 Type Aluminium Alloy.* Materials Science & Engineering A (Structural Materials: Properties, Microstructure and Processing), 1996. **A221**(1-2): p. 113-21.
[96] **Meletis, E.I.**, *Microstructure and Stress-Corrosion Cracking Relationship in an Al-Li-Cu-Zr Alloy.* Material Science and Engineering, 1987. **93**: p. 235-45.
[97] **Lumsden, J.B. and Allen, A.T.**, *The Stress Corrosion Cracking Behavior of AlLi Alloy 8090.* Corrosion, 1988. **44**(8): p. 527-32.
[98] **Belk, J.**, *Electron Microscopy and Microanalysis of Crystalline Materials*. 1979: Applied Science Publishers, London. .
[99] **Williams, D.C., CB.**, *Transmission Electron Microscopy: A Textbook for Materials Science*. 1996: Kluwer Academic.
[100] **Goodhew, P.H., FJ.**, *Electron Microscopy and Analysis*. 2nd. ed. 1988: Taylor & Francis, London, England.

9. Appendices

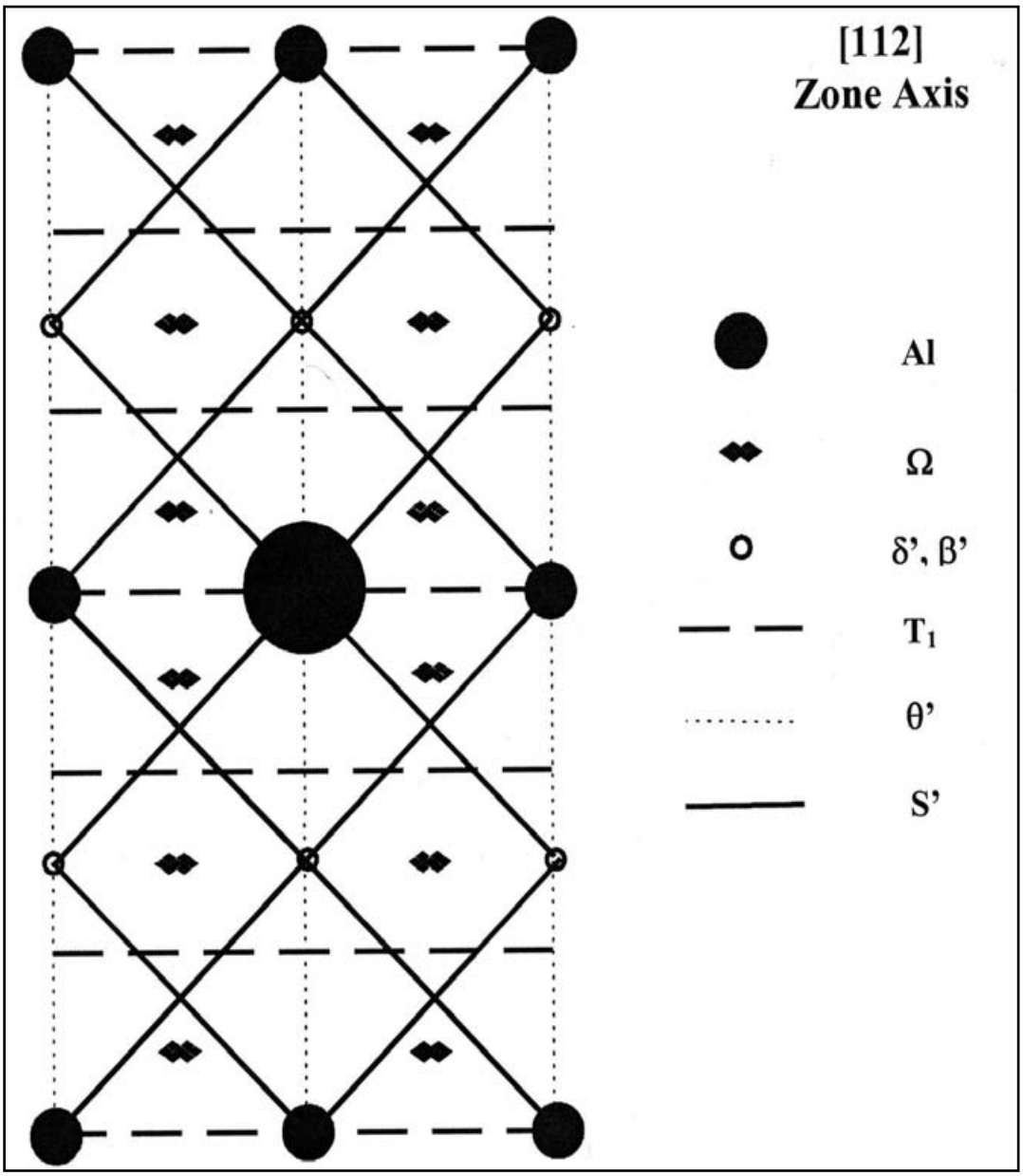

Figure A.1. Diagram of diffraction streaks and spots associated with a [112] zone axis used to identify possibly precipitate phases in AA2096 [20].